Università degli Studi di Torino

Scuola di Dottorato in

Scienze della Natura e Tecnologie Innovative

Dottorato in

Scienze Farmaceutiche e Biomolecolari

(XXXIII ciclo)

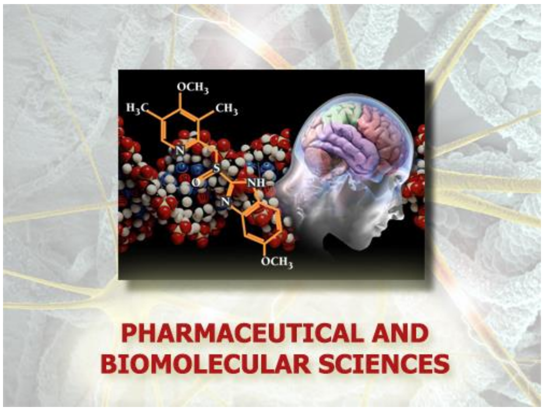

Surface Functionalization of Nanodiamonds for diagnostic applications

Candidato: Mirko Sacco

Tutor: Prof. Alessandro Barge

Università degli Studi di Torino

Dottorato in
Scienze Farmaceutiche e Biomolecolari

Tesi svolta presso il
Dipartimento di Scienza e Tecnologia del Farmaco

CICLO: XXXIII

TITOLO DELLA TESI: Surface functionalization of nanodiamonds for diagnostic applications

TESI PRESENTATA DA: Mirko Sacco

TUTOR: Prof. Alessandro Barge

COORDINATORE DEL DOTTORATO: Prof.ssa Roberta Cavalli

ANNI ACCADEMICI: 2018-2020

SETTORE SCIENTIFICO-DISCIPLINARE DI AFFERENZA: CHIM06

Summary

CARBOXYLIC SURFACE FUNCTIONALIZATION: NDs AS FLUORESCENT TARGETED NANOSYSTEMS 82

ABSTRACT

Currently, a strong interest has been focused on the employment of carbon nanoparticles as promising tools in biomedical research, diagnostics and therapy[1]. Size, biocompatibility, cost-effectiveness, detectability, modifications and targetability are fundamental characteristics for a nanomaterial for applications in the therapeutic field. On the other hand, a nanomaterial that can act as a sensor would be an excellent tool for diagnostics.

Due to their structure, nanodiamonds (NDs) possess all these features, making them exploitable both in therapy and in diagnostics, therefore in the so-called theranostics.

NDs are naturally fluorescent core-shell nanoparticles, made of a inner diamond-like core and a surface, partially graphitic and oxidized, mainly with carboxylic groups[2]. The core may contain some lattice defects, the more interesting among them is the nitrogen-vacancy (NV) center, responsible of NDs stable and intense fluorescence[3]. Despite the inertness of the core, NDs surface can react, making NDs suitable for many applications.

Synthesis and post-synthesis treatments of NDs can alter the characteristics of both the inner core, therefore the fluorescence[4], and of the surface[5], making this nanomaterial very versatile.

NDs fluorescence make them suitable for applications in sensoristic field, because their emission characteristics are deeply influenced by environmental factors, such as magnetic noise and surface charges[6]. In biomedicine NDs can be exploited as nanometric scale sensors for all those parameters that are altered in pathological conditions, such as pH and redox potential[7]. However, in order to make them even more exploitable for applications, NDs surface decoration with active molecules should be adequate and predictable.

The introduction of heteroatoms on NDs, such as oxygen, sulphur, nitrogen, exploiting both graphitic and carboxylic surface groups (primary grafting), allows the nanomaterial conjugation with molecules of interest, such as contrast agents, drugs and antibodies (secondary grafting)[8]. Currently, the most common methods

involve the use of polymers, which have the disadvantage of changing the size of the nanodiamond and do not guarantee the modulation and predictability of both primary and secondary grafting[9].

In this research project we studied NDs surface chemical modifications in an efficient, predictable and tunable manner for diagnostic purposes, always looking at both surface features and internal fluorescence. More in detail, the Diels-Alder and 1,3-dipolar cycloaddition reactions via azomethine ylides generated by amino acids on the graphitic component and conjugation reactions on the carboxylic one were explored. Secondary grafting reactions of paramagnetic agents, porphyrins and antibodies were subsequently conducted, and nanomaterials were characterized. Since the natural fluorescence is a unique feature of these nanomaterials, part of this work is focused on increasing their fluorescence. We wondered whether and how surface modifications can alter the fluorescence emission characteristics. Furthermore, in order to obtain high-fluorescent NDs, we worked on post-synthesis modifications and we improved a strategy for producing NDs already intrinsically rich in NV centers, starting from modified graphite.

1. INTRODUCTION

Healthy conditions can be turned in to pathological ones by alterations of physiological mechanisms, as electric activity variations, metabolic alterations and protein transport impairments[7]. Variations in cellular environmental parameters, such as pH, oxygen concentration and metabolites redox state, are not only the cause of these pathologies, but they are often also the consequences[10]. The study and the high sensitivity detection of these alterations, in order to early diagnose the onset of many diseases and to intervene promptly, remain an interesting challenge.

Nanodiamonds represent a possible solution, because they can be used as sensors, exploiting their fluorescence, and as MRI tools, with the possibility to transfer magnetic polarization to metabolites. Nanodiamond particles, also called "ultra-dispersed diamonds", belong to the so-called third generation of carbon-based nanomaterials, divided into generations both from a chronological and applicability point of view (fullerenes and nanotubes belong to the first generation, graphene to the second)[11]. Nanodiamonds (NDs) are core-shell particles consisting of a diamond core of sp^3 hybridized carbon atoms and an outer surface, partly graphitic and partly oxidized[12] (Figure 1). The core may contain defects, in terms of impurities, atoms different from carbon and, in terms of defects, empty spaces within the diamond lattice. When these defects are sufficiently close together, they form the so-called atom-vacancy center; the most widely studied of which is the nitrogen-vacancy (NV) one, responsible for NDs fluorescence. The external surface consists partly of graphite layers, partly of amorphous carbon and partly of oxidized carbon, mainly in the form of carboxylic moieties. The NDs synthesis techniques and post-synthesis treatments can alter their surface characteristics. In particular, high-temperature annealing treatments in inert atmosphere lead to a general surface graphitization, while oxidizing etching leads to the extension of the oxidized component.

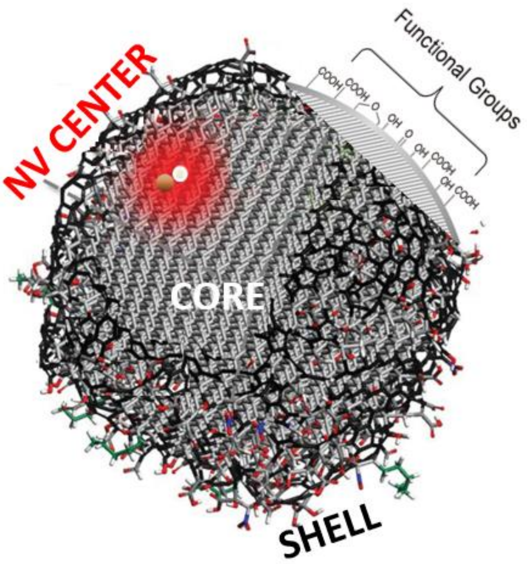

Figure 1. Nanodiamond general structure (adapted from ref.4).

1.1 Synthesis of nanodiamonds

The methodologies of nanodiamonds synthesis do not differ from those commonly used for the synthesis of carbon-based nanomaterials. However, given the profound structural and chemical-physical differences between nanodiamonds and fullerenes and nanotubes, it is necessary to significantly modify the conditions in which nanodiamonds are produced. Numerous methods of production have been performed until now, the most common of which are high-energy ball milling of diamond microcrystals grown at high static pressure high temperature (HPHT), the detonation technique and laser ablation (Figure 2). Size, surface features, morphology and aggregation tendency deeply depend on synthetic procedures. Major classes of commercial NDs are related to “static” or “dynamic” synthesis of diamond material. The former is obtained at high temperature under high static pressure maintained for minutes or hours and the latter involves a highly non-equilibrium process wherein the high temperature and high-pressure conditions exist within a fraction of microsecond.

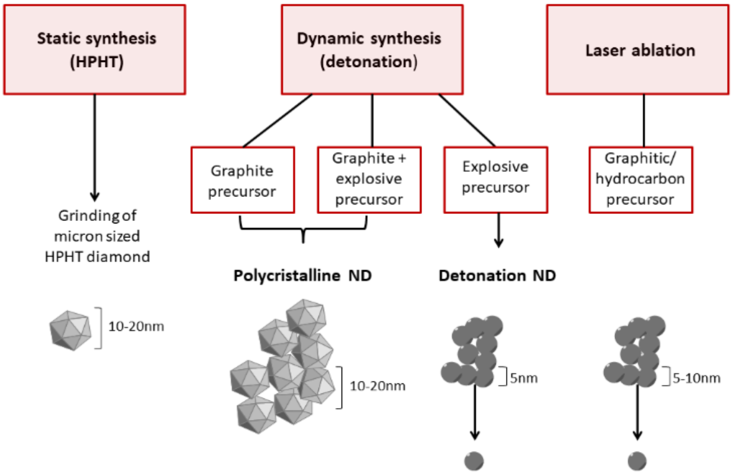

Figure 2. Most exploited nanodiamonds synthesis techniques.

1.1.1 Grinding of HPHT grown microcrystals

Nanodiamonds can be synthesized from grinding of diamond microcrystals obtained by HPHT synthesis[13].

With this method, carbon, for example in the form of graphite, is subjected to pressures and very high temperatures, respectively of 3.5 GPa and 3000K, for a few seconds. The carbon is placed in a chamber and a heated press compresses the material, which is fragmented into microparticles. As a function of the synthesis times and the quantity of material involved, particles can increase their size, making necessary a subsequent treatment by grinding, in order to obtain nanodiamonds. In fact, using prolonged times it is possible to increase the size of the microparticles produced, which can be subjected to further grinding to obtain the dimensions you want. Alternatively, the control of the size of the nanodiamonds, between 1 and 100 nm, can be exercised through the modulation of temperature and pressure reached in the synthesis chamber.

With this method it is possible to produce nanocrystals with low concentration of lattice defects.

1.1.2 Detonation

This technique involves the use of explosives detonated in a metal chamber in a oxygen-free atmosphere, oxygen-free carbon or graphite, in the presence of nitrogen, carbon dioxide and aqueous vapor[14].

The most used explosives are trinitrotoluene (TNT) and cyclonite (cyclotrimethylenetrinitramine), in a mixture of TNT and cyclonite 1:1 or 6:4. With the detonation, pressure and temperature inside the chamber instantly increase to about 27 GPa and 3500K, reaching the Jouget point. Jouget's point is a thermodynamic point, characterized by characteristic temperature and pressure, in which the gaseous products of the chemical reactions that took place in the area are formed. Considering the state diagram of the different phases in which the carbon exists (Figure 3A), the temperature and pressure achieved with detonation would not be sufficient to make the “raw” carbon liquid; however, in these conditions the carbon can exist in the liquid state if it occurs in the form of 1-2 nm nanodrops. As pressure and temperature decrease, these carbon nano-droplets coalesce into larger droplets, crystallize and agglomerate to form nanodiamonds, which increase their size.

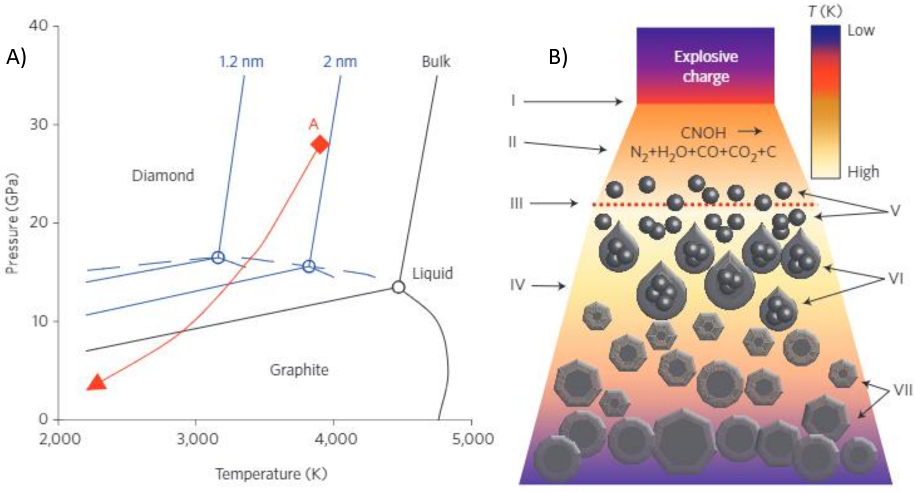

Figure 3. A) Carbon diagram phase in which Jouget Point (A) is shown. As the temperature and pressure decrease carbon atoms condense into nanoclusters (red line). B) Carbon nanodroplets creation and growth following detonation. (I) front of the shockwave; (II) zone of the chemical reactions; (III) Jouget point; (IV) expanding detonation products; (V) formation of nanoclusters; (VI) coagulation into nanodroplets; (VII) cristallization and agglomeration of nanodiamonds.

The moment the pressure drops below the diamond-graphite equilibrium line, the growth of the nanodiamond is replaced by the formation of a native graphite layer. Therefore, nanodiamonds form by homogeneous nucleation in the super-saturated vapor volume of carbon, for condensation and recrystallization of liquid carbon nanoparticles (Figure 3B).
With this technique 5-20 nm diamonds nanocrystals are obtained, wrapped and conglomerated in graphite shells[12].

1.1.3 Laser ablation

With this technique, a laser beam of high density is focused onto graphite, which is placed in water. The interaction of the laser beam and the target surface can result in vaporization of the target in the form of the so called ablation plume (Figure 4). Atoms of the target and liquid interact under high pressure and high temperature conditions induced by laser, allowing the formation of nanoparticles dispersed in suspension[15]. The synthesis of nanodiamonds by laser ablation is often performed in liquid medium, named also liquid phase pulse laser ablation (LP-PLA).

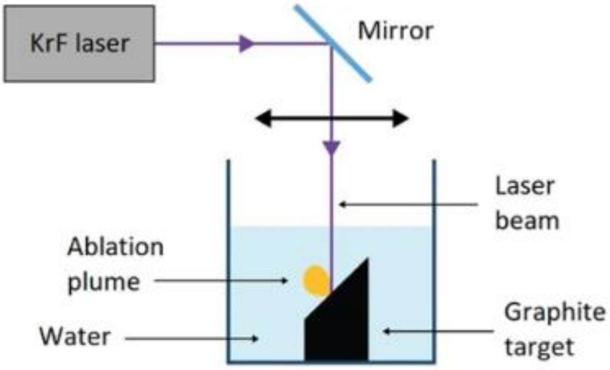

Figure 4. Pulsed laser ablation of graphite in liquid experimental setup.

More in detail, the graphite target is placed in a liquid media and a KrF laser beam of specific parameters is focused at the some predetermined distance from the target surface. The laser beam leads to the emergence of acoustic shock waves of high power that impact on the target surface and provide the required conditions of temperature and pressure, that are sufficient for the formation of the diamond cubic crystal structure of carbon[16]. Infact, as the duration of the laser pulses is rather short, the time derivatives of both the pressure (dP/dt) and the temperature (dT/dt) are extremely high and both P and T rise dramatically in certain micro-regions, reaching values in which the thermodynamically stable form of carbon is a diamond. Despite some mechanisms of nanodiamonds formation by laser ablation are elusive, a recent work[17] propose a thermodynamic model explaining the formation mechanism of NDs under the transient physical conditions in the ablation plume, followed by removal of graphitic byproducts.

The main advantage of this technique is that it enables the synthesis of NDs at room temperature and standard pressure conditions.

1.2 Post-synthesis treatments

NDs synthesized by traditional large-scale methods (i.e. grinding of HPHT crystals and detonation) typically require post-synthesis treatments, in order to purify them from non-diamond carbon and metallic impurities, and to make them suitable for applications. Some physical (annealing and etching) and chemical (acidic mixtures treatment) techniques will be discussed.

1.2.1 Annealing

When nanodiamonds are subjected to heat treatments (T less than 1800K), their surface can undergo the annealing phenomenon, i.e. the sp^3-sp^2 conversion of surface carbon atoms hybrid orbitals[5]. Annealing is a process that begins on NDs surface and continues inwards: a new graphitic-structured surface surrounds the central diamond core. (Figure 5).

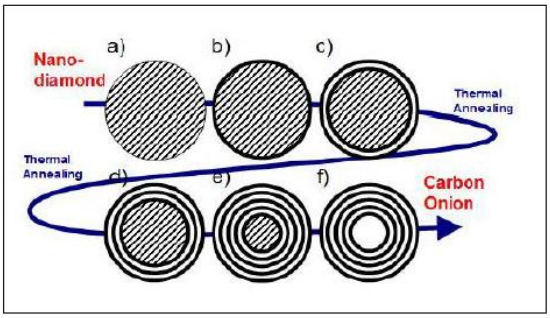

Figure 5. Graphitic surface progressive growth from the outside to the inside of the nanodiamond during the annealing process.

The total amount of surface sp^2 carbon atoms depends on the annealing temperature, the morphology and size of the nanodiamonds and the atmosphere in which the heat treatment takes place[18]. With the graphitization process nanodiamond minimizes the surface free energy at high temperatures[19]. A first graphene-like surface covers about 95% of the diamond core since after 2 picoseconds that the graphitization process has started; after 10 picoseconds the external surface no longer changes significantly, however the underlying layers in turn undergo the graphitization process[14]. Thus, the ordered structure of the core becomes progressively more disordered. For instance, after 800 picoseconds, a consistent layer of graphite covers the nanodiamond, the thickness of which depends on annealing temperature and time nanodiamonds were subjected to (Figure 6).

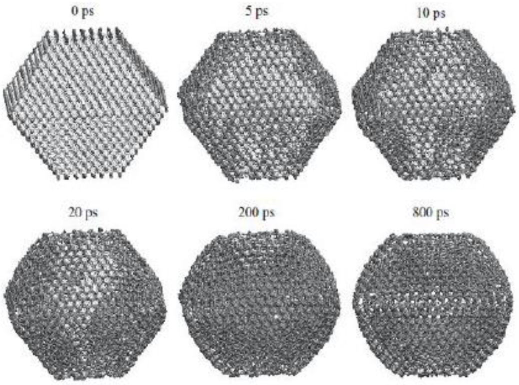

Figure 6. The annealing process led to progressive graphitization of nanodiamonds surface.

The obtained nanoparticles are often referred to as onion-like, because of the presence of a surrounding multi-layered graphitic shell[20]. Moreover, the speed of the graphitization process depends on the size of the diamond nanocrystals: crystals with smaller dimensions undergo the graphitization process more quickly, probably due to a greater curvature of the particle[2].

1.2.2 Etching

Etching is a physical phenomenon of removing nanodiamonds superficial graphite layers. It has been observed that annealing conducted on nanodiamonds in an oxygen-rich atmosphere tends to favour the oxidation processes of the C-C double bonds, rather than graphitization[2]. High energy surface “active” atoms trigger the high temperature mediated process. Analysis of electron transmission microscopy (TEM), scanning electron microscopy (SEM) and Raman spectroscopy have shown not only that the typology of nanodiamond surface transformation depends on the atmosphere to which the heating is performed, but also that the two processes take place at different temperatures: for instance, graphitization in argon occurs around 940K, oxidation in oxygen already occurs around 770K. It is also known that prolonged heating times in an oxygen-rich atmosphere cause graphitic surface component massive oxidation. This allows the introduction of new oxidized functionalities, in particular carboxylic groups, at the same time leading to a progressive reduction of nanoparticles diameter[21]. However more aggressive etching procedures can lead to the removal of surface closer nitrogen-vacancy centers[22], making necessary effective irradiation step for obtaining fluorescent nanodiamonds. Since air oxidation is particularly effective in removing graphitic surface layers it has the advantage of greatly suppress unwanted *sp*^{2} fluorescence background and graphite-mediated fluorescence quenching[23]. Furthermore, the partial removal of graphitic surface, after etching, makes nanodiamonds paler (Figure 7).

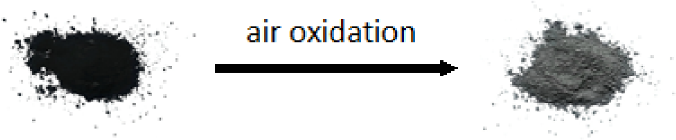

Figure 7. Etching procedure on 50 nm NDs make them paler because of partial removal of surface graphitic layers.

1.2.3 Chemical treatments

"Wet" chemical treatments are often used to remove impurities that nanodiamonds contain as a result of synthesis processes, especially detonation, such as detonation soot, graphitic carbon, metals and metal oxides[24,25]. The removal of these impurities facilitates the disaggregation process of the nanocrystals[26], enriches the surface with functionalizable carboxylic groups[27] and, by removing the graphitic component, can increase their fluorescence[28]. Typical mixtures are strong acidic oxidizing media and include HNO_3/H_2SO_4, $HNO_3/H_2SO_4/HClO_4$, H_2SO_4/H_2O_2, $K_2Cr_2O_7/H_2SO_4$[29].

1.3 Nanodiamonds characterization

Characterization of nanodiamonds is mainly carried out by means of solid-state analytical methods. Surface area measurements, thermogravimetric analyses, IR and Raman spectroscopy and electrophoretic mobility studies unequivocally allow to highlight dimensions, state of aggregation, surface characteristics or alterations of nanodiamonds structure. These techniques are exploited both for pristine and chemically functionalized materials, to verify the derivatization process and evaluate any changes in their chemo-physical properties.

1.3.1 BET

Brunauer–Emmett–Teller technique allows the measurement of the specific surface area of materials. The technique is based on the physisorption of gas with very low boiling temperature (nitrogen is the most commonly employed, but carbon dioxide, argon or krypton can be used as well), which led to nanodiamonds weight increasing[30]. Taking advantage of the known volume and surface of gaseous molecules employed it is possible to correlate the nanomaterial increment in weight with the surface area.

Nanodiamonds have far larger surface areas than larger diamonds of equal mass. In particular, typical 30-100 nm detonation NDs subjected to annealing show high specific surface area between 400 and 600 m^2/g [31]. Moreover, specific surface area does not depend on nanodiamonds surface porosity, but rather on the density, that is heavily influenced by temperature and time nanodiamonds are subjected to annealing process.

1.3.2 Thermogravimetry

Thermogravimetry is based on the continuous record of the mass variations of a material as a function of time and temperature in a controlled atmosphere (typically argon, nitrogen or air)[32]. Heating causes modifications by means of decomposition or oxidation phenomena that involve bonds ruptures and formation of volatile products by pyrolysis. The result is expressed by thermogravigrams, with temperature on abscissa and percent mass variation on the ordinate. However, the information obtained from this analytical technique is limited as it relates only to semiquantitative data. Thermogravigrams derivatives profiles allow to identify the inflection point typical of grafted molecules thermal transition after pyrolysis. The study of these derivative profiles and the percent weight loss represent one of the most effective techniques to demonstrate the success of nanodiamonds surface derivatization reactions and to estimate surface loading[33,34,35,36] (Figure 8).

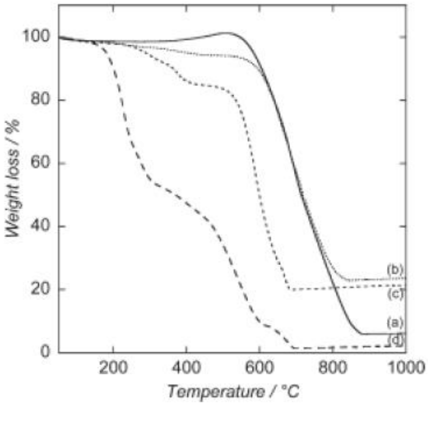

Figure 8. Example of thermogravigrams of functionalized nanodiamonds under air atmosphere[36]. a) ND-OH, b) ND-N_3, c) NDs functionalized with an alkynilpyrenic probe, d) NDs functionalized with an azido-modified dopamine.

1.3.3 Infrared spectroscopy

Nanodiamonds surface can be studied through the analysis of the IR spectrum. Different functional groups undergo vibrational relaxation phenomena, different in terms of intensity, mechanism, and energy. It is important to remember that IR spectroscopy, despite giving important structural information, is nevertheless used as a confirm tool for surface characteristics, since different vibrational phenomena can originate overlapping bands and peaks and making the interpretation of the spectrum not always easy[37]. For instance, IR spectroscopy allows to highlight the presence of water molecules adsorbed on bare nanodiamonds surface (typical bending and stretching OH vibrations at 1630 cm^{-1} and 3400 cm^{-1}, see Figure 9)[38]. Furthermore, the signal at about 1700 cm^{-1}, typical of the stretching of the carbonyl group, can be diagnostic of the oxidized state nanodiamonds surface and of the synthesis techniques used to synthesize them, for example by detonation[37].

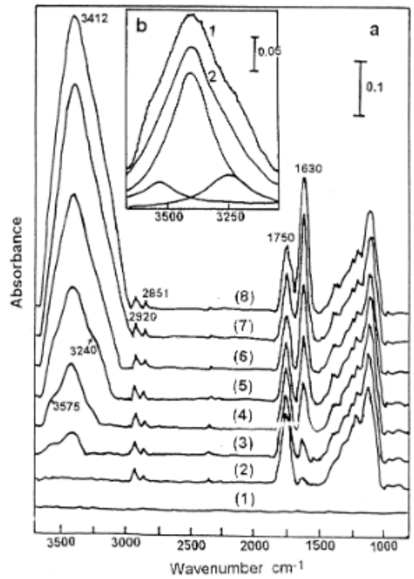

Figure 9. FTIR spectra of nanodiamonds after exposure to air over increasing periods of time (2-8). Typical OH signals at 1630 cm^{-1} and 3400 cm^{-1} and 1750 cm^{-1} carbonyl signals increase as the period of air exposure increases.

Moreover, besides to highlight different surface characteristics of nanodiamonds, IR spectroscopy can also confirm the presence of surface grafted molecules[34,39] (Figure 10).

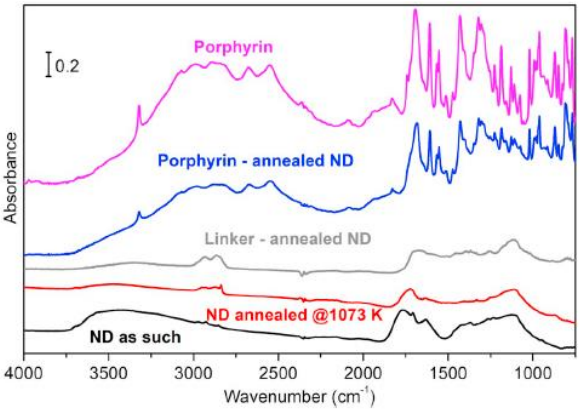

Figure 10. FT-IR spectra of bare and functionalized NDs. Untreated (black), annealed (red), amino-linker-functionalized (grey) and porphyrin-linker-functionalized (blue) NDs[39].

1.3.4 Raman spectroscopy

Raman spectroscopy is another characterization methods of NDs, as it is now commonly used to characterize all carbon materials and carbon nanostructures from three to zero dimensions (3D, 0D): 3D graphite or diamond, 2D graphene, 1D carbon nanotubes, and 0D fullerenes[40,41]. This kind of spectroscopy has also the ability to distinguish between different forms of amorphous carbon-based materials[42]. Furthermore, in some specific cases, Raman spectroscopy can also be used to study surface modifications of carbon materials, in particular when strongly conjugated molecules are grafted[43]. As regards nanodiamonds, it is possible to distinguish some diagnostic bands attributable to different surface features following different post-synthesis oxidation procedures[44]. Some main bands are observed, in particular the so called “D-band” and “G-band” (Figure 11):

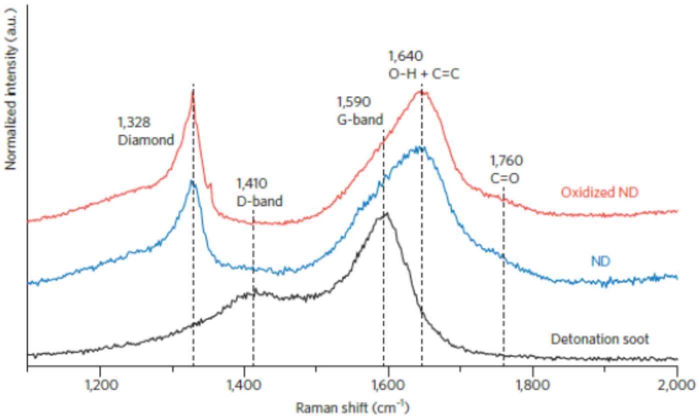

Figure 11. Typical Raman spectra of non-functionalized nanodiamonds, subjected to post-synthesis oxidation treatments.

The D-band is typically in the range between 1310 cm^{-1} and 1450 cm^{-1}, it is often named as the "disorder band" and it is characteristic of the amorphous component.

The G-band is typically in the range between 1520 cm^{-1} and 1610 cm^{-1}, it is referable mostly to the graphitic portion, the sp^2 component. This peak is evident in detonation nanodiamonds not purified by soot, and it is absent in nanodiamonds that have been subjected to surface oxidation process.

1.3.5 DLS and zeta potential

NDs surface electrical charge and potential are key features in order to better understand the tendency of nanodiamonds to aggregate, to interact with proteins[45], drugs[46] and their ability to penetrate in to cells[47].
DLS (dynamic light scattering) and ZP (zeta potential) measurements have gained popularity as simple, easy and reproducible tools to ascertain particle size and surface charge[33].

Zeta potential is the mostly exploited technique to characterize electrostatic charge of nanodiamonds. There are various charging mechanisms giving rise to zeta potential, such as dissociation of surface chemical groups, their dipoles and electron affinity differences[48]. It is measured by applying an electric field across the media in which nanodiamonds are suspended and monitoring nanoparticle migration velocity, typically by Dynamic Light Scattering (DLS). Measurements of zeta potential on NDs as a function of pH showed that oxidized ones have negative zeta potential within the full range of pH while graphitized nanodiamonds have positive values up to pH=12, because the graphitic planes at the surface leave oxygen-free base Lewis sites, which catch the acidic protons gaining a positive charge and so promoting the suppression of acidic functional groups present in the medium (Figure 12)[49,50]. Zeta potential has therefore high importance for mutual nanoparticle interactions in solutions. For instance, it influences the stability of NDs' colloidal solution and their assembly on surfaces[51].

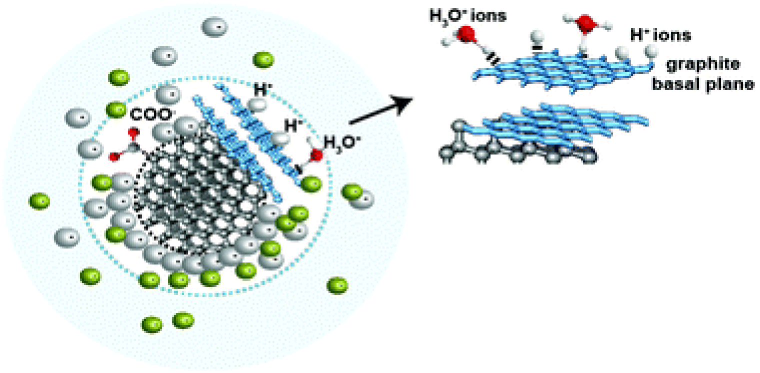

Figure 12. Graphitized nanodiamonds adsorb positive charges (protons) on basic Lewis sites and this results in positive values of zeta potential[49].

1.4 The Nitrogen-Vacancy center

1.4.1 Electronic structure

Nitrogen-Vacancy centers are crystalline imperfections in diamond lattice, consisting of a substitutional nitrogen atom (N) combined with a vacancy (V) in a neighbouring lattice site of the diamond crystal[3]. The NV center has a very peculiar electronic structure. Besides contradictory results have been obtained among years and a full understanding of NV^- most remarkable properties is still lacking, recently, a general NV center model has been accepted[52]. According to this model, NV center contain six electrons, five of them being electrons unpaired between the vacancy (the three nearest carbon atoms and two electrons belonging to nitrogen atom), plus an additional electron trapped at the defect center. The electronic state of NV centre can be described by means of molecular orbitals constructed according to complex group theory rules[53], as combinations of sp^3 orbitals of the vacancy nearest carbon and nitrogen atoms (Figure 13A).
More in detail, depending on its charge state, NV centers exist as six electrons negatively charged (NV^-) or as neutral five electrons (NV^0) defect[4]. The NV defect is a luminescent colour-center that absorbs in the wavelength range of 460–600 nm. The defect when excited by green light (532 nm) gives broad fluorescence emission in the near-infrared region with maximum centred on 680 nm. Under blue or green light excitation, photoluminescence (PL) is moved in the red and in near infrared domains, with characteristic narrow lines at 637nm (NV^-) and 575nm (NV^0), called “Zero Phonon Lines” (ZPL), followed at higher wavelengths with a broad band (see Figure 13B).

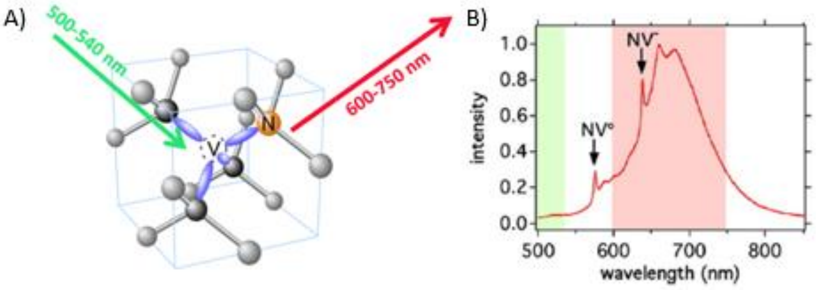

Figure 13. A) Model structure of a NV^0 [3]. B) Typical NV^0 575 nm and NV^- 637 nm fluorescence emission frequencies.

The multi-electron states at room temperature are separated in to a triplet level (spin S=1), in which is possible to identify a ground state called $^3A_2$ and an excited state called ^3E, and a singlet level (spin S= 1/2), containing an excited $^1A_1$ and a ground state ^1E[4]. At room temperature, in both excited and ground state levels, three spin levels exist, ms=0, ms=+1 and ms=-1, the last two being degenerate in absence of external magnetic field (see Figure 14).

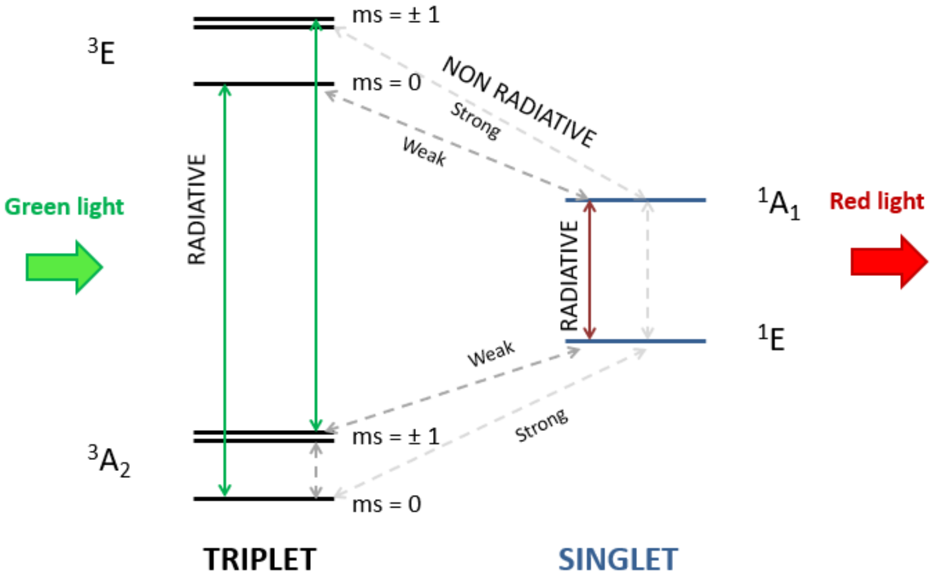

Figure 14. Electronic diagram of a negatively charged NV center.

As regards NV$^-$, for the ground $^3A_2$ triplet level, the spin-spin interaction is responsible for a zero-field splitting (ZPL), leading to a separation between ms=0 and ms=±1 of 2.88 GHz (in the microwave domain). Radiative transitions are responsible for optical phenomena and involve triplet-triplet or singlet-singlet electrons transitions. The previously mentioned ZPL originates from the excited triple state $^3E \rightarrow {}^3A_2$ transition. Non-radiative transitions may exist as well, when intersystem-crossing-like phenomena occurs, and they can be strong or weak, which means more frequent or less frequent to occur respectively, depending on whether the transition is relative to ms=0 or ms=±1[52].

The most exploited electronic transition is the one relative to triplet states, because the $^1E \leftrightarrow {}^1A_1$ singlet transition is about four orders of magnitude weaker than $^3E \leftrightarrow {}^3A_2$[54]. So, under 532 nm green light irradiation, NV center electrons in the $^3A_2$ ms=0 level decade mainly in a radiative fluorescent manner, in minor part following a weak IR radiative pathway involving intersystem crossings. This initial excitement and fluorescence recording step is called initialization step (or electron pumping), in the sense that the observed red emission fluorescence almost all arises from the ms=0 electron population. A steady state population of the three sublevels is generated, and emission fluorescence is collected.

NV center shows peculiar radiation lifetimes values, depending on nanoparticle size. Being NDs smaller than NV emission wavelength, the dimension of crystal lattice deeply influences the way the excited NV center decays in a non-radiative manner, so following a non-radiative channel[55]. For instance, radiative lifetime of NV^- in nanodiamond is broadly distributed in the 10-40 ns range with the most frequent value being 33 ns for 100 nm sized nanoparticles and 28 ns for 25 nm ones[56].

1.4.2 NV centers interactions with magnetic noise

NV centers' fluorescence emission properties can be altered by external magnetic fields[57,58] or temperature[59]. These alterations allow to understand dipolar interactions that occur between nanodiamonds and the surrounding environment, by means of Optically Detected Magnetic Resonance (ODMR) and T_1 experiments.

The ODMR experiment

When NV centers are irradiated with a particular frequency, a redistribution of spin polarization between ms=0 and ms=±1 may occur. More in detail, electrons in the triplet ground state $^3A_2$ are promoted from ms=0 to the ms=±1 spin level. At the same time, the light irradiation causes electrons transition in the excited state ^3E, without altering the spin level. Differently from ms=0, in this case, the return to the ground state mainly follows a non-radiative pathway, leading to a global reduction in photoluminescence. For the triplet ground state situation and at room temperature, the difference in energy between the two spin levels corresponds to a frequency of 2.88 GHz for a NV^- center[60] (Figure 15).

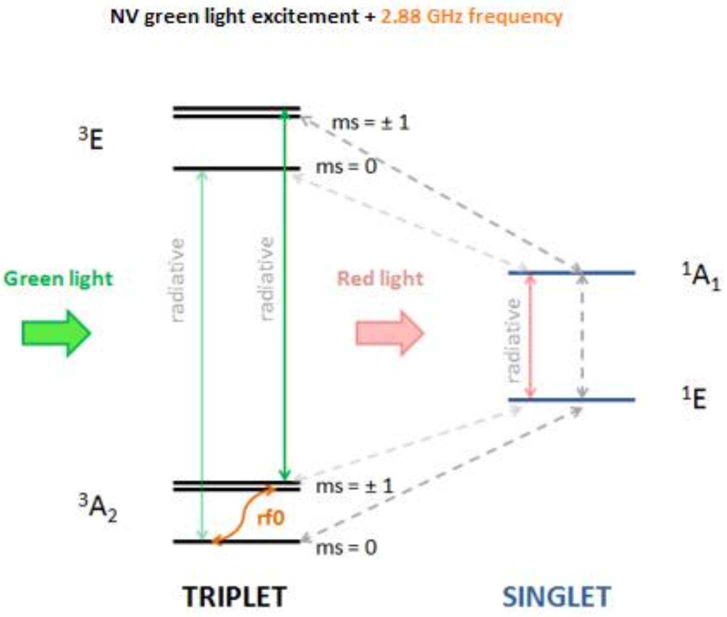

Figure 15. Electronic diagram of a negatively charged NV center, under irradiation with 532 nm green light and a 2.88 GHz microwave.

Irradiation with microwaves (or application of magnetic field B) lead to Zeeman effect: the two spin states m=+1 and ms=-1 are splitted in two states, different in energy, thus they are not degenerate anymore. Application of a resonant microwave field between the couple of sublevels (ms=0 → ms=-1 and ms=0 → ms=+1) will lead to a redistribution of their populations because a new steady state will be generated by the presence of the microwave field (see Figure 16). Thus, now there are two different frequencies, resonant with spin level transitions: one promotes ms=0 → ms=+1 and the other promotes the ms=0 → ms =-1; the light excitement promotes the transition from the triplet ground state to the triplet excited state. Independently from the spin level ms=+1 or ms=-1 of electrons in the excited state, the return to the ground state still follows a non-radiative way, leading to a decrease in red emission fluorescence.

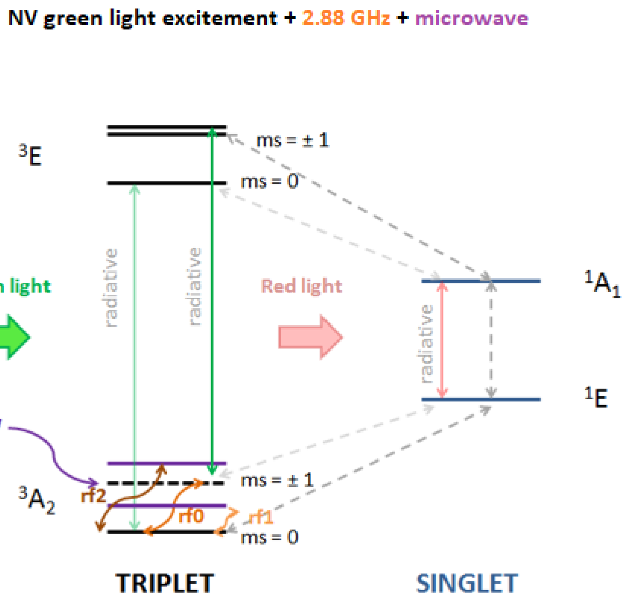

Figure 16. Electronic diagram of a negatively charged NV center, under irradiation with 532 nm green light, 2.88 GHz microwave and a microwave (or B magnetic field) leading to Zeeman Effect.

Thus, upon a frequency sweep of microwave driving field, a decrease of the fluorescence indicates when the microwave frequency is resonant with either the ms=0 → ms=+1 or the ms=0 → ms=-1 transition. So, in a ODMR experiment the sample is continuously illuminated and irradiated by microwaves at a frequency not far from one of the resonance frequencies.

In Figure 17 is shown a simple ODMR experiment: without external magnetic field (B=0) the microwave frequency is slowly scanned while the sample fluorescence is being monitored. When it approaches the resonance frequency, the fluorescence will be diminished depending on the relative values of the populating and decaying rates. Applying an external magnetic field, the Zeeman effect is observable by fluorescence intensity reduction at characteristic polarization frequencies[61]. In other words, applying a precise microwave it is possible to determine external magnetic field values from measured Zeeman effect[62].

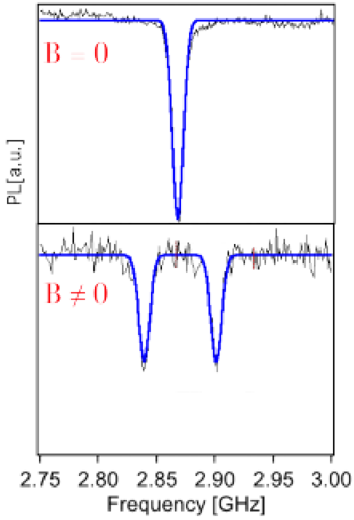

Figure 17. Typical ODMR experiment, in which the NV center characteristic photoluminescence reduction at 2.88 GHz frequency is shown (B=0). Applying B≠0 the Zeeman effect can be revealed.

Moreover, from the resonant frequencies of the ODMR, also temperature[63,64] and electric fields[65,66] can be estimated. Optically detected magnetic resonance can be exploited also as imaging technique for high resolution imaging of fluorescent nanodiamonds in tissues[67].

The T_1 experiment

A nitrogen-vacancy center population initialized to a ground-state magnetic sublevel emits fluorescence with a particular decay lifetime, the longitudinal spin-lattice relaxation time T_1[68]. Since its T_1 is deeply influenced by external magnetic fields[69] and temperature[70], NV center can be exploited as a probe for biological systems[71,72].

In Figure 18 a photoluminescence decay profile and a particular pulse sequence in order to perform the T_1 experiment[73] are shown.

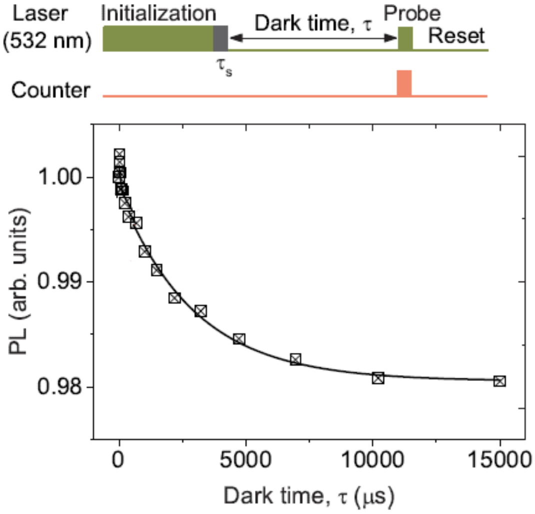

Figure 18. Pulse sequence used to study spin relaxation time (top). Photoluminescence (PL) decay profile as a function of dark time τ (bottom, adapted from ref. 61).

- Laser pulses (500 μs) is used to initialize NVs and the photoluminescence emission reaches an equilibrium state;
- the green laser is switched off and fluorescence is measured after variable dark time (τ); here external magnetic fields, temperature or electric fields can alter the fluorescence decay profile;
- a reset time is introduced to enable the system to reach equilibrium.

T_1 values and PL decay profiles also depend on NV centers density within the diamond lattice.

Considering the simplified energy levels of a NV center, T_1 can be calculated from the evolution of photoluminescence intensity signal as a function of dark time[74]:

$$I(\tau) = I_{eq}\,[1- \alpha(I_p)e^{-\tau/Tr} + \beta(I_p)e^{-\tau/T1}]$$

The photoluminescence intensity I depends on photoluminescence at equilibrium (I_{eq}), laser intensity (I_p), relaxation time of populations in the m_s=0 state (T_1), dark time (τ) and some important factors (α, β and T_r) related to dynamics that may occur during the fluorescence decay, the so-called spin and charge dynamics.

Spin dynamics and charge dynamics

ODMR and T_1 experiments are based on the principle that the measured fluorescence depends on electronic transitions, which in turn depend on electron spin dynamics influenced by external environment (magnetic fields, temperature…). Such experiments almost always measure NV^- fluorescence instead of the NV^0 one[75], because NV^0 centers have different electronic and spin energy levels and different fluorescence properties, often hard to interpret[76]. When NV electrons are excited by laser radiation they may undergo to photoionization phenomena, changing the defect charge state, usually from NV^- to NV^0 [73,77].

The changes in a general defect charge state are called charge dynamics. The fluorescence decay observed after laser irradiation and collected in the dark reflects the interplay between NV charge dynamics and spin dynamics (Figure 19).

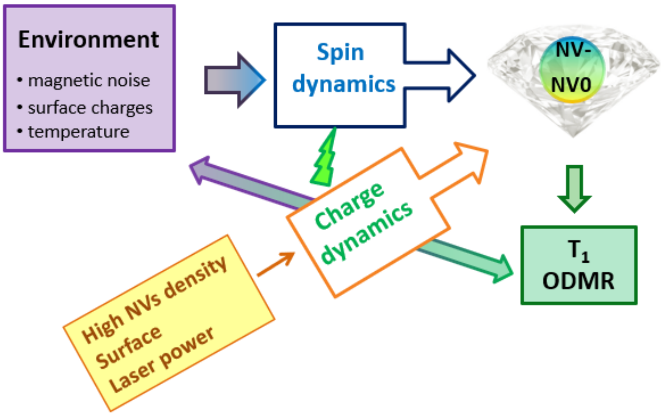

Figure 19. The interplay between spin and charge dynamics can alter the study of NV centers interaction with environmental parameters by means of ODMR and T_1 experiments.

The study of the charge dynamics is important in NDs fluorescence characterization because they can have a detrimental effect in the spin relaxation measurements. Variations in excitation laser power and magnetic field led to complex processes involving charge and spin dynamics during pumping, altering the shape of the classic exponential fluorescence decay (Figure 20)[78]. Charge dynamics may arise because of tunnelling among a network of closely spaced NV centers or among NV centers and nearby nitrogen atoms.

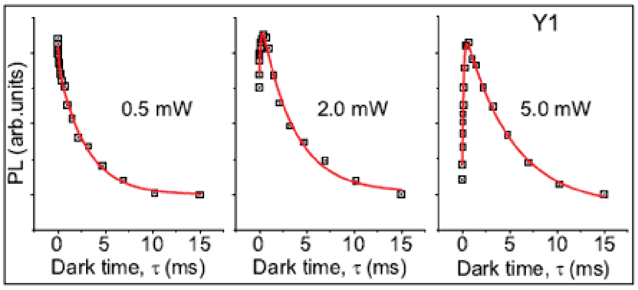

Figure 20. The increase of laser power alters the NV fluorescence emission decay profile, because charge dynamics start to prevail on spin dynamics.

Other factors, such as nitrogen defects, surface states, vacancies and other deep level defects, can influence the charge state stability of the NV center[79]. Moreover, also the intensity of the magnetic field applied to carry out both ODMR and T_1 can alter the balance between charge and spin dynamics[73]. Controlling the NVs charge state is fundamental because it can improve the sensitivity of detection. The presence of undesirable charge dynamics can alter fluorescence emission, spoiling T_1 and ODMR measurements. The study of these two complex phenomena is thus preliminary to the realization of such experiments.

Due to the effects of charge-state conversion on spin-relaxation measurements, controlling charge dynamics is then fundamental in the application of NVs as sensors, in particular for T_1-based sensing in biological systems, where high fluorescent NDs are required[80,81].

1.4.3 NV interactions with paramagnetic species

The alteration of the fluorescence emission profile measured with the T_1 and ODMR experiments makes nanodiamonds a tool for the detection and measurement of external magnetic fields. Paramagnetic species, such as gadolinium (III) and manganese (II) ions, generate local magnetic fields. The nature of the paramagnetic agent, its concentration and its distance from the NV center can alter the relaxivity Γ_1 of the NV centers. In fact, some studies on bulk diamonds show that Γ_1 increases with the increase of surface gadolinium ions concentration and with the reduction of the distance between the paramagnetic agent and the defect (see Figure 21)[82].

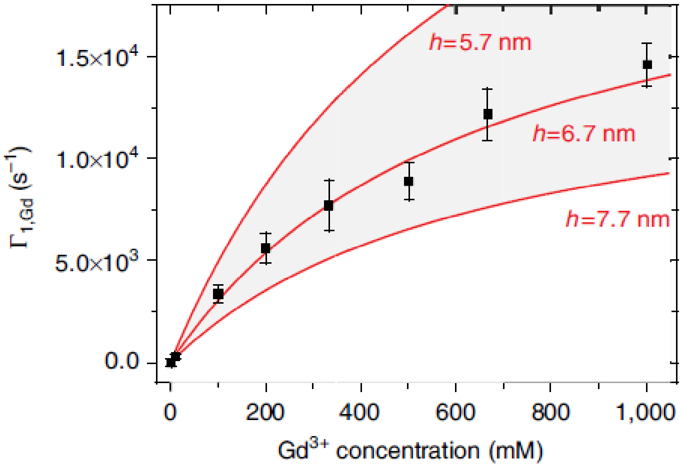

Figure 21. Dependence of diamonds NV centers relaxivity Γ_1 from gadolinium surface concentration and distance from the defect (ref 70).

Moreover, the T_1 of the NV centers exposed to gadolinium depends on the size of the nanocrystals and on the concentration of the paramagnetic species, both in solution[83] and grafted on the surface[84]. The dipolar interaction between gadolinium ions and NV can also be exploited for detection of gadolinium spin labels in an artificial cell membrane, in which gadolinium is covalently linked to phospholipids[71].

Recently, based on Gd-NV dipolar interactions, Rendler et al. adopted a single-step method to measure spin relaxation rates enabling time-dependent measurements on changes in pH or redox potential at a submicrometric-length scale in a microfluidic channel that mimics cellular environments[85].

The dipolar interaction between NV centers and other paramagnetic active species (e.g. Iron (II)) can be exploited to achieve similar results. Magnetic NDs fabricated implanting Fe(II) ions have been developed as a MRI contrast agent with negligible cytotoxicity[86].

1.4.4 Production of NV centers: ionic implantation

To be useful for previous described applications, nanodiamonds need to be as brightest as possible, so they should contain a great amount of fluorescent NV centers. The production of NV centers in nanodiamonds involves firstly the creation of vacancies by high energy particle irradiation, followed by high temperature annealing (800-900°C), that led to their migration and stabilization in lattice sites adjacent to nitrogen atoms. Most nanodiamonds are produced by grinding of HPHT diamonds; diamond naturally contain nitrogen impurities in place of carbon atoms[87]**.** The high energy (keV-MeV) particles employed for irradiation (electrons, protons, He^+ ions, sometimes neutrons) displace the carbon atom at interstitial positions, leaving vacancies. Depending on the ionic nature of the particles it is possible to get NV centers with different electronic state; for instance, NV^- are produced more easily by electron irradiation[4].

To efficiently produce NV^- center, reducing the formation of the neutral form NV^0, a certain amount of nitrogen impurities in the lattice is required. It has been demonstrated that a nitrogen concentration of a few hundred ppm is required[88]. The widely accepted NV^- formation mechanism, in radiation-damaged diamond, involves a three-steps reaction:

$$V^0 + 2N^0 \rightarrow NV^0 + N^0 \rightarrow NV^- + N^+$$

Under high temperature annealing, a vacancy can move in the rearranging diamond lattice, it reaches two aggregated nitrogen atoms and separates them, making a neutral NV center and leaving a lone neutral nitrogen atom in the lattice; this nitrogen electron donor, located in the proximity of NV^0, donates its electron to it, converting the neutral defect into its negatively charged form. Therefore, considering a 100 ppm nitrogen impurity concentration, the maximum reachable NV^- concentration should be 50 ppm[89], thus with a 50% conversion rate.

Two approaches are followed to produce a large amount of NV in NDs (figure 22):

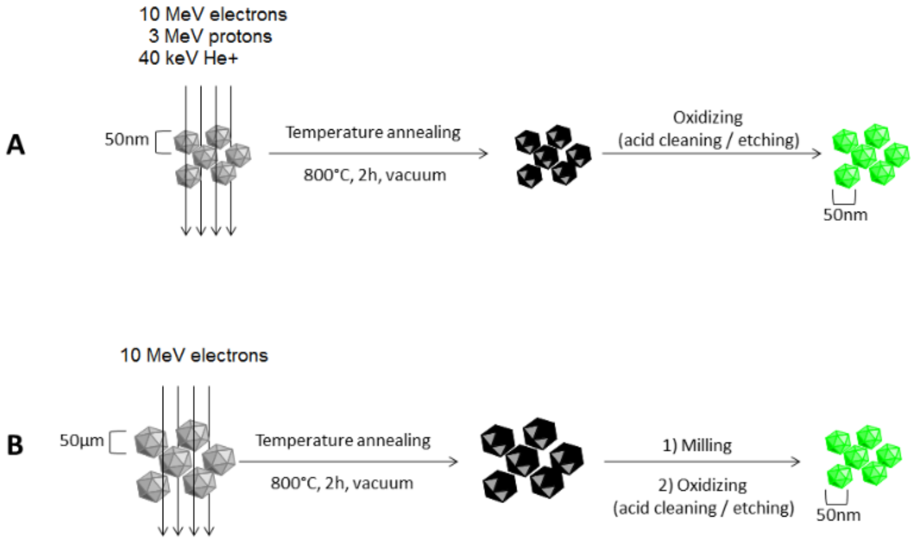

Figure 22. Approaches for production of fluorescent nanodiamonds: A) irradiation of nanodiamonds followed by annealing then etching, B) irradiation of microdiamonds, followed by annealing, grinding, then etching.

A) Direct irradiation and annealing of commercially available nanodiamonds. He^+, protons or electrons beam are employed for irradiation of nanodiamonds, previously deposited in a monolayer on a few meter-long copper ribbon that is slowly moved in front of the ion beam. Chang et al.[87] improved this technique using a 40 keV energy He^+ ion beam for irradiation of NDs with less than 50nm diameter. The 40 keV He^+ beam produces about 40 vacancies when it penetrates diamond, with respect to 3MeV H^+ that gives 13 vacancies; the bigger is the particle mass the higher is the penetration power. The irradiation step is then followed by vacuum 800°C annealing and 450 °C oxidation in air or strong acid cleaning, to remove the amorphous sp^2 graphitic layer.

B) Irradiation of microcrystals before their milling into nanocrystals. NV formation requires the migration of the vacancies during the annealing process, and applying this treatment to microcrystals instead of nanocrystals should reduce the annihilation of the vacancy at the surface[28]. However, this top-down production approach did not yield higher NV^- concentration, compared to direct irradiation of ND. The smallest reported fluorescent ND containing at least one NV^- center has size in the 5-10 nm range[90].

Since the ionic implantation requires peculiar facilities, NDs post-synthesis modifications by means of this procedure can be very expensive.

1.5 Nanodiamonds applications in biomedicine

NDs fluorescence, inertness properties and surface tunability can be exploited in biomedical field[14]. Their stable dispersion in a formulation medium[91,92], conjugation with biomolecules[93], biocompatibility[94,95] and ability to penetrate target tissues and cells make them suitable drug-delivery and targeting tools.

1.5.1 Drug-delivery

Various studies have been carried out to load therapeutic agents on the surface of NDs, in order to introduce them into biological systems, tuning their availability at the site of action. Many therapeutic agents of different classes such as antibiotics, anti-inflammatory agents and chemotherapeutic drugs have been successfully loaded onto NDs[96]. The latter include doxorubicin[46], epithelial growth factor[97], cisplatin[98], paclitaxel and cetuximab[99]. NDs-chemotherapeutics nanosystems proved to be efficient in suppressing tumor growth *in vitro*, triggering cellular-death mechanisms.

The grafting of these active molecules is not always covalent, but often based on electrostatic interactions that occur between drug and nanodiamond surface. For this reason, it is not easy to control the surface loading when non-covalent linkage is used (see Figure 23).

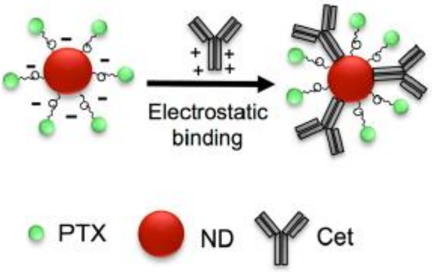

Figure 23. Synthesis strategy of NDs-paclitaxel (PTX)-cetuximab (Cet) nanosystems, exploiting electrostatic interactions between drugs and nanodiamond surface[99].

To improve the applications of nanodiamonds in this field, further studies of predictable and reproducible grafting are necessary.

1.5.2 Targeting and labelling

Fluorescent nanodiamonds are suitable fluorophores for labelling of low concentrations targets. The molar absorption coefficient for a single NV-center is reported as ε_{532nm}= 8.1x10^3 M^{-1} cm^{-1} [100]. For a 100 nm particle containing approximately 300 NV centers, the molar absorptivity of 2.43x10^6 M^{-1} cm^{-1}. Comparatively, the common fluorophore Alexafluor647 has a molar absorption coefficient of 2.7x10^5 M^{-1} cm^{-1}. It was first reported in 2005 that the far red fluorescence from NV^- -containing fluorescent nanodiamonds (FNDs) can be readily detected in live cells since it is well separated in wavelength from the autofluorescence (400-600 nm) of biological sample[101,102]. This characteristic makes nanodiamonds well suited as biomarker even at a single particle level.

NDs can be conjugated to different kind of proteins to label mammalian cells. For example, *in vitro* studies demonstrated that NDs-streptavidin and NDs-glycoproteins are useful respectively for breast cancer and liver cells labelling[103]. Cancer stem cells can be revealed with good sensitivity as well[104]. Moreover, NDs labelling can be performed also *in vivo* , as proved in recent studies on cervical cancer cells[105] and lung stem cells after transplanting in animal[106] (see Figure 24).

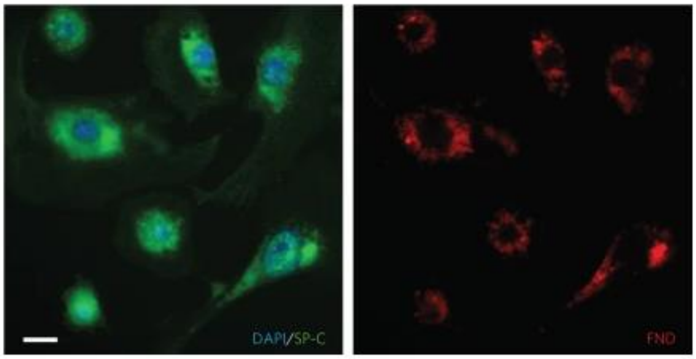

Figure 24. Wide-field fluorescence images of differentiated lung cells, revealed with immunostaining (green) and fluorescent nanodiamonds (red)[106].

1.5.3 Sensing

NDs can also be exploited as tools for highly sensitive sensing of all those cellular micro-environment alterations which modify their optical properties, such as temperature, magnetic fields and surface charges and that can be diagnostic for pathologies[10]. One of the most studied and monitored parameter is pH, because it can change nanodiamonds surface charges characteristics. More in detail, NV centers T_1 values depend on NDs surface charge state, which in turn depends on the pH of NDs surrounding media. It is possible to measure pH by measuring T_1 alterations based on it, exploiting protonation-deprotonation of natural carboxylic groups[6] (see Figure 25) or polymer containing amino-groups[107] on NDs surface.

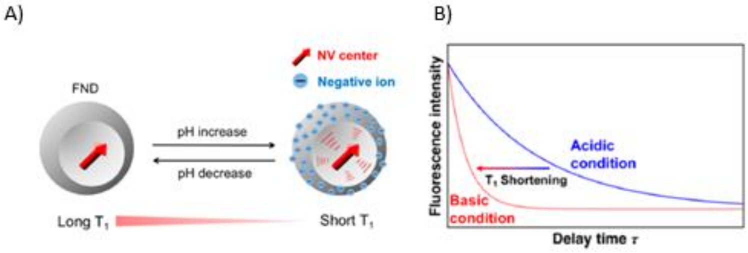

Figure 25. A) T1-shortening effect of increasing pH due to changes in surface carboxylic groups charge state. B) NV centers fluorescence decay profile in acidic and basic media[96].

Recently, ND-environment sensitive polymer-Gd hybrid nanoscale sensors have been made, in order to measure pH and redox potential. Changes in pH or redox potential led to hydrolysis or reductive cleavage of the specific polymer, moving Gd (III) away from NDs surface. It is possible to measure alterations in NV centers T_1 caused by the removal of surface Gd(III)[85].

1.6 Covalent surface modifications

The surface of a nanomaterial has a major influence on its actual properties. The lattice of nanodiamonds needs to be terminated in some way, otherwise dangling bonds would reach out of the environment. The most common terminal atoms are hydrogen[108] and oxygen[109] and the amount of each atom typology depends on nanodiamonds synthetic procedures.

Nanodiamonds subjected to post-synthesis annealing and etching treatments do not yet possess the surface characteristics suitable for applications in the biomedical field. The surface functionalization of nanodiamonds with any active species requires the presence of anchor points. The non-covalent interaction of nanodiamonds surfaces with biomolecules, such as peptides, has been known for several years. Oxidised diamond nanoparticles adsorb proteins and nucleic acids and polymers by hydrophobic and hydrophilic interactions[9,110]. However non-covalent functionalization is not always reproducible and tunable, differently from the covalent approach.

A lot of surface functionalization strategies have been carried out so far (see Figure 26)[12].

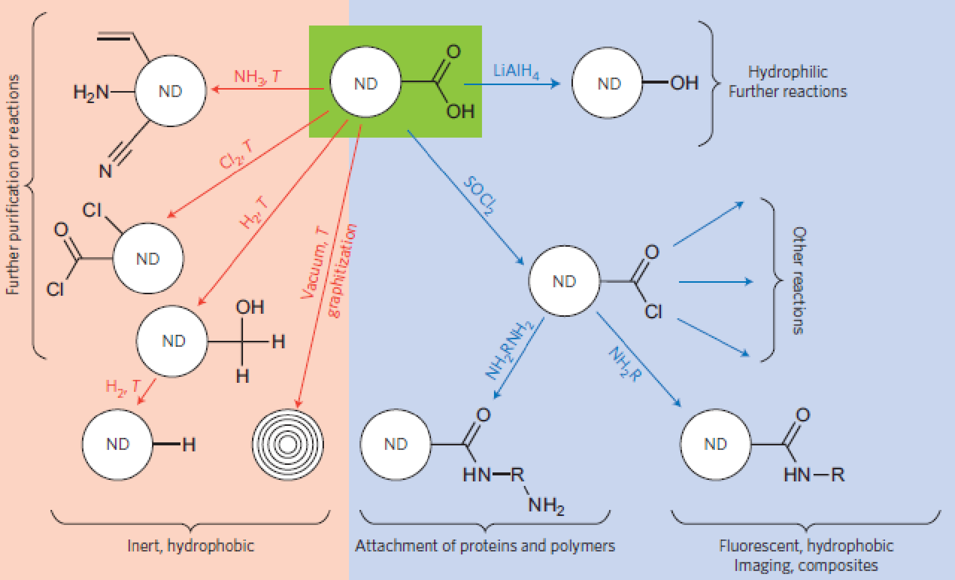

Figure 26. General nanodiamonds surface functionalization strategies, starting from the carboxylic groups, are carried out, leading to decoration with different moieties.

Surface functionalization can be used to directly decorate nanodiamonds with molecules of interest (for example proteins, dyes, polymeric chains[111]); this approach usually involves oxygen surface atoms. On the other hand, surface functionalization can introduce functional groups, which in turn are exploited in subsequent decoration with molecules of interest. This second strategy allows the introduction of heteroatoms other than oxygen exploitable for further conjugations, such as halogens[112], sulfur[113] and nitrogen[114]. It is the most used strategy because often the coupling of biomolecules directly on the surface could be not so successful for steric reasons, therefore the interposition of linkers between the surface and the biomolecule with more accessible moieties, are often required[115,116].

To better understand and tune the surface chemistry, it is important to distinguish between reactions carried out on functional groups already present, or possibly introduced through oxidation reactions of the graphitic surface, and reactions involving the graphitic carbon atoms.

1.6.1 Carboxylic surface

Surface carboxylic groups are particularly versatile. In fact, the ND-COOH surface can be modified with high temperature treatments in the presence of NH_3[117] to obtain amino derivatives, Cl_2 for chlorinated derivatives[118] or H_2 to obtain nanodiamonds with a partially reduced surface[119].

These functional group conversion offer the possibility to expand the decoration strategy of nanodiamonds surface with probes, drugs and other molecules of interest[120]. ND-COOH surface treatments with reducing agents such as $LiAlH_4$ allow to obtain functionalizable ND-OH surfaces. Treatment with $SOCl_2$ leads to formation of chloroacyl intermediates, which, when reacted with amino derivatives, lead to formation of the corresponding amide derivatives[121].

1.6.2 Graphitic surface

It is possible to exploit the increased graphitic surface of annealed nanodiamonds as a 2π component in cycloaddition reactions, for example the Diels-Alder cycloaddition and the [1,3] -dipolar ones.

Diels-Alder cycloadditions

A particular application of Diels-Alder cycloaddition on nanodiamonds subjected to thermal annealing is reported by Jarre et al[34],in which derivatives of ortho-quinodimethane, generated in situ starting from 1,2-bis (bromomethyl) benzene, are employed. In this study is demonstrated that the efficiency of the Diels-Alder reaction is closely related to nanodiamonds graphitic surface area. However, the Diels-Alder cycloaddition reactions carried out on nanodiamonds present the same problems as those carried out on fullerenes: the curvature of the π system on the surface of both nanomaterials does not particularly favour the diene-dienophile interaction and can lead to the removal of the diene from the surface adduct, through a retro Diels-Alder mechanism[122,123].

1,3-dipolar cycloadditions

1,3-dipolar cycloadditions represent a wide family of pericyclic reactions that can be applied to nanodiamonds modifications. For example, the Bingel-Hirsch cyclopropanation[124] and Huysgen cycloaddition[125] proved to be successful for the direct linking of organic moieties on diamond nanoparticles. Interesting results have been obtained in the formation of pyrrolidine or tetrahydroindolizine rings on graphitic NDs surface by mean of azomethine ylides[35] , according to the well-known Prato reaction on fullerenes[126].

The 1,3-dipolar cycloaddition can be also performed on nanodiamonds using N-protected amminoacids, such as sarcosine and different aldehydes as the precursors for the ylide formation (see Figure 27) [33].

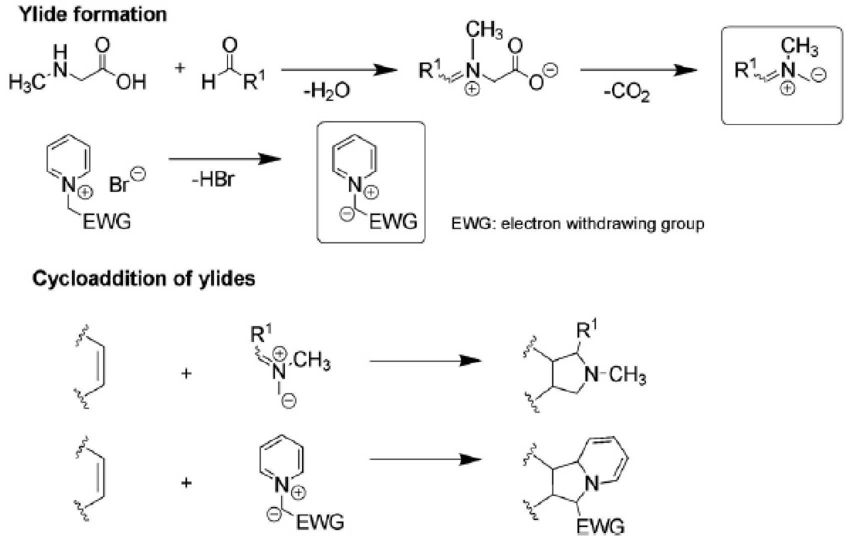

Figure 27. Examples of 1,3-dipolar cycloadditions of azomethine ylides generated by a) amminoacids (sarcosine) and b) N-alkyl pyridinium salts on nanodiamonds[33].

By means of this kind of reaction it is possible to introduce a lot of heteroatoms on nanodiamonds surface, first and foremost nitrogen.

2. THE AIM OF THE PROJECT

Unlike fluorescent bulk diamonds, NDs must have suitable dimensions and surface characteristics in order to interact with the biological environment. Since, following the already described synthesis techniques, these nanomaterials do not immediately possess the surface and fluorescence characteristics suitable for biological applications, post-synthesis physical and chemical treatments are necessary. Moreover, whereas the diamond-like core is inert, NDs surface is reactive and it can be modified by covalent attaching of tailored functional moieties. A lot of grafting strategies are based on a preliminary surface coating with polymers, leading to increasing dimensions and potentially limiting fluorescence exploitation. On the other hand, direct covalent modifications which involve carboxylic surface groups are not easily tunable, and the ones which involve the graphitic component are not usually exploited.

The aim of this project is the study and the modification of nanodiamonds carboxylic and graphitic surface in a uniform and tunable manner, in order to make them suitable for applications in diagnosis and therapy. From the diagnosis point of view, nanodiamonds can be exploited directly in sensing, by means of external magnetic field-dependent fluorescence, and indirectly, transferring magnetic polarization to metabolites. In therapeutic field nanodiamonds can be used as drug delivery systems, mutual prodrug tools and targeted nanosystems.

The idea is to tune nanodiamonds surface chemical characteristics, in a reliable and predictable manner, to improve these nanomaterials features, in particular, in all those applications where their fluorescence is exploited. Subsequent grafting of specific active species is useful to understand and modulate the interaction between fluorescence responsible NV centers and the surrounding environment, a crucial point for drug delivery, targeting and sensing purposes.

Of course, the first surface modification occurs by post-synthesis annealing and etching treatments, therefore they have been considered, characterized and tuned.

To enrich the surface of heteroatoms, in a reliable and predictable manner, pericyclic reactions on NDs graphitic component have been studied and optimized, in particular the Diels-Alder and 1,3-dipolar cycloaddition of azomethine ylides *in situ* generated by aminoacids. Then, further surface functionalization with active species has been carried out using:

- gadolinium and manganese complexes with the aim of better understand dipolar interactions between paramagnetic species and NV centers by T_1 and ODMR experiments;
- Porphyrins, which make the nanosystems potentially exploitable in photo and sono-dynamic therapy.

Carboxylic surface derivatization has been explored and tuned as well and it has been chosen for further grafting of monoclonal antibody for targeting and therapeutic purposes.

Given that NDs fluorescence is the key aspect that make these nanomaterials exploitable in the sensoristic field, also strategies to produce NDs rich in NV centers have been explored. The first strategy concerns the production of NDs intrinsically rich of NV center by laser ablation of graphite enriched with nitrogen atoms by means of chemical reaction. The second strategy exploits the ionic implantation of nanocrystals.

Because of the multidisciplinary nature of this project, the work has been carried out in collaboration with different research groups:

Istituto Italiano di Tecnologia: Center for Neuroscience and Cognitive Systems (A. Bifone, F. Gorrini)

Drug Science and Technology Department: group of Pharmacology (M. Gallicchio, V. Boscaro, R. Canaparo, F. Foglietta), group of Analytical Chemistry (O. Abollino, A. Giacomino)

Physics Department: group of Solid-State Physics (F. Picollo, P. Aprà)

Chemistry Department: group of Physical Chemistry (G. Martra, E. Rebba)

Department of Molecular Biotechnology and Health Sciences (A. Bifone)

3. RESULTS AND DISCUSSION

3.1 Nanodiamonds preliminary characterization

In order to choose the most suitable nanodiamond for applications in biomedicine, preliminary characterization studies were performed. More in detail, photoluminescence, specific surface area and nanoparticles diameters distribution studies on different kind of nanodiamonds are shown below.

3.1.1 Photoluminescence

Photoluminescence studies were carried out on 5, 50 and 250 nm nanodiamonds subjected to post-synthesis annealing (800°C, 2h, N_2 atmosphere) and followed by thermal etching (450°C, 30 min, air atmosphere). Figure 28 shows annealed nanodiamonds powders before and after etching treatment. The etching treatment causes the partial removal of graphitic surface layers, leading to brighter powders.

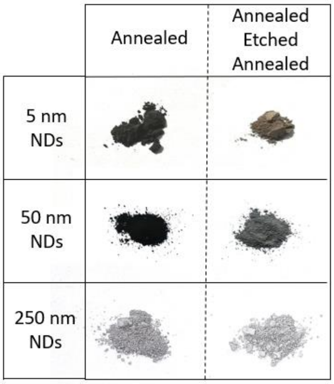

Figure 28. Powders of 5, 50 and 250 nm nanodiamonds subjected to annealing and annealing-etching-annealing treatments.

Raman photoluminescence spectra are reported in Figure 29.

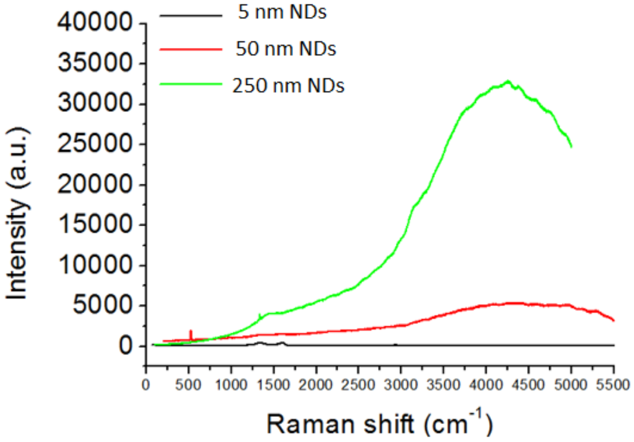

Figure 29. Photoluminescence spectra of 5 (black), 50 (red) and 250 nm nanodiamonds (green) subjected to annealing followed by etching treatments after synthesis.

The higher the diameter of the nanodiamonds, the greater their fluorescence. In fact, as the size, and therefore the volume, increases, the amount of NV centers responsible for the fluorescence increases. Since 5 nm nanodiamonds have almost null fluorescence they were excluded from this research project.

3.1.2 Specific surface area

Given that nanodiamonds must be modified for biomedical applications, specific surface area (SSA) plays an important role because it is the interface between diamond core and environment. Thus, SSA studies were performed on 50 and 250 nm NDs. In order to obtain very fluorescent nanodiamonds, the materials were subjected to annealing, etching, ionic implantation and finally to annealing treatments. We wondered if etching-annealing treatments that follow the initial annealing could alter these nanomaterials SSA. Annealed-etched-annealed NDs (aea) would simulate the case of annealed-etched-implanted-annealed ones. SSA-BET measurements are conducted on both annealing (a) and annealed-etched-annealed (aea) NDs (Table 1).

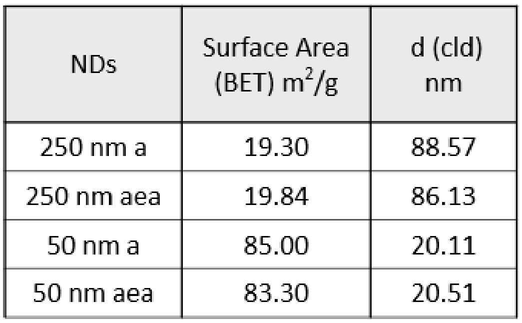

NDs	Surface Area (BET) m^2/g	d (cld) nm
250 nm a	19.30	88.57
250 nm aea	19.84	86.13
50 nm a	85.00	20.11
50 nm aea	83.30	20.51

Table 1. Surface area estimation and calculated diameter of 50 and 250 nm nanodiamonds subjected to annealing (a) and annealing-etching-annealing (aea) post-synthesis treatments.

Smaller nanodiamonds show higher surface area, as expected. Different post-synthesis treatments do not affect surface area significantly. Moreover, from measured surface area, nanodiamonds diameter are calculated, with some assumptions: nanodiamonds are perfectly sphere-shaped, they are not aggregated, and they have diamond density (3.51 g/cm^3). In this case, diameters seem to be smaller than the nominal ones, maybe because of irregular shapes of nanoparticles, or because of the approximation employed.

3.1.3 Scanning Electron Microscopy

SEM microscopy allows to obtain images with a resolution of a few nanometres, by which it is possible to extract information of a morphological nature and, having well-dispersed nanoparticles, a size distribution. SEM images of 50 and 250 nm NDs subjected to annealing are shown below (Figure 30).

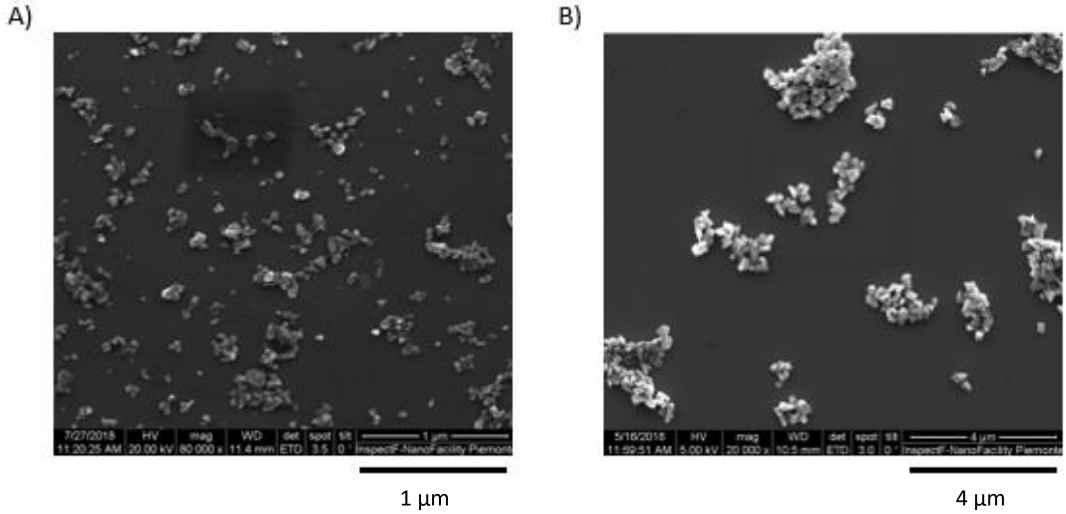

Figure 30. SEM images of 50 nm annealed NDs (A) and 250 nm annealed NDs (B).

SEM images confirm the irregular shape of both kind of nanodiamonds.
Dimensions were determined by means of ImageJ software. For 250 nm NDs it was possible to define a size distribution profile (Figure 31). Given the 50 nm NDs tendency to aggregate, size distribution analysis in this case was discarded, because it would have been too much approximative.

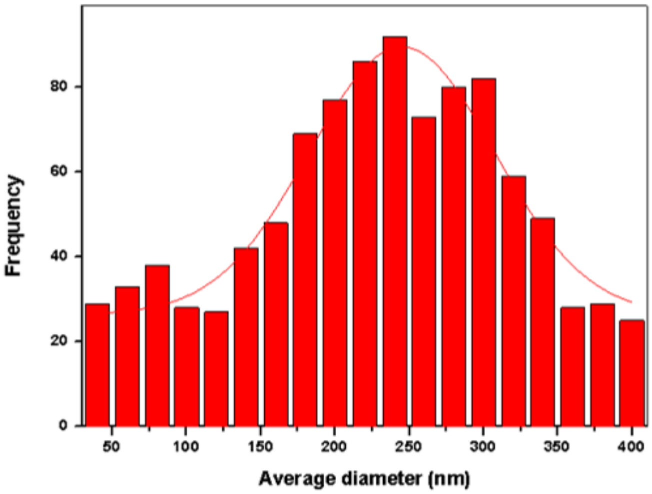

Figure 31. Diagram bars of the average diameter distribution of 250nm annealed NDs.

GRAPHITIC SURFACE FUNCTIONALIZATION: UNDERSTANDING MAGNETIC DIPOLAR INTERACTIONS

As described in the introduction, one of the interesting applications of nanodiamonds is related to the magnetization transfer from NDs to surface organic species. In order to better understand the interplay between surface molecules and ND core, we explored the dipolar interaction connecting NV centers and surface paramagnetic species, evaluating their effect on NV centers relaxivity at different distances from the surface. More in detail, we chose as paramagnetic probe a Gd complex, for the high paramagnetic moment of this metal, and Mn complex, whose paramagnetic properties depend on its redox equilibrium. The study needs to start from NDs surface functionalization with appropriate linkers, which was obtained by pericyclic reactions between appropriate substrate and graphitic ND surface. Then, paramagnetic complexes were grafted to the linker and the obtained ND-paramagnetic system were analysed in terms of T_1 and ODMR.

3.2 The Diels-Alder approach

3.2.1 Making the ND-linker nanosystems

The first step of diamond derivatization is then the insertion of an appropriate linker. On the basis of known procedures[39], we selected Diels-Alder cycloaddition between NDs graphitic surface and the furanic portion of *ad hoc* synthesized linkers with amino chains of different lengths (see Scheme 1) to reach this objective. 250 nm NDs subjected to annealing (a) and annealing-etching-annealing (aea) has been selected to simulate the more expensive implanted nanodiamonds, that should be employed in future further similar studies.

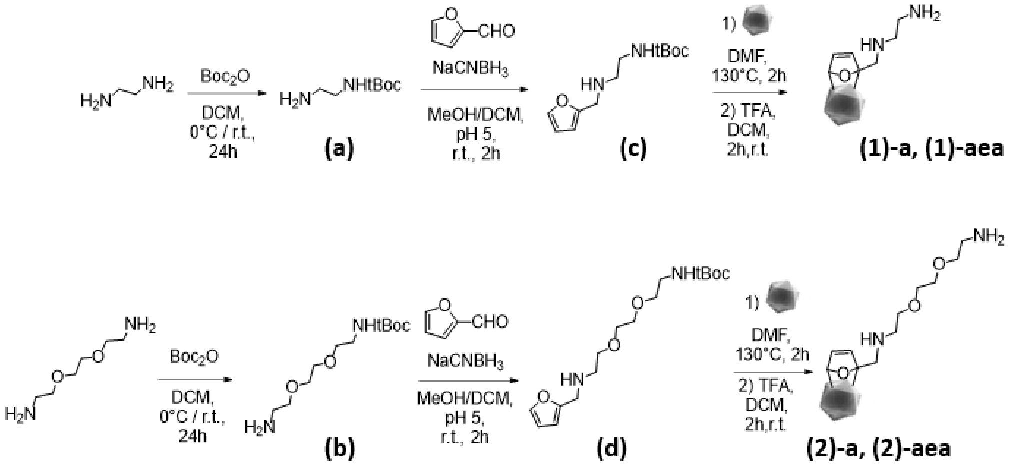

Scheme 1. Synthesis of the ND-linker nanosystems (1) and (2), annealed (-a) and annealed-etched-annealed (-aea). Short (c) and long (d) linkers are obtained from mono-boc protected short (a) and long (b) diamine, respectively.

The surface grafted linker amounts have been estimated by thermogravimetric analysis and shown in Figure 32.

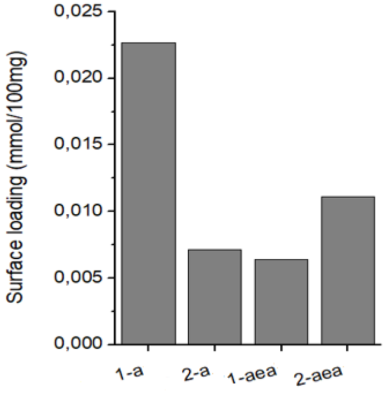

Figure 32. Diagram bars, showing NDs-linker surface amounts estimations. Errors are reported in Figure E2.

All thermogravimetric analysis were performed considering a weight loss error of ± 0.5%, calculated on thermogravimetric analysis of bare graphite.

NDs derivatization degrees with furanic linkers suggest that the cycloaddition efficiency is not related either to nanodiamond surface type (a *vs* aea), or to the amino chain length. The Diels-Alder cycloaddition reaction, due to its reversibility under the chosen reaction conditions, may not be the most suitable approach for NDs surface functionalization in a predictable and reproducible manner.

3.2.2 Making the ND-paramagnetic nanosystems

NDs-NH_2 nanosystems (1) and (2) were then grafted with paramagnetic species (see Scheme 2). More in detail, AAZTA (6-amino-6-methylperhydro-1,4-diazepine tetracetic acid) derivative (AAZTA(tBu)C_4COOH) and carboxy-EDTA (CEDTA(tBu)) derivative were chosen for Gd and Mn respectively, leading to NDs-AAZTA and NDs-CEDTA systems, with different length. Then, reaction with TFA and incubation with Gd (III) and Mn (II) solutions lead to NDs-Gd derivatives (7) and (8) and NDs-Mn nanosystems (9) and (10).

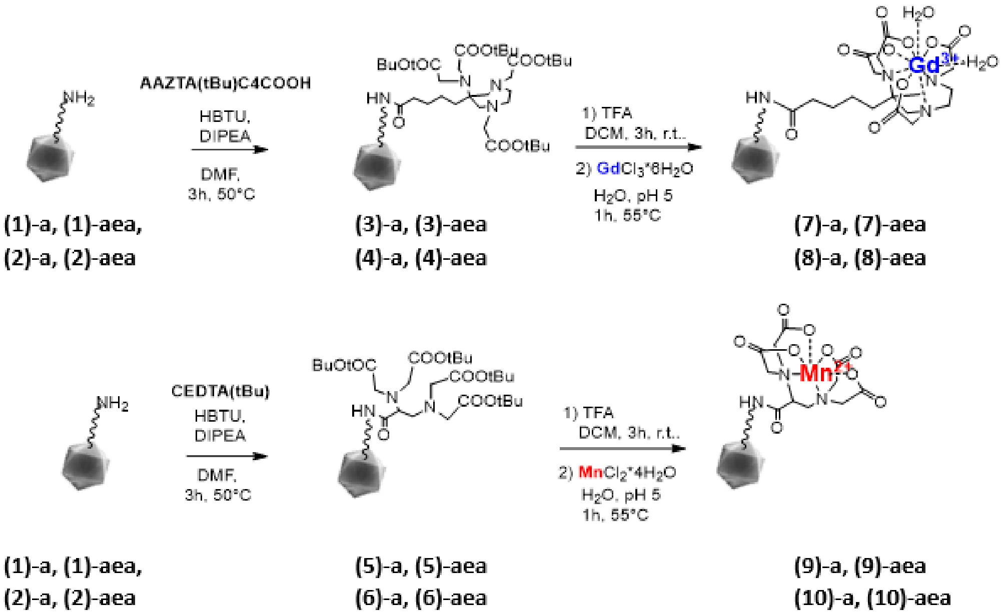

Scheme 2. Synthesis of NDs-Gd and NDs-Mn nanosystems. NDs-NH$_2$ grafting with AAZTA and CEDTA derivatives lead to NDs-AAZTA short (3) and long system (4) and NDs-CEDTA short (5) and long system (6). reaction with TFA and incubation with Gd (III) and Mn (II) solutions lead to Gd-(7), Gd-(8), Mn-(9) and Mn-(10).

By thermogravimetry of NDs-metal-complexes, paramagnetic species surface amounts have been estimated and depicted in Figure 33.

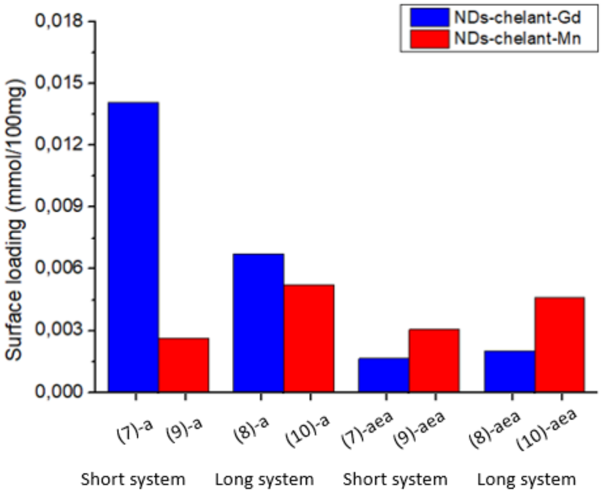

Figure 33. Diagram bars, showing NDs-linker surface amounts estimations. Errors are reported in Figure E3.

3.2.3 T_1 experiments on NDs-Gd nanosystems

Magnetic interactions between nanodiamonds and paramagnetic agents has been studied, in collaboration with Istituto Italiano di Tecnologia (IIT) of Rovereto. An experimental setup was realized *ad hoc*, a particular pulse sequence[78] was designed in order to measure NV centers fluorescence emission decay, from which, by means of a model equation, T_1 can be estimated (see Figure 34).

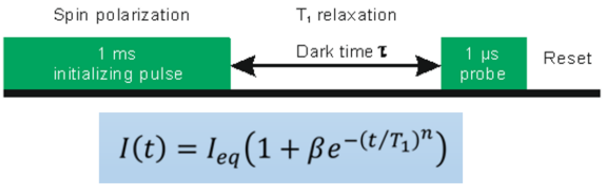

$$I(t) = I_{eq}\left(1 + \beta e^{-(t/T_1)^n}\right)$$

Figure 34. Pulse sequence employed in the T_1 experiments on NDs-paramagnetic nanosystems (top); correlation between fluorescence emission intensity and T_1 (bottom).

Bare nanodiamonds NV centers show a relaxation rate, r_1 (r_1=1/T_1), of 0.312 ms^{-1}. In Figure 35 relaxation rate (r_1) and Gd surface amounts are reported.

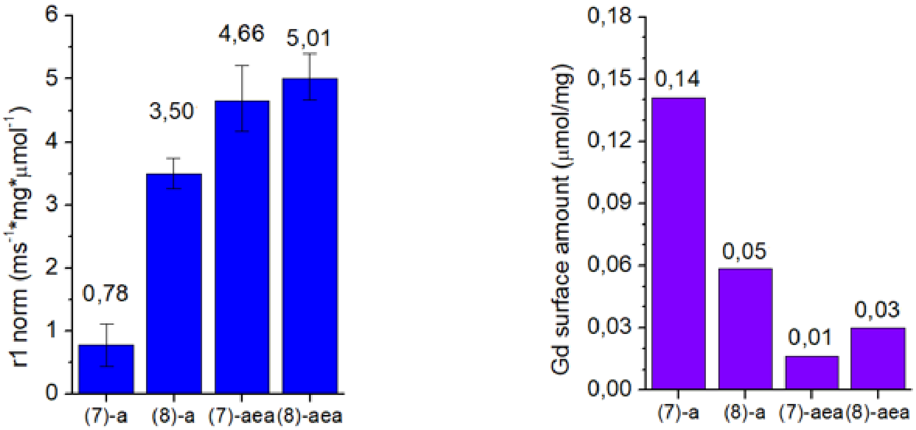

Figure 35. A) Diagram bars reporting relaxivity values of NDs-Gd nanosystems, normalized for surface Gd concentration. B) Gd surface concentration as reference.

It is well known that the T_1 value of an NV center depends on the concentration of paramagnetic agent in their proximity[127]. For this reason, a rational evaluation requires the normalization of r_1 values for Gd surface amount. Long chain systems Gd (8)-a and Gd (8)-aea relax faster than shorter chain ones Gd (7)-a and Gd (7)-aea. This is unexpected, since the dipolar effect is directly related to distance[128]. This trend can be explained by assuming a sort of folding of the long linker on the diamond surface, which would bring the paramagnetic agent closer to the surface, whereas the folding of short chain is harder. The shorter NV-Gd results in a higher relaxation rate, and therefore higher relaxivity.

More interestingly, r1 still depends on the amount of Gd on the surface, even after normalization. In fact, keeping constant the chelating system chain length, the higher the gadolinium density, the slower the system relaxes (7-a vs 7-aea and 8-a vs 8-aea). This can be explained by assuming a sort of dipolar interaction between gadolinium ions, reducing paramagnetic activity, differently from what it is expected. Further studies are necessary to better understand this aspect.

In any case, gadolinium generates magnetic noise, which causes a general increase in relaxivity. Moreover, relaxivity depends on paramagnetic species surface amount and on its distance from the surface, hence from NV centers.

3.2.4 T_1 experiments on NDs-Mn nanosystems

A similar study was conducted on NDs-Mn systems. The paramagnetic properties of the manganese ion depend on its oxidation state, hence on the redox potential of the surrounding environment. Each ND-Mn nanosystem was therefore subjected to two different treatments before T_1 measurement: a reducing treatment with sodium thiosulfate, which guarantees that all the manganese ions exist as paramagnetic Mn(II), and an oxidizing treatment with hydrogen peroxide, which lead to the diamagnetic Mn(III) (Scheme 3).

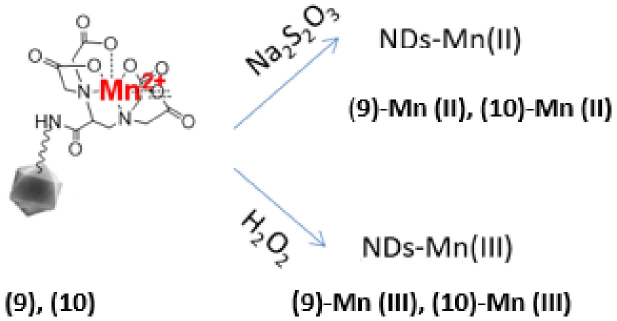

Scheme 3. Synthesis of NDs-Mn (II) and NDs-Mn (III) nanosystems, starting from short chain (9) and long chain (10) nanosystems.

The experimental setup and the pulse sequence adopted to measure T_1 were identical to those used in the case of NDs-Gd.

Since T_1 values of the four NDs-Mn systems are dispersed between 300 µs and 6 ms, with no clear trend, averaged measurements of NDs-Mn (II) and NDs-Mn (III) are shown in Figure 36.

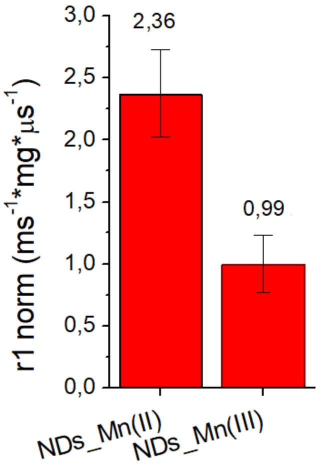

Figure 36. Diagram bars of relaxivity r1 values of averaged NDs-Mn (II) and NDs-Mn (III) systems.

Reduced samples have a higher r_1 than the oxidized ones. Moreover, both manganese nanosystems show higher r_1 than the bare samples (0.312 ms^{-1}). This could be due to uncomplete oxidation of Mn ion or to a different, not better identified, interaction between NV and metal center.
However, these experiments confirm the reduction of T_1 as consequence of reducing conditions which allow the generation of paramagnetic metal center.

These preliminary results indicate the importance to conjugate a rather high amount of the paramagnetic centers near the diamond. In other words, in order to understand how external magnetic noise and NV center influence each other and for extending NDs future applications in sensing or imaging, an efficient T_1 stimulation is required. This is possible only if a high probability of interaction between NV and paramagnetic species occurs.

The interaction probability between NV centers and paramagnetic species can be increased following these strategies (Figure 37):

- increasing surface paramagnetic amount;
- increasing NV centers amount (implantation with high energy beams);
- reducing NDs dimensions, that allow paramagnetics to be closer to the diamond core.

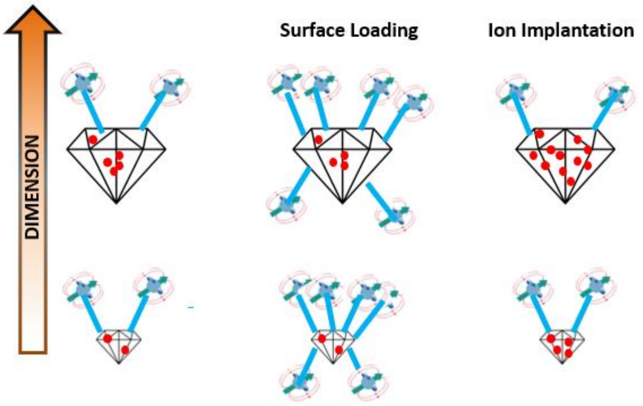

Figure 37. Strategies for increasing the probability of interaction between NV centers and paramagnetic species. Reducing NDs dimensions, increasing paramagnetic species surface loading or increasing the amount of NV centers.

We focused this study on increasing the paramagnetic surface amount, changing the linking chemistry, and reducing NDs dimensions (using 50 nm NDs).

3.3 The 1,3-dipolar approach to ND surface grafting

Since Diels-Alder cycloaddition was revealed to be not very reproducible on NDs, we explored the 1,3-dipolar cycloaddition of azomethine ylides generated *in situ* by selected amino acids onto 50nm NDs and 250 nm NDs (to be compared with the Diels-Alder strategy).

3.3.1 Azomethine ylides cycloaddition on NDs

The 1,3-dipolar cycloaddition were exploited to graft on NDs surface accessible amino groups useful for the secondary linkage of chelating agents (or any other suitable molecule). To this purpose we focused on paraformaldehyde and lysine as reagents (see Scheme 4).

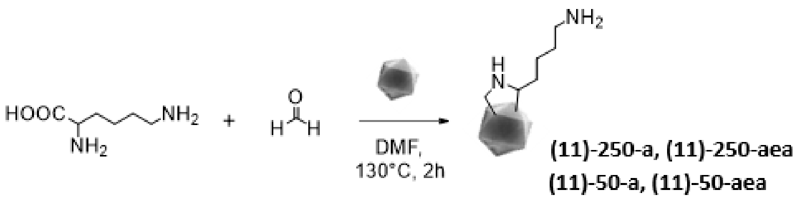

(11)-250-a, (11)-250-aea
(11)-50-a, (11)-50-aea

Scheme 4. Performing the 1,3-dipolar cycloaddition of azomethine ylides generated from lysine and paraformaldehyde on 50nm (“50” systems) and 250 nm (“250” systems) nanodiamonds, subjected to annealing (“a” systems) and annealing-etching-annealing (“aea” systems) treatments.

According to the previously shown strategy, this cycloaddition reaction were performed also on 50 nm (“50” systems) annealed (“a” systems) and annealed-etched-annealed (“aea” systems) NDs.

The grafting efficacy of the aminic linker by means of 1,3-dipolar (11) and Diels-Alder (2) cycloaddition on annealed and annealed-etched-annealed 250 nm NDs (NDs-NH_2-a and NDs-NH_2-aea) was estimated by TGA (Figure 38).

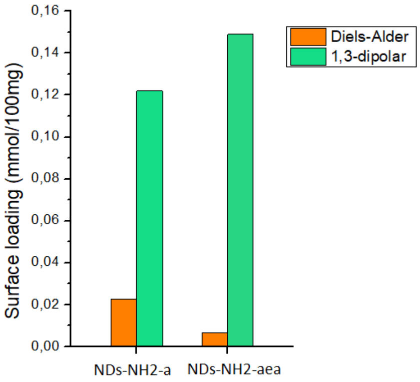

Figure 38. Surface loading estimation of amino linkers introduced on 250nm annealed (NDs-NH_2-a) and annealed-etched-annealed (NDs-NH_2-aea) by means of 1,3-dipolar (green) and Diels-Alder (orange).

Dipolar cycloaddition reaction is more reliable and reproducible than Diels-Alder strategy. This is reasonable due to the reversibility of the last reaction.

3.3.2 Conjugation with paramagnetic species

250nm and 50 nm NDs-NH_2 were conjugated with the previously mentioned chelating agents obtaining NDs-chelator (12) and (13). Reaction with TFA and the subsequent incubation with the paramagnetic species lead to NDs-Gd (14) and NDs-Mn (15) nanosystems (see Scheme 5).

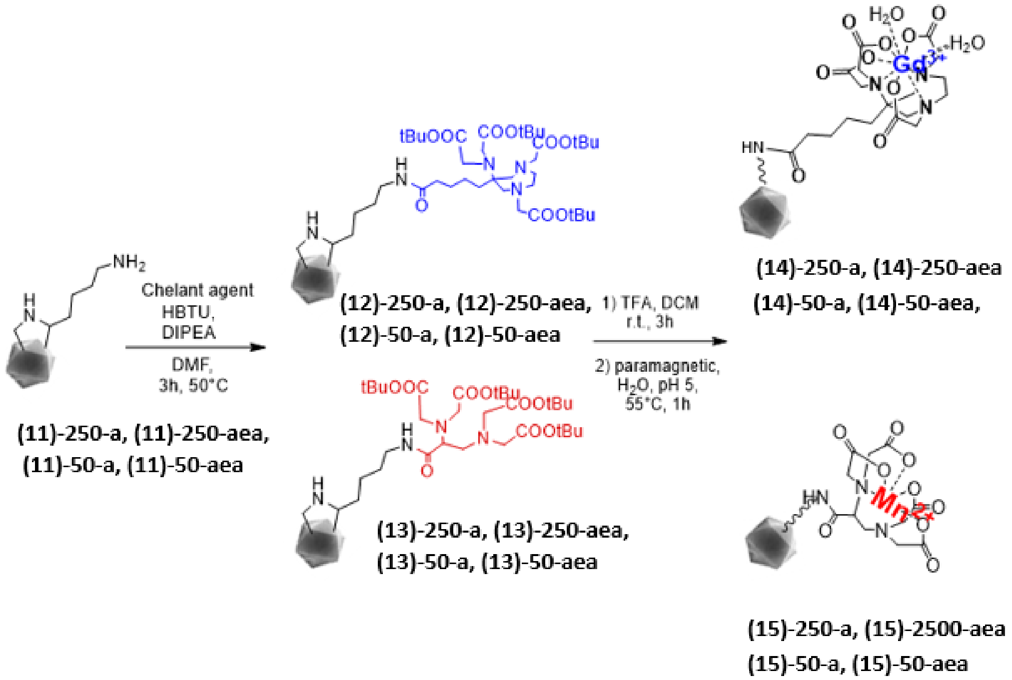

Scheme 5. Synthesis of NDs-chelant (12) and (13) nanosystems and subsequent synthesis of NDs-Gd (14) and NDs-Mn (15) nanosystems.

Figure 39 shows chelant agents surface graftings, estimated via thermogravimetry.

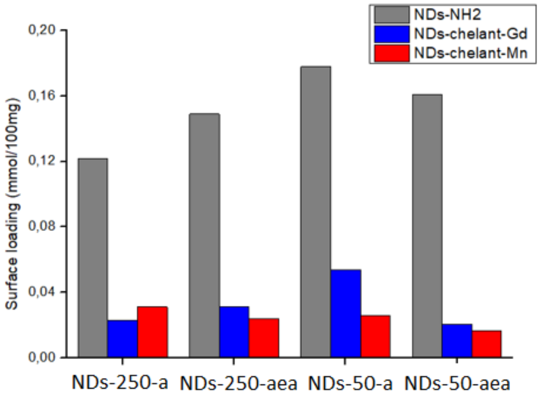

Figure 39. Diagram bars showing chelant agents surface loadings, following the 1,3-dipolar cycloaddition strategy. Errors are reported in Figure E4.

The aminic linker grafting by means of 1,3-dipolar cycloaddition of azomethine ylides proved to be reliable and quite reproducible also on 50 nm NDs, as well as the subsequent conjugation with chelating agents. However, not all the amino groups introduced by 1,3-dipolar cycloaddition react with activated ligands. Steric hindrance, lower amino group reactant accessibility or surface interactions could be the reason of this lower reactivity.

3.3.3 T_1 experiments: finding the suitable experimental parameters

In order to better understand the dipolar interactions between NV centers and paramagnetic species by means of T_1 measurements, spin dynamics and charge dynamics must be considered. For this purpose, the best experimental parameters need to be found.

Taking advantage of the above-mentioned experimental setup, studies of annealed 50nm bare NDs photoluminescence emission trend as function of laser power were conducted (Figure 40).

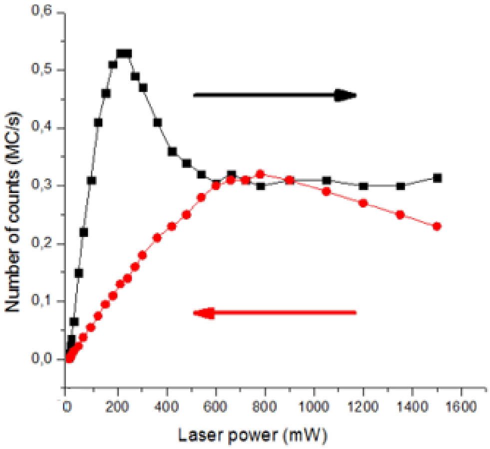

Figure 40. Photoluminescence (PL) emission trend of annealed 50nm bare NDs, as a function of laser power irradiation. PL is recorded irradiating the sample with increasing (black line) and decreasing laser powers (red line).

From the photoluminescence trend, interesting phenomena were observed:

- By irradiating the material with very high powers (red line), a reduction in the fluorescence intensity is observed since from the beginning of the experiment. This is probably due to laser triggers charging phenomena that convert the fluorescent NV^- centers into less fluorescent NV^0.
- By reducing laser power, PL remains low, since the charging phenomena have already balanced.
- On the other hand, when irradiating with low powers, spin dynamics are prevalent, and PL increases as laser power increases, but beyond a certain power level, charge phenomena begin to prevail again, leading to a reduction in photoluminescence.

From these results, we wondered whether the graphitic surface could play some role in making one dynamic phenomenon predominant over the other.
Same experiments were performed on NDs (11)-50-a (system exposing only the aminic linker), on paramagnetic (14)-50-a and on chemically oxidized (HNO_3) NDs-COOH (16) which shows a very low amount of graphitic surface (Figure 41).

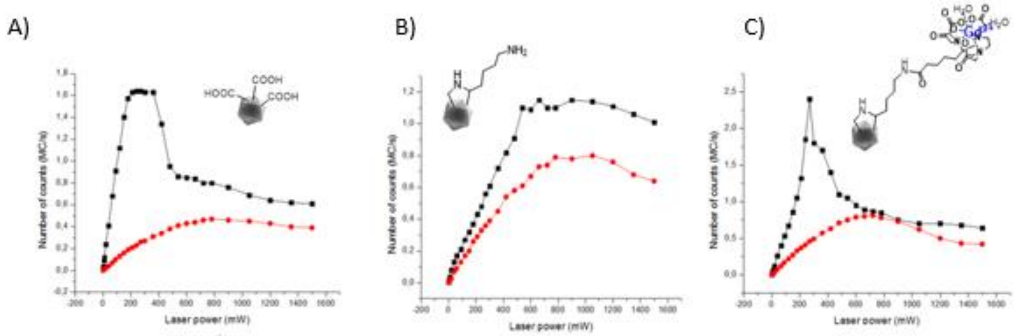

Figure 41. Photoluminescence (PL) emission trend of carboxilated NDs NDs-COOH (16) (A), NDs-linker (11)-50-a (B) and NDs-Gd (14)-50-a (C) as a function of laser power irradiation. PL is recorded irradiating the sample with increasing (black lines) and decreasing laser powers (red lines).

The data interpretation is complex. Many other equilibrium phenomena concur to modify the spin and charge dynamics. However, without going into details, from the PL trends it is possible to highlight that both the typology of the surface and the typology of derivatization, when this is paramagnetic, modify the behaviour of the internal NV centers, altering these complex phenomena^{73}. This deserves further investigations.

3.3.4 ODMR experiments

In order to confirm the role of graphitic surface in tuning charge dynamics, ODMR experiments have been performed as well. These experiments allow to study the NV center hyperfine structure.

ODMR spectrum of bare annealed 50nm NDs is reported in Figure 42.

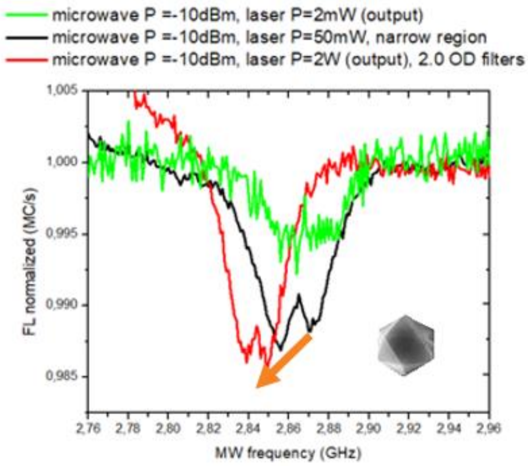

Figure 42. ODMR experiment of annealed 50 nm bare nanodiamonds, showing the shift of spin polarization frequency to lower values (orange arrow) when the sample is irradiated with increasing laser powers (from green to black to red).

The increasing laser power led to a shift of spin polarization frequency to lower values (orange arrow in fig. 42), from 2.87 GHz to 2.84 GHz. These results indicate that this experimental condition alter NV centers, accordingly to data obtained on bulk diamonds[129].

ODMR data acquired on NDs (11)-50-a, on paramagnetic NDs (14)-50-a and on chemically oxidized NDs-COOH (16), are shown in Figure 43.

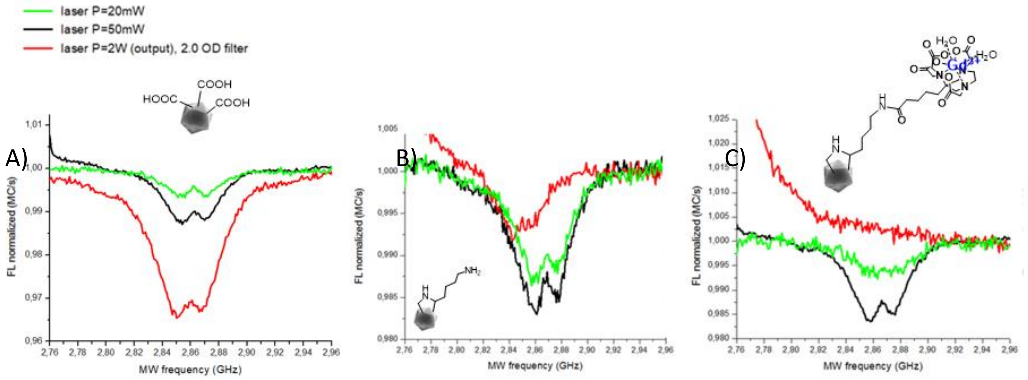

Figure 43. ODMR profile of carboxilated NDs NDs-COOH (16) (A), NDs-linker (11)-50-a (B) and NDs-Gd (14)-50-a (C). Samples are irradiated with increasing laser powers (from green to black to red).

Chemically oxidized NDs-COOH have a very low amount of graphitic surface. When they are irradiated with increasing laser powers, the resonant frequency does not vary (Fig 43A). Probably carboxylic groups present on their surface reduce, in some way, the charge dynamics phenomena, which would contribute to alter NV^- fluorescence profile.

NDs grafted with amino-pyrrolidine moiety maintain a significative amount of graphitic surface. Their irradiation with increasing laser power, from 20 to 50 mW, leads to an increase in ODMR contrast (Figure 43B). 2W laser power (red line) could alter NV^-, as can be observed by the shift of the resonant frequency to lower values (from 2.87 to 2.84 GHz) and by the decrease in fluorescence in the left part of the spectrum. All these aspects probably are triggered by charging phenomena, favoured in these experimental conditions.

Paramagnetic NDs-Gd have the same graphitic surface than their precursors (NDs grafted with amino-pyrrolidine moiety). ODMR data obtained on these nanosystems are like the previous ones (Figure 43C). In this case, the power increasing to 2W shows a very marked exponential decay (red line), which does not allow to appreciate spin levels resonant frequency. This could be explained by assuming the alteration of the NV^- centers and a role, which is not clear yet, of the paramagnetic species in modifying the balance between the two dynamic processes.

ODMR experiments confirm an interesting role of the surface and its derivatization on NV centers paramagnetic behaviour, by tuning charge and spin dynamics.

Despite high laser are necessary for studying the paramagnetic behaviour of the NV centers with high sensitivity, however, they trigger such phenomena, making the results difficult to interpret. Both graphite and paramagnetic species on NDs surface concur to alter these measurements by means of thermal, charge and spin polarization effects.

GRAPHITIC SURFACE FUNCTIONALIZATION: NDs AS ACTIVE DRUG FRAGMENTS

3.4 NDs conjugation with porphyrins

In addition to the ability to alter the NV magnetic behaviour, graphitic surface layer can be exploited as radical/charge stabilizer in photo/sono-induced excited states, by its extensively delocalized pi-electrons. NDs could thus be exploited to modulate the properties of sensitizers commonly used in sono- and photo-dynamic therapy (e.g. porphyrins)[130,131]. The NDs could act as active drug fragments in NDs-sensitizer nanosystems. Taking advantage of surface amino groups introduced by the above mentioned 1,3-dipolar cycloaddition, a carboxy porphyrin was conjugated to NDs (see Scheme 6), leading to ND-porphyrin nanosystems (17).

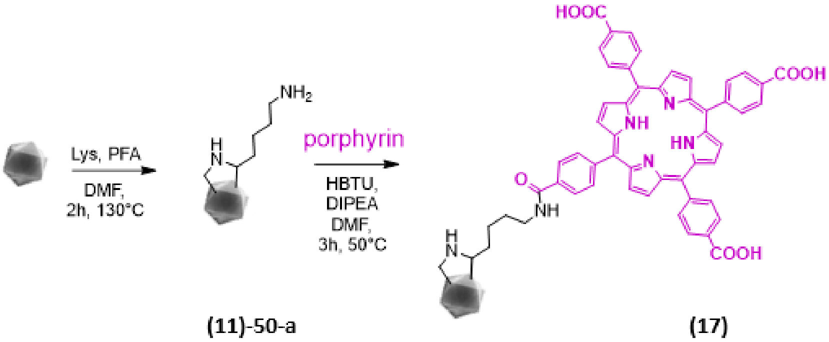

(11)-50-a **(17)**

Scheme 6. Synthesis of ND-porphyrin nanosystem (17), starting from aminated NDs (11)-50-a.

The thermogravimetric profiles of aminated NDs (11)-50-a and ND-porphyrin nanosystems (17) prove the success of the synthetic procedure. ND surface loading repeats the behaviour already observed with the ligands conjugation: the amino groups present on diamond surface react only partially with the adding moiety (about 25%, Figure 44). The porphyrin steric hindrance could have a detrimental effect on the conjugation yield.

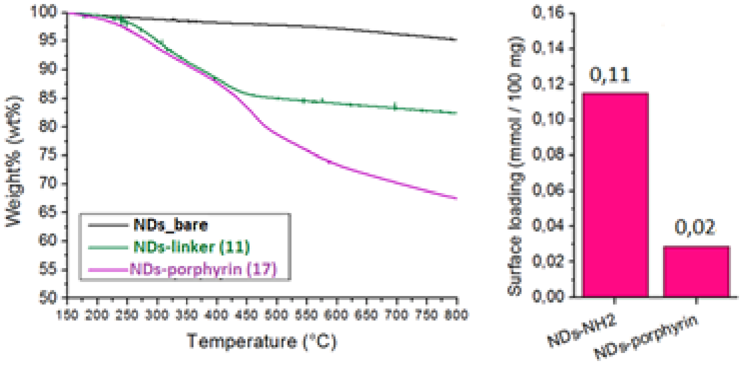

Figure 44. A) Thermogravimetric profile of bare NDS (black line), aminated NDs (17)-50-a (green line) and NDs-porphyrin nanosystems (17) (purple line). B) Bars expressing surface loadings (mmol of adduct / 100 mg of bare NDs) of pyrrolidine adducts (17)-50-a and porphyrins (17) on NDs. Errors are reported in Figure E6.

FT-IR spectroscopy further demonstrate the success of porphyrin conjugation of aminated nanodiamonds as depicted in Figure 45.

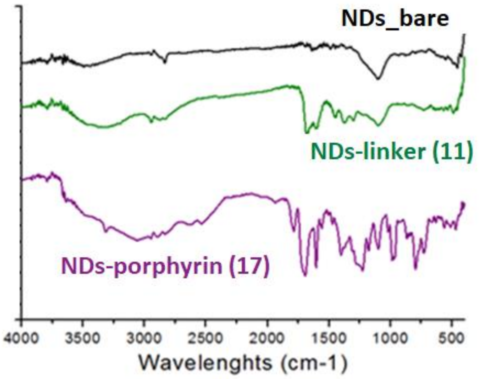

Figure 45. FT-IR spectra of bare annealed NDs (black), NDs aminated with pyrrolidine cycloaddition adduct (green) and the final system ND-porphyrin (17) (purple).

The IR spectrum of the untreated NDs is characterized by the presence of a broad absorption in the 3650–3000 cm^{-1} spectral region, associated to the *v*(OH) stretching modes of hydrogen bonded water molecules[38]. After the introduction of the linker, new bands appear at 1520-1700 cm^{-1}, related to NH bending.

Looking at the ND-porphyrin IR spectrum, important absorption peaks can be observed: the narrow band at 3321 cm^{-1} due to the v(NH) stretching and the vibrations involving C=C and C=N stretching of the porphyrin macrocycle in the 1650-1400 cm^{-1} region[132].

Moreover, the presence of a peak at 1682 cm^{-1}, typical of carbonyl stretching signal, is consistent with the formation of amide bond between surface amino groups and porphyrin carboxylic groups[39].

The thermal transition temperature in TGA profile and IR data ensure the occurrence of the amidic bond.

.

GRAPHITIC SURFACE FUNCTIONALIZATION: TUNING STUDIES

3.5 Tuning graphitic surface functionalization with azomethine ylides

Given the importance of preliminary NDs surface decoration for grafting active molecules in a tunable manner, studies of grafting tunability of heteroatoms on NDs surface have been conducted, taking advantage of 1,3-dipolar cycloaddition of amino acid-generated azomethine ylides. Lysine has been chosen as model aminoacid, reaction conditions are varied, and surface loadings quantified. Multiple functional moieties have been grafted and tuned by means of azomethine ylides generated by other amminoacids (serine, cysteine and tyrosine) as well. Reactions with common electrophiles have been subsequently studied.

3.5.1 Dependence of lysine-derived azomethine ylides cycloaddition on solvent and reaction time

Firstly, the efficacy of 1,3-dipolar cycloaddition reaction of azomethine ylides generated from lysine and paraformaldehyde (PFA) on NDs has been evaluated as function of the employed solvent (see Scheme 7).

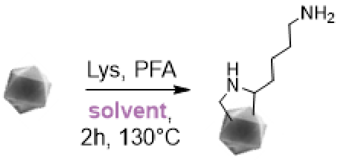

(11)-s1, (11)-s2, (11)-s3, (11)-s4

Solvent	Substance
DMF	**s1**
Toluene	**s2**
DMSO	**s3**
DMF+H_2O	**s4**

Scheme 7. Lysine and paraformaldehyde generated azomethine ylides cycloaddition on NDs, varying kind of solvent.

Keeping constant reagents concentrations, time and temperature, the reaction has been performed in dimethylformamide (DMF), toluene, dimethylsulfoxide (DMSO) and in water/DMF mixture (H_2O/PFA molar ratio of 5). Through the estimation of surface loading by TGA (Figure 46), it has been identified dimethylformamide as the most effective solvent. However, a quite large amount of water mixed to DMF drastically lowers the cycloaddition yield.

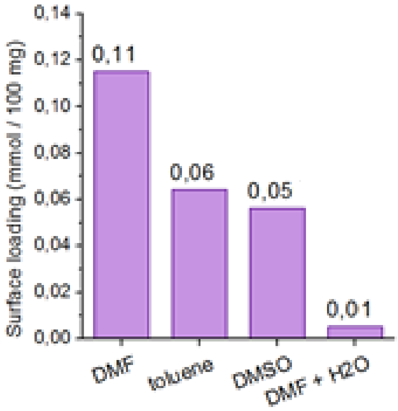

Figure 46. Surface loadings estimations of NDs reacted with lysine and paraformaldehyde, in different solvents. Errors are reported in Figure E8.

Toluene and DMSO led to a less satisfactory surface loading, probably because of the lower solubility of the employed reagents. Moreover, it cannot be excluded the solvation role of the solvent in the formation and stabilization of azomethine ylide.

The dependence of surface loadings as a function of reaction time is then studied using DMF as solvent and maintaining constant reagents concentrations (lysine and PFA) and temperature (see Scheme 8).

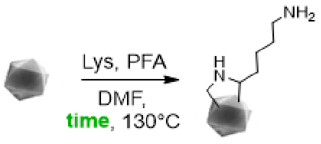

(11)-t1, (11)-t2,
(11)-t3, (11)-t4

Time (h)	Substance
2	**t1**
4	**t2**
8	**t3**
16	**t4**

Scheme 8. Lysine and paraformaldehyde generated azomethine ylides cycloaddition on NDs, varying reaction time.

In Figure 47, surface loadings estimated from TGAs are reported.

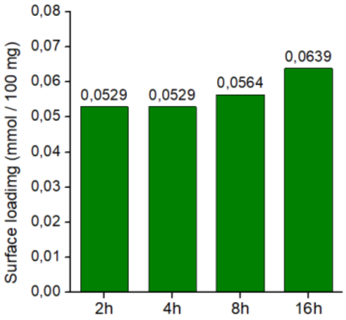

Figure 47. Surface loadings estimations of NDs reacted with lysine and paraformaldehyde, at different times. Errors are reported in Figure E10.

The results clearly show that prolonging reaction time does not significantly increase the amount of grafted material can be obtained. The reaction can be carried out at 130°C for just 2 hours.

3.5.2 Dependence of lysine-derived azomethine ylides cycloaddition on reagents concentration

Beyond solvent and time optimization, the study was focused on the role of reagent concentration. To this purpose, 50 nm nanodiamonds have been subjected to post-synthesis annealing process, since the reaction involves the *sp*^{2} graphitic surface[133].

Lysine/PFA molar ratio is kept constant (1.2) and solvent volume as well (2 mL DMF / 10 mg NDs). Reagents concentration has been varied, starting from condition Q (0.25 mmol PFA/15mg NDs) to Q/2, Q/4, Qx2 and Qx4, leading to NDs (11) -(Q/2-Qx4). The solvent volume was not changed to make sure that the heat transferred through the solvent to the reaction components always occurs in the same way, depending only on its dielectric constant. Trends of derivatization degree as function of reagent concentration and fitting plot are reported in Figure 48.

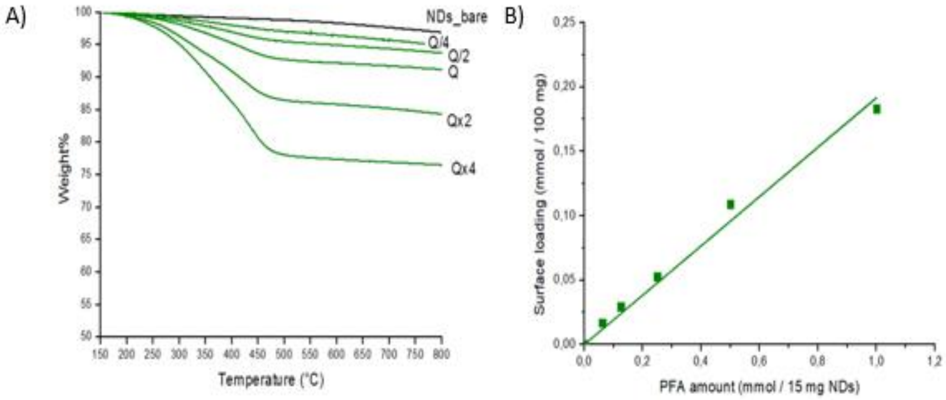

Figure 48. A) Thermogravimetric profiles of NDs reacted with different amounts of lysine and paraformaldehyde (NDs-Lys (Q/4, Q/2, Q, Qx2, Qx4)). B) Fitting plot of surface loading as function of PFA amount (r^2= 0.9967).

The derivatization amount is directly proportional to reagent concentration. In fact, apart from the extension of the graphitic surface (which act as dipolarophile), the effectiveness of a cycloaddition reaction depends on the amount of formed dipole, which in turn depends on reagents quantity. Moreover, since the graphitic surface is limited in its extension, the degree of surface derivatization could reach a plateau with a further increase in reactants amount. By means of this strategy, surface grafting proved to be predictable.

3.5.3 NDs functionalization with other aminoacid-derived azomethine ylides

In order to decorate NDs surface with different functional groups, cycloaddition reactions with cysteine, serine and tyrosine were performed (see Scheme 9).

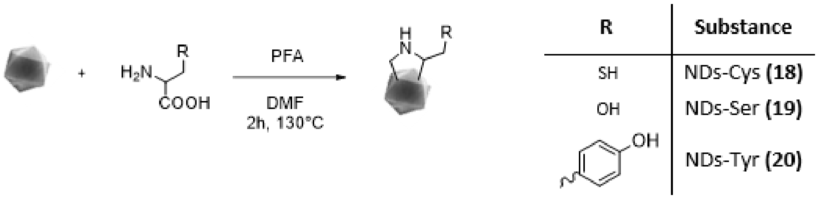

R	Substance
SH	NDs-Cys **(18)**
OH	NDs-Ser **(19)**
OH	NDs-Tyr **(20)**

Scheme 9. NDs reactions with paraformaldehyde and different amminoacids, leading to ND-Cys (18), NDs-Ser (19) and NDs-Tyr (20).

Also in these cases, reagents concentration were varied, and surface loadings have been determined via TGA (Figure 49).

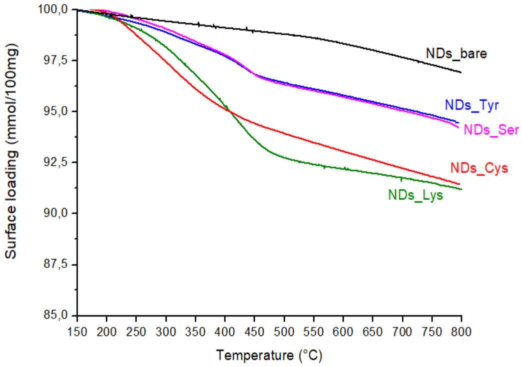

Figure 49. Thermogravimetric profiles of NDs reacted with paraformaldehyde and cysteine (NDs-Cys (18), red), serine (NDs-Ser (19), magenta) or tyrosine (NDs-Tyr (20), blue). The case of lysine (11)-Q is reported as comparison (green).

Correlations between derivatization degrees and reactants concentration were then verified as well (see Figure 50).

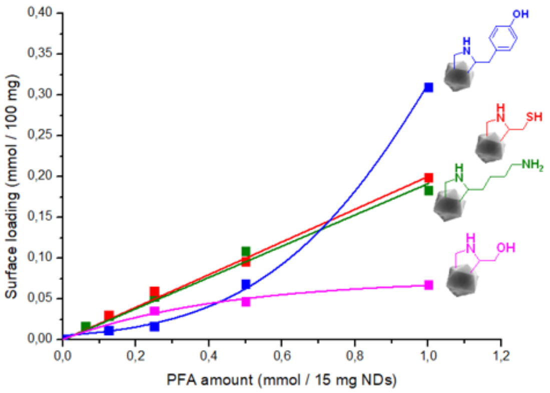

Figure 50. Trends of surface loadings estimation relative to NDs reacted with paraformaldehyde and cysteine (NDs-Cys (18), red), serine (NDs-Ser (19), magenta) or tyrosine (NDs-Tyr (20), blue). The case of lysine (11)-Q is reported as comparison (green).

The trend of surface loading estimation of NDs reacted with cysteine and paraformaldehyde is very similar to the case of lysine. By contrast, the grafting amount by cycloaddition reaction involving serine shows a polynomial trend. In this case, a plateau is almost reached at relatively low reagents concentrations, with respect to reactions with other amino acids (in the case of lysine and cysteine we are observing only the initial part of the polynomial curve, which is approximable as linear). The grafting efficacy in the case of tyrosine is exponential. The explanation could lie in the hydroxyphenyl residues on the surface pyrrolidine rings, which can trigger polymerization phenomena with paraformaldehyde and tyrosine themselves, building up phenol-formaldehyde-like adducts[134].

In general, the success of a 1,3-dipolar cycloaddition reaction depends on the easiness of dipole formation, as well as on its stability. In the case of azomethine ylides, the aminoacid side chain could play an important role both in dipole formation and stabilization. Thus, the amount of the cycloaddition adducts on nanodiamonds graphitic surface is influenced by the involved aminoacid.

3.5.4 NDs conjugation with electrophiles

To evaluate the applicative potential of the previously obtained NDs, the possibility of covalently link electrophiles was verified. In particular, NDs-Lys (11)-(Q) and NDs-Cys (18)-Q/4 are conjugated with 6-N-Fmoc protected hexanoic acid chloride (f) and *N*-ethyl maleimide respectively, leading to (21) and (22) (Figure 51). The obtained nanosystems have been analysed by thermogravimetry and satisfactory conjugation yields were estimated.

Differently from that observed in the case of porphyrin conjugation, the linkage of 6-N-Fmoc protected hexanoic acid chloride occurs with higher yield (52% respect to 25%), supporting the hypothesis of a certain role of steric hindrance of electrophile in conjugation reaction. Little bit lower yield has been observed in the case of maleimide reaction, probably because of the different reaction mechanism.

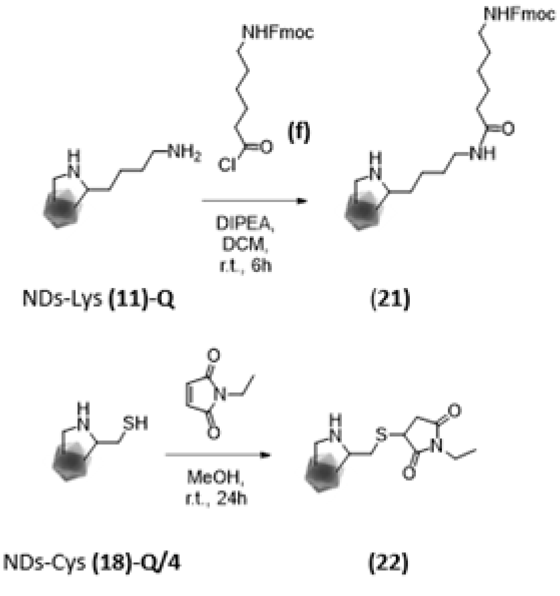

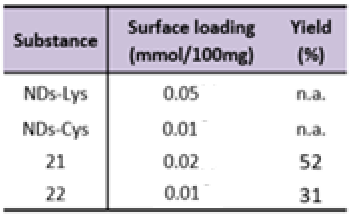

Substance	Surface loading (mmol/100mg)	Yield (%)
NDs-Lys	0.05	n.a.
NDs-Cys	0.01	n.a.
21	0.02	52
22	0.01	31

Figure 51. Conjugation of some electrophiles on surface grafted heteroatoms. Amino groups on NDs-Lys (11) -Q are conjugated with 6-N-Fmoc protected hexanoic acid chloride, leading to (21), thiol groups on NDs-Cys (18)-Q/4 are reacted with N-ethyl maleimide, leading to (22). Errors are reported in Figure E18.

3.5.5 Irreversibility of lysine-derived azomethine ylides cycloaddition

The 1,3-dipolar cycloaddition of azomethine ylides generated by aminoacids is a very versatile reaction, since, by varying aminoacid and aldehyde, it is possible to decorate nanodiamonds surface with different functional groups. With the aim of introducing more than one kind of functional group on the same nanodiamond taking advantage of this strategy, nanodiamonds could be subjected to multiple reaction cycles, changing reagents between one cycle and another. To study this possibility, it is necessary to be sure that the retro-cycloaddition reaction of pyrrolidine adducts on nanodiamonds does not occur. It is known, in fact, that retro-cycloaddition reaction of pyrrolidinofullerenes has been observed in harsh reaction conditions (1,2-dichlorobenzene, 180°C, 18h, with $Cu(OTf)_2$)[135].
To this purpose, NDs-Lys (11)-Qx4 was reacted in DMF at 130°C for 2h in order to exclude the possibility of such retro-cycloaddition in the tested milder conditions (Scheme 10).

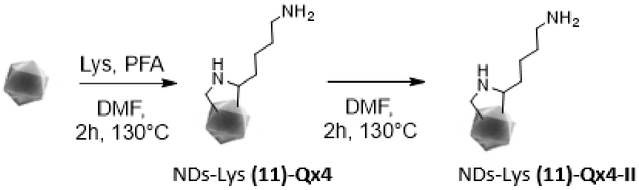

Scheme 10. Aminated NDs-Lys (11)-Qx4 are reacted in DMF without reagents, in the same reaction conditions, leading to NDs-Lys (11)-Qx4-II.

The close similarity of thermogravimetric profiles of NDs-Lys (11)-Qx4 and NDs-Lys (11)-Qx4-II (Figure 52) proved that retro-cycloaddition doesn't take place in the tested reaction conditions.

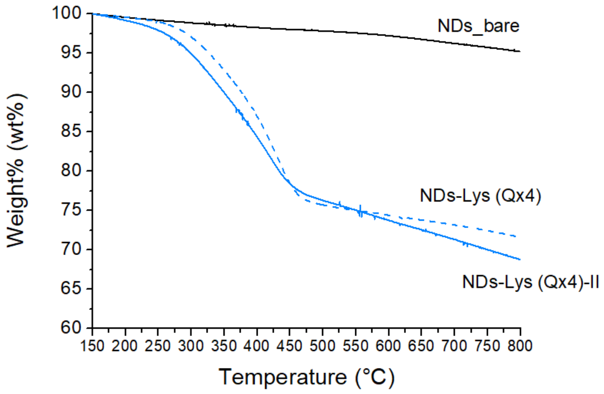

Figure 52. Thermogravigrams of NDs-Lys (11)-Qx4 and NDs-Lys (11)-Qx4-II.

3.5.6 NDs functionalization with different heteroatoms

On the base of these results, we wondered if it was possible to graft different heteroatoms on the same ND, by means of two (or more) consecutive reaction cycles. Nitrogen and sulphur have been chosen. First cycloaddition reaction of azomethine ylides generated from PFA and lysine has been performed, obtaining the above mentioned aminated NDs-Lys (11)-Q, which has been subjected to a second cycle with cysteine and PFA (in condition Q) to graft thiol groups, obtaining (23) (see Scheme 11).

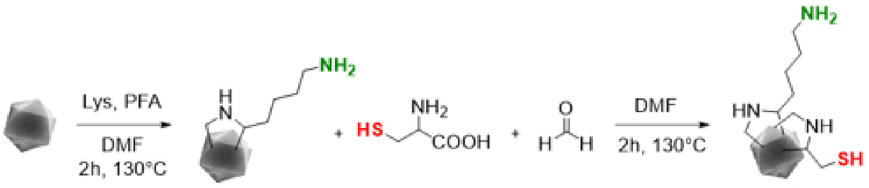

NDs-Lys **(11)-Q**

(23)

Scheme 11. Grafting of amino and thiol groups on the same ND, performing two reaction cycle with PFA and aminoacid: a first reaction cycle with paraformaldehyde and lysine, leading to NDs-Lys (11)-Q; a second cycle with paraformaldehyde and cysteine lead to (23).

The hybrid material (23) has been analysed by thermogravimetry (Figure 53A) and surface loading has been estimated.

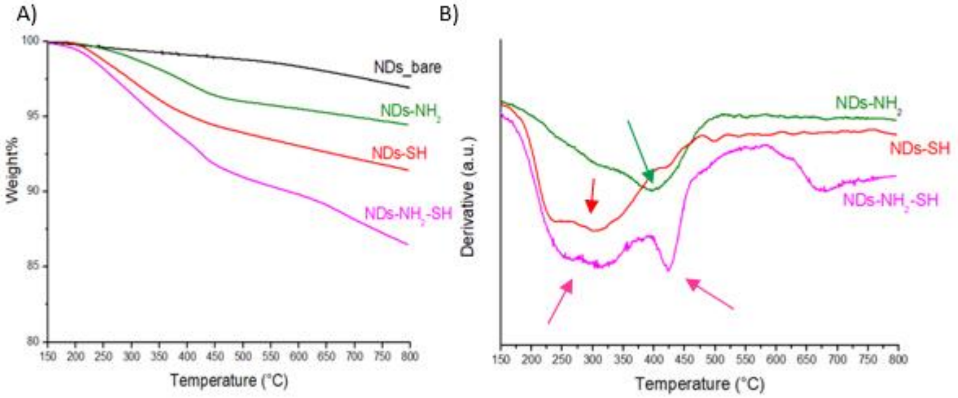

Figure 53. Thermogravigrams (A) and relative derivative profiles (B) of the hybrid NDs-NH$_2$-SH nanosystem (compound (23), magenta), NDs-SH (compound NDs-Cys (18)-Q, red) and NDs-NH$_2$ (compound NDs-Lys (11)-(Q/2), green), showing typical transition temperature (arrows).

Thermogravimetric analysis clearly shows the occurred double grafting, with 0.02 mmol/100mg of amino groups and 0.06 mmol/100mg of thiols (errors are reported in Figure E19). Moreover, it is important to underline that the derivative of the hybrid material shows the same thermal transitions of the two singularly grafted materials (arrows in Figure 53B), further demonstrating the success of this two steps process. By using this strategy is therefore possible to introduce N and S atoms on the same ND with two different reaction cycles.

CARBOXYLIC SURFACE FUNCTIONALIZATION: NDs AS FLUORESCENT TARGETED NANOSYSTEMS

The partial removal of graphitic surface due to oxidative treatments can increase NDs fluorescence emission intensity, making them further suitable for fluorescence imaging applications[28]. Active molecules can be grafted on NDs taking advantage of surface carboxylic groups. For example, specific antibody could be conjugated to their surface in order to target certain cellular receptor, thus extending NDs application in sensing field.

3.6 The ND-Cetuximab nanosystem

By means of a suitable organic linker grafted on surface carboxylic groups the monoclonal antibody Cetuximab has been covalently conjugated to NDs, making the nanosystem specific towards membrane epidermal growth factor receptor (EGFR). Then, a particular overexpressing EGFR cell line has been incubated with the so obtained NDs and confocal microscopy fluorescence analysis has been performed in order to visualize NDs-cell specific interaction.

3.6.1 Making the ND-Ctx nanosystem

The NDs-Cetuximab nanosystem synthesis strategy is shown in Scheme 12.
50nm annealed NDs were reacted with sulfonitric mixture, with the purpose of partially removing the graphitic surface and to increase surface carboxylic groups amount.
In order to guarantee the efficient Cetuximab covalent grafting on NDs and the proper Cetuximab-EGFR interaction, an appropriate distance between the antibody and NDs surface is required. For this reason, the aminic linker (i) is synthesized and grafted on NDs-COCl which have been previously obtained by refluxing carboxylic nanodiamonds in thionyl chloride. Cetuximab was then

modified with γ-thiobutyrolactone for promoting its conjugation with the linker grafted on ND. Targeted nanosystem (26) has been obtained simply mixing the two entities (25) and (I) in water. The bis-alkyloxy ethyl portion of the linker (indicated as cylinder in scheme 12) has been selected because probably it could promote the interaction with solvent water molecules, thus avoiding its folding on diamond surface and making easier the interaction between antibody and receptor. The maleimide/thiol conjugation strategy has been chosen thinking to future possible applications of this targeted nanodiamonds as targeted drug delivery system, in which the antibody conjugation must occur as last synthetic step, after drug linkage.

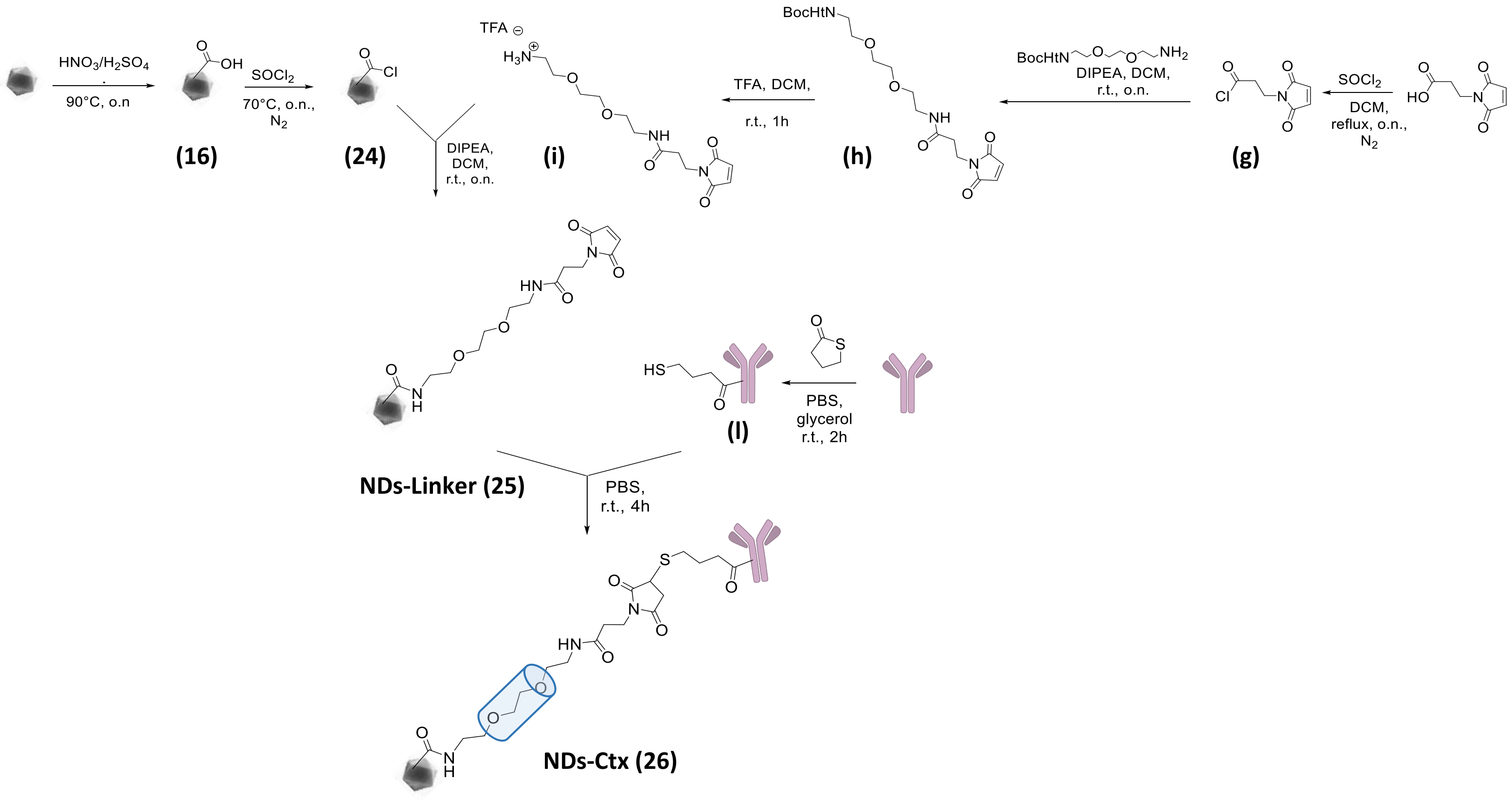

Scheme 12. Synthesis of NDs-Cetuximab nanosystems (26). The conjugation of NDs-COCl (24) with the organic linker (i) lead to NDs-linker (25), which in turn is grafted with the thiol-modified Cetuximab (l), making the final nanosystem NDs-Cetuximab (26). Water surrounding the bis-alkyloxyethyl portion (cylinder) gives the linker the required rigidity.

The surface loading of Cetuximab was estimated by thermogravimetric analysis and it results in 0.11 µmol / 100 mg NDs (errors are reported in Figure E22). It was intentionally kept low with the purpose of limiting the cytotoxic effect of antibody during the incubation period[136]. Moreover, a large amount of antibody on NDs surface is not necessary to assure a good nanosystem-cell interaction.

3.6.2 *In vitro* test

HT29 colon-rectal cancer cells line, overexpressing EGFR, are incubated with NDs-Cetuximab systems (26), with a proper concentration (see Experimental Section) and analysed by fluorescence microscopy (Figure 54).

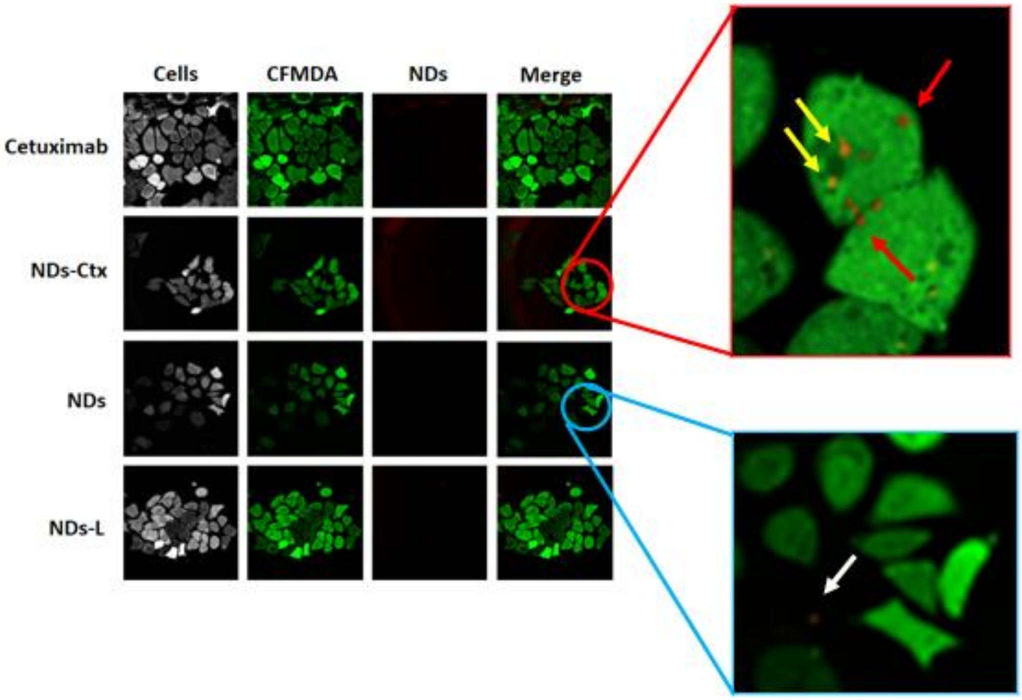

Figure 54. Fluorescence confocal microscopy imaging of HT29 cells incubated with Cetuximab, NDs-Ctx, NDs and NDs-L. Magnification of cells incubated with NDs-Ctx shows that nanodiamonds are in part on cell surface (red arrows) and in part internalized (yellow arrows). Magnification of cells incubated with NDs shows NDs far from cell membrane (white arrow). There is no cell interaction between Cetuximab alone or NDs and cells.

HT29 cells are stained with the common CFMDA (5-chloromethylfluorescein diacetate), which emits at 490nm (green light) and incubated with Cetuximab, NDs-Ctx, NDs or NDs-L. NDs are analysed after 24, 48 and 72 hours. The results shown in figure 54 are referred to 72 hours (max emission at 637 nm, red light).
Fluorescence confocal microscopy experiments show that only the NDs-Ctx nanosystem interact strongly with cell membranes. More interestingly, some NDs-Ctx nanosystems are internalized within cells. This is proved by some spots of yellow fluorescence, arising from red (NDs-Ctx) and green fluorescence (cells) from the same focal plane.

Summing up:

- NDs specifically interact with a target when they are grafted with a specific antibody.
- Targeted nanodiamonds can be internalized; this would allow to specifically deliver drugs loaded on NDs surface that may act on intracellular targets, reducing potential side effects.

3.7 Tuning NDs surface functionalization: graphitic vs carboxylic approach

The success in exploiting both graphitic and carboxylic NDs surface for grafting molecules of interest, suggests studying the functionalization tunability also on carboxylic surface. NDs subjected to different post-synthesis oxidative treatments, aimed at modifying reactive surface area, have been considered to this purpose. The more aggressive oxidative treatment, the greater the extension of the carboxylic surface, at the expense of the graphitic one. To evaluate the “reactivity” of the two different “surface components” the 1,3-dipolar cycloaddition via azomethine ylide and condensation reactions have been selected for the graphitic and carboxylic component respectively. Since these kinds of reactions involve two different kind of surfaces, they can be considered as complementary (see Figure 55).

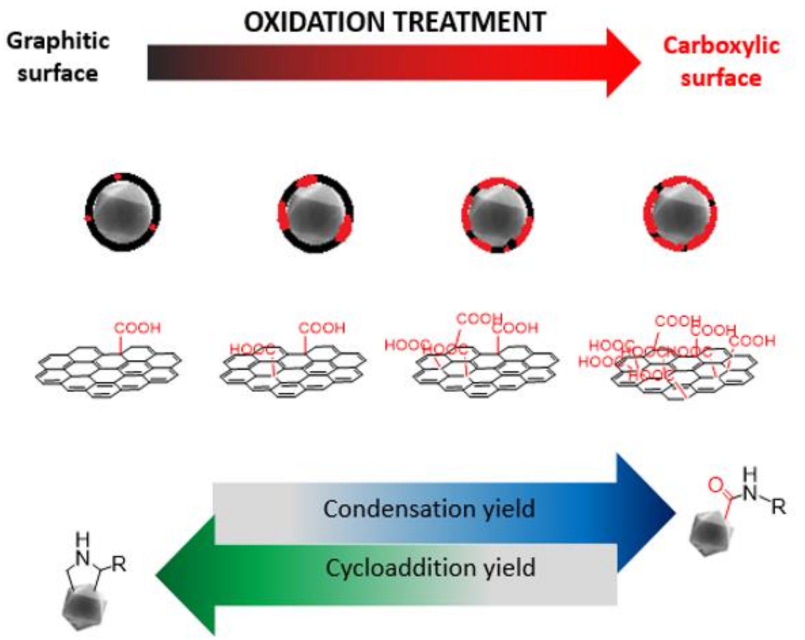

Figure 55. Increasingly aggressive oxidation treatments lead to extension of carboxylic surface, at the expense of the graphitic one. Condensations and cycloaddition reactions yields are complementary, because the involved surface components are complementary as well.

3.7.1 NDs oxidative post-synthesis treatments

Firstly, raw 50nm NDs were processed with a high temperature thermal annealing in N_2 flux at 800 °C for 2 h. Different oxidation processes on the annealed NDs were then carried out at 400°C for 30 minutes and at 500 °C for 1 h, in air environment.

Stronger chemical oxidation was also carried out using sulfonitric mixture at 100°C overnight.

The oxidation processes determine the partial removal of surface graphitic layers, resulting in a potential increase in luminescence produced by the diamond core NV centers. The photoluminescence spectra of the oxidized samples (see Figure 56) shows an intense emission band between 580 nm and 780 nm, mostly ascribable to the NV-centers. As the oxidation level increase, the fluorescence yield is enhanced.

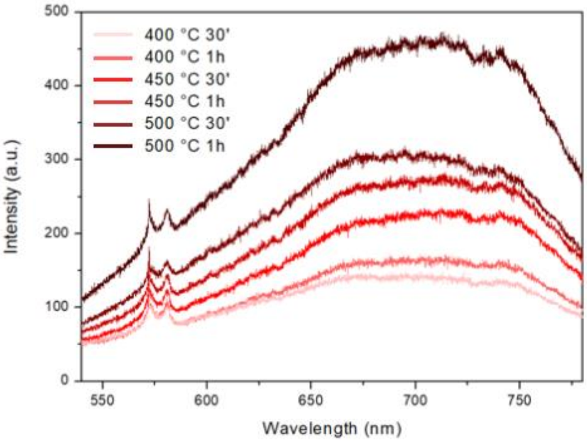

Figure 56. Photoluminescence spectra of NDs oxidized in oven with increasing aggressive treatments.

Oxidation processes cause changes in the surface chemical terminations, increasing the quantity of oxygen-related functional groups, such as carbonyls. This is proved by FT-IR spectroscopy analysis (see Figure 57).

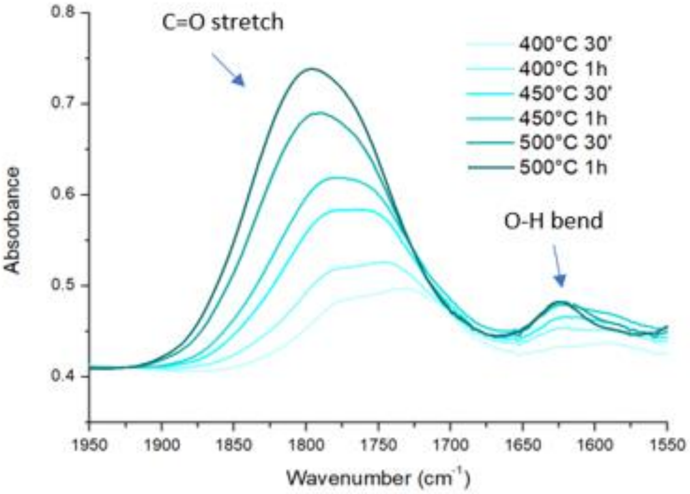

Figure 57. FT-IR spectra for annealing + oxidized samples with different temperature and process time parameters. Zoom over the C=O stretching region (1600 cm^{-1} - 1800 cm^{-1}).

3.7.2 Cycloaddition vs condensation reactions

Cycloaddition and condensation reactions (which can be considered complementary, due to the reactive surface involved) were carried out on four types of annealed NDs: subjected to no post-annealing treatment (A) and to increasingly aggressive oxidative treatments, from etching (B and C) to sulfonitric mixture (D), as depicted in Scheme 13.

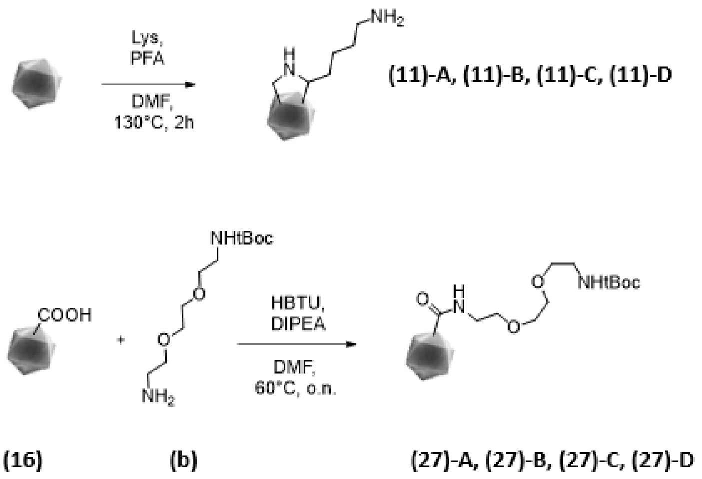

(11)-A, (11)-B, (11)-C, (11)-D

(16) **(b)** **(27)-A, (27)-B, (27)-C, (27)-D**

Scheme 13. Cycloaddition reaction of lysine-formaldehyde generated azomethine ylides on NDs involving graphitic component (top) and condensation reaction of monoboc-protected diamine (b) involving carboxylic surface groups (bottom).

The obtained nanodiamonds were then characterized by thermogravimetric analysis and the surface loading has been evaluated.

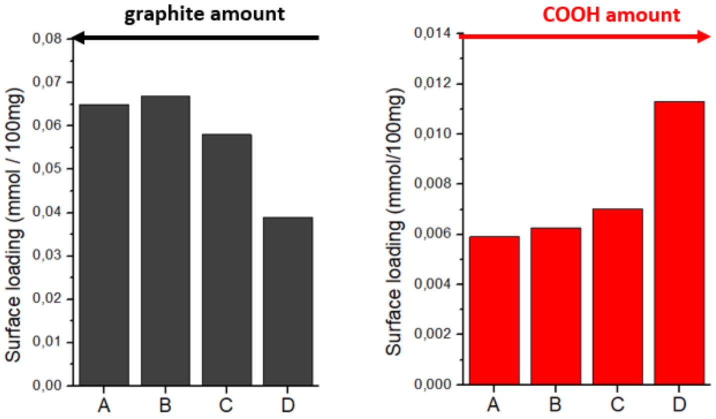

Figure 58. Surface loading estimation of NDs subjected to different post-synthesis oxidative treatments, involving azomethine ylides cycloaddition on graphitic surface (black bars) and condensation reactions involving carboxylic surface (red bars). The above arrow indicates the increasing in reactive surface area. Errors are reported in Figure E24 and E25.

Figure 58 shows that cycloaddition surface loading reaches a maximum of 0.065 mmol/100mg, while with the condensation the highest yield is 0.011 mmol/100mg. Moreover, cycloaddition surface loading is gradually lower as the aggressiveness of the oxidative treatment increases, because of removal of reactive graphitic surface. Conversely, the condensation reactions show an opposite trend, because oxidation procedures lead to an increase in reactive carboxylic groups.

It is important to underline that carboxylic surface conjugation is less reliable than the graphitic approach, but anyway tunable. This trend may be explained considering the different reactive surface area involved, infact graphitic surface is more extended than carboxylic one. Post-synthesis oxidative treatment can play an interesting role in tuning the surface grafting efficiency.

STRATEGIES FOR MAKING HIGHLY FLUORESCENT NDs

The production of nanodiamonds with a high NV centers density, which allows high detection sensitivity, is of great importance for sensing and biomedical applications. However, sensitivity is directly proportional to the square root of the number of NV centers[137], so it is mandatory to significantly increase density of NV centers in commercially available NDs.

In this work highly fluorescent NDs (FNDs) were obtained, according to two strategies: ion implantation of synthetic NDs and *ab-initio* synthesis of NDs from nitrogen-enriched materials.

3.8 Ionic implantation

Highly fluorescent NDs were obtained by ionic implantation following the procedure depicted in Figure 59.

50 nm HPHT monocrystalline synthetic NDs were subjected to annealing (800°C, 2 hours, in vacuum) then to etching (450°C, 45 min, in air) to remove impurities and the graphite component. A high energy (MeV) protons beams irradiation further generates the defects, which are converted in fluorescent NV centers approaching vacancies to defects by annealing treatment (800°C, 2 hours, in vacuum).

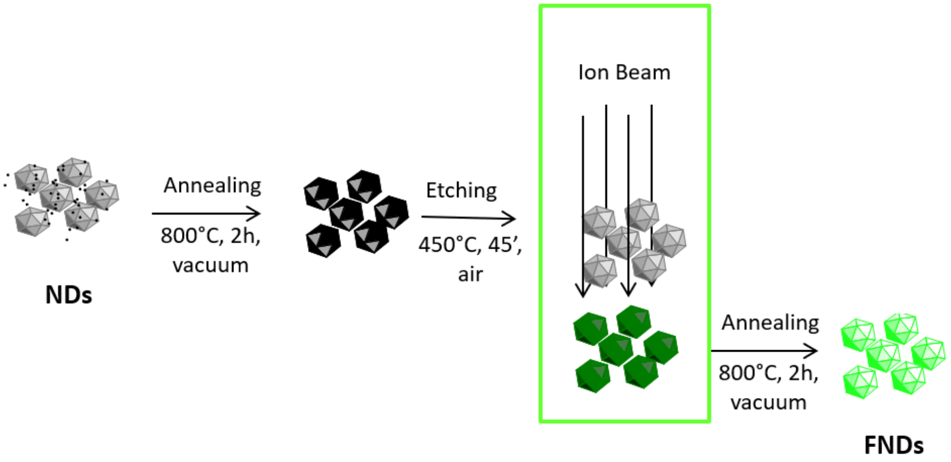

Figure 59. Synthesis of FNDs by ion implantation. Synthetic HPHT nanodiamonds (NDs) are subjected to annealing and etching treatments, then implantation with ion beam; final annealing procedure led to FNDs.

Fluorescence emission spectroscopy demonstrates the increased fluorescence properties of the FNDs obtained with the above-mentioned sequence. Accordingly to literature[4], typical NV^- emission at 660-700 nm is observed. Figure 60 shows the emission spectrum of implanted ND as well as spectra arising from nanodiamonds that have undergone only to intermediate steps.

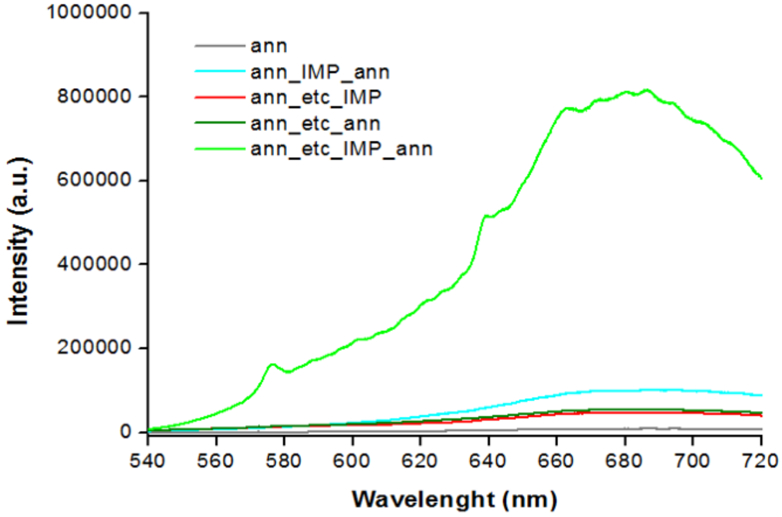

Figure 60. Photoluminescence spectra of NDs subjected to different post-synthesis treatments. Annealed NDs (grey line), annealed-etched-annealed NDs (dark green line), annealed-etched-implanted (red line), annealed-implanted-annealed (light blue) and annealed-etched-implanted-annealed (light green).

Of course, the fluorescence of implanted NDs is higher than non-implanted ones. However, the implantation *per se* is not enough to obtain highly fluorescent nanodiamonds. The annealing process after implantation is necessary to approach vacancies to nitrogen, thus generating the NV center. On the other hand, previous etching treatment removes the surface graphitic component that could shield fluorescence emission and could reduce the defects generation efficiency.

It is important to underline that implanted NDs can be functionalized exactly in the same way of non-implanted ones. Highly fluorescent ND-porphyrin nanosystem (17)-F has been prepared (see Scheme 14) according to the previously described strategies for NDs-(11) and NDs-porphyrin (17).

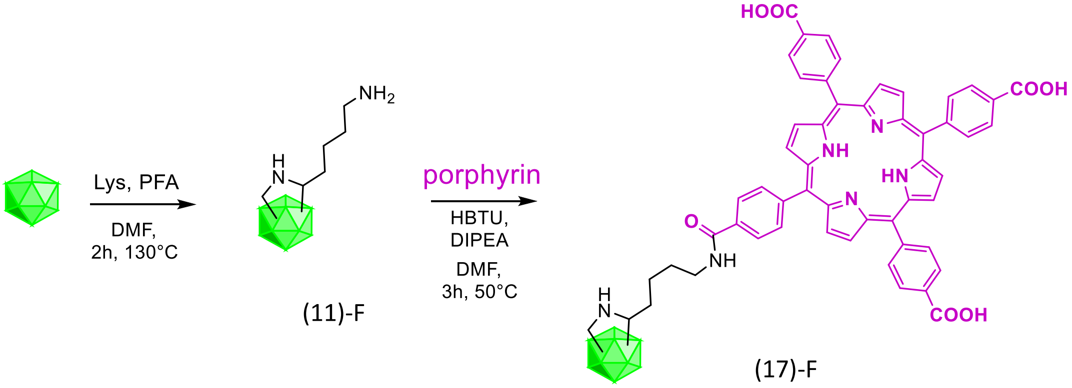

Scheme 14. Synthesis of FND-porphyrin nanosystems (17)-F, starting from aminated FND (11)-F.

3.9 Laser ablation of nitrogen-enriched graphite

Alternative method to ion implantation is represented by laser ablation, which was proven to successfully convert graphite into NDs with a limited size distribution (≤100 nm)[138]. We exploited the success of the 1,3-dipolar cycloaddition of azomethine ylides to enrich graphite with nitrogen[139]; then graphite was pressed and finally subjected to laser ablation in water in collaboration with Istituto Italiano di Tecnologia (Rovereto), according to Figure 61. The desired FNDs are obtained and characterized.

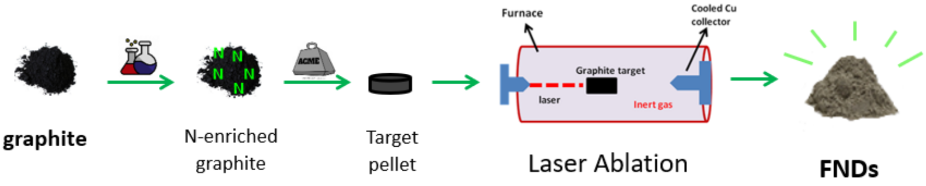

Figure 61. Synthetic sequence employed for converting graphite into fluorescent nanodiamonds (FNDs). Graphite is enriched with nitrogen by means of chemical reactions, then pressed into a pellet and finally ablated by laser, leading to FNDs.

3.9.1 Synthesis and characterization of N-enriched graphite

Two kind of graphite, with different nitrogen content, were prepared exploiting 1,3-dipolar cycloaddition. Reaction of paraformaldehyde and glycine and reaction of p-nitrobenzaldehyde and histidine on graphite were conducted. Considering the different steric hindrance of the involved reagents, higher cycloaddition yield is expected in the case of reaction with paraformaldehyde and glycine and lower yield when it comes the reaction with histidine and p-nitrobenzaldehyde. Thus, high-N (28) and low-N graphite (29) were obtained (Scheme 15).

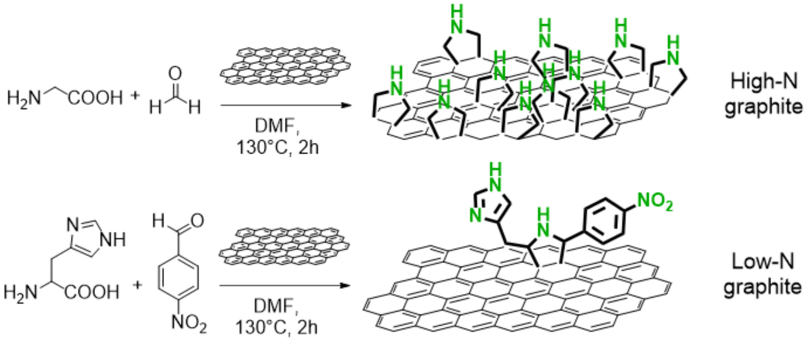

(28)

(29)

Scheme 15. Synthesis of High-N graphite and Low-N graphite by means of cycloaddition of different amminoacids (glycine or hystidine) and aldehydes (paraformaldehyde or p-nitrobenzaldehyde).

The N-doped graphite powders were characterized by thermogravimetric analysis to quantify nitrogen amount. A weight loss is observed at ~230 °C in both modified graphite. This is probably due to the degradation of the pyrrolidine ring (Figure 62).

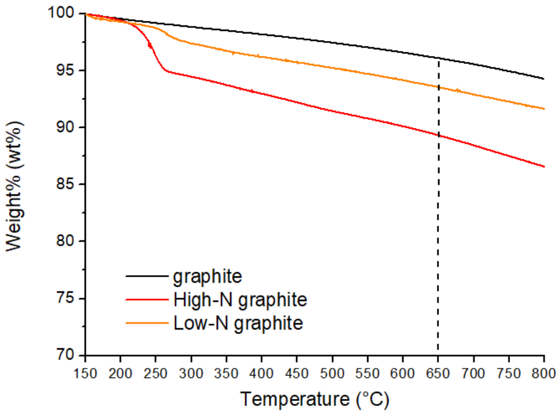

Figure 62. Thermogravigrams of graphite, high-nitrogen (28) and low-nitrogen (29) enriched graphite samples.

Table 2 shows nitrogen doping amount calculated from the thermogravimetric analysis.

Sample	Weight loss (%)	mg N / 1g graphite	N atoms / 1 g graphite (10^{20})
High N-graphite	7.1 ±0.5	23.3	9.9
Low N-graphite	2.5 ±0.5	5.8	2.5

Table 2. Nitrogen amount estimation in High-N graphite and Low-N graphite samples.

Although the pyrrolidine adduct obtained from histidine and p-nitrobenzaldehyde contains four nitrogen atoms, unlike the adduct obtained with glycine and paraformaldehyde which contains only one, the reaction with glycine and paraformaldehyde proved to be more efficient in making N-enriched graphite. An explanation may lie in the different ease of formation of azomethine ylide and further cycloaddition: the steric hindrance of histidine and p-nitrobenzaldehyde can impact negatively on the generation of the dipole and the subsequent cycloaddition reaction yield.

3.9.2 Synthesis and characterization of FNDs

N-doped powders were pressed by a tablet press, and the obtained pellets were used as targets for laser ablation in water. The obtained NDs are fully characterized in the morphological and optical properties, in particular with SEM, Raman, photoluminescence and ODMR spectroscopy to unequivocally prove the diamond-like features of the new nanomaterial and to confirm the NV origin of the NDs photoluminescence.

Morphological analysis of the ablated High-N material is reported in the inset of Figure 63, showing clustered nanoparticles having size <100 nm.

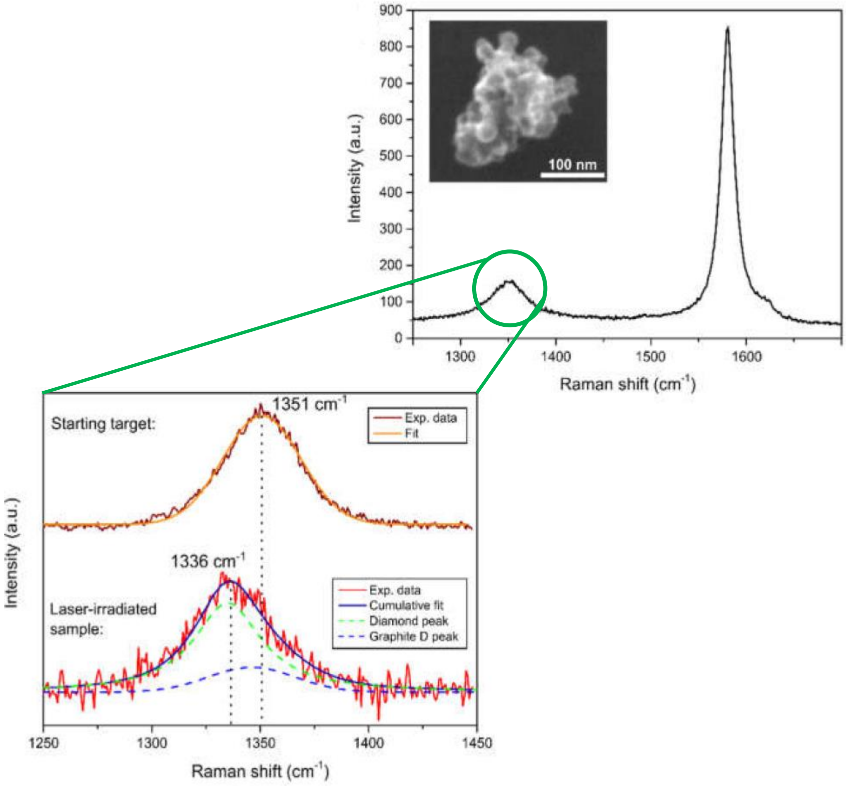

Figure 63. Raman spectrum of the ablated powder under 532 nm laser excitation, dominated by 1580 cm^{-1} G peak. Inset: morphological SEM analysis of the powder resulting from laser ablation. Bottom: magnification of 1336 cm^{-1} D peak.

Raman spectroscopy analysis shows that the spectrum is still dominated by the graphite G peak at ~1580 cm^{-1}. The 1336 cm^{-1} peak proved the presence of NDs in the ablated material. Indeed, it is a convolution between the diamond peak (green dashed line) at 1335 cm^{-1}, and the residual graphitic D peak (blue dashed line) at 1346 cm^{-1}, which is typical of the sp^2 carbon atoms surrounding the NDs cluster[42]. The diamond phase is also confirmed by comparison of the cumulative fit with the graphite D peak of the starting target (brown curve).

Starting N-doped graphite target (black curve), and the NDs (red curve) photoluminescence spectra were recorded to evaluate NDs fluorescence properties (Figure 64A).

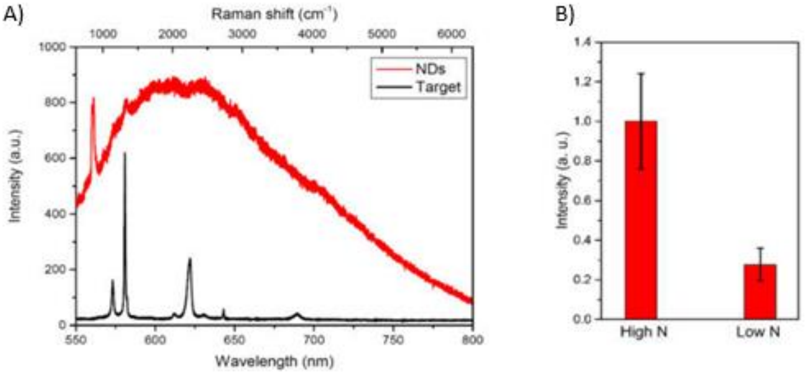

Figure 64. A) Photoluminescence and Raman spectra of FNDs (red line) and starting N-doped graphite target (black line). B) Photoluminescence intensity comparison between NDs laser-ablated from High-N and Low-N starting target.

In the case of NDs, a broad band is observed, consistent with the well-known NV$^-$ emission[140], shifted toward the low-wavelength region due to the presence of graphitic defects on the NDs surface[141]. This is a first proof that the nitrogen contained in the graphite is incorporated in the forming NDs upon laser irradiation. The starting target does not show any photoluminescence emission, as only the Raman peaks of graphite are detected.

Moreover, FNDs obtained from graphite with different amounts of nitrogen show different fluorescence intensity emission (Figure 64B). As expected, fluorescence emission intensity of FNDs synthesized from High-N graphite is higher than the one from Low-N graphite derived FNDs.

In Figure 65, an optical image of a micrometer-sized cluster and the corresponding photoluminescence image under 532 nm excitation are reported. It can be observed that only a portion of this cluster presents a red emission, because not all the ablated graphite is converted into NDs.

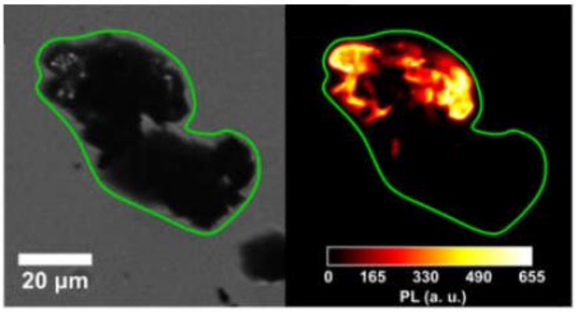

Figure 65. Wide field microscopy imaging analysis of FNDs clusters. Bright field (left) and fluorescent imaging (right).

ODMR spectroscopy, performed over the bright spots observed with photoluminescence imaging, finally proves the NV^- formation (Figure 33). The observed decrease in photoluminescence at around 2870 MHz typical of NV^-[137] indicates the NV^- origin of fluorescence (see Figure 66).

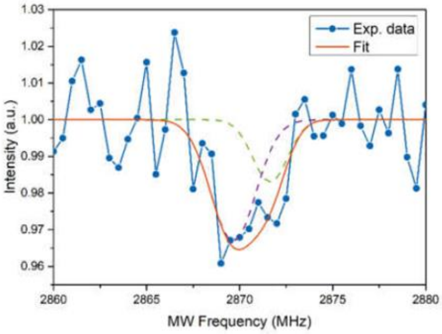

Figure 66. ODMR spectrum of FNDs synthesized from High-N graphite.

In conclusion, it is possible to obtain nanodiamonds different in fluorescence emission properties starting from their synthesis, tuning azomethine ylides cycloaddition reaction conditions on graphite.

4. MATERIALS AND METHODS

Nanodiamonds characterization

Specific surface areas were measured by N_2 adsorption–desorption isotherms at 77 K using a Micromeritics ASAP 2020 instrument and SSA was calculated by the Brunauer–Emmett–Teller (BET) method. Before measurements, the nanomaterials were outgassed at r.t until a residual pressure of ca. 0.02 mbar, for 10 hours.

SEM micrographs were obtained with a Inspecy F™ scanning electron microscope (SEM) with Field Emission Gun. The system operates at a maximum accelerating voltage of 30 kV and probe current up to 2 µA, working in high vacuum (about 10^{-6} mbar). NDs were dispersed in isopropyl alcohol with a concentration of ~ 0.01 g/ml, sonicated and a droplet of the solutions was deposited on Si substrates. The samples under analysis were not metal coated so that, although leading to possible charging effects, we avoided any modification of NDs morphology. Secondary Electrons microscopy to obtain topographic micrographs with a spatial resolution of about 10 nm at 5 kV accelerating voltage. The dimensions distribution was assessed using Fiji software, an ImageJ-based open-source image processing package. The "watershed" feature from BioVoxxel toolbox [28][PA2] was applied to separate contiguous particles and it was followed by an extended particle analysis. The obtained areas were reconverted to diameters, assuming for simplicity the NDs to be like ideal perfect spheres. Nanodiamonds were initially dispersed in ultra-pure MilliQ® water and deposited on an approximately 1 cm^2 silicon wafer. The images were acquired by setting an electron acceleration voltage of 5 kV.

250 nm NDs: the samples were purchased by the company ElementSix®, whose nominal dimensions are between 0-250 nm and are produced by fragmentation of monocrystalline type Ib diamonds synthesized with the HPHT method. The concentration of nitrogen atoms is around 100 ppm.

50 nm NDs: HPHT monocrystalline synthetic NDs were purchased from Microdiamant AG (Switzerland) MSY 0-0.1 present a size ranging from few up to 100 nm, with a median size of 50 nm and a nominal concentration of single substitutional nitrogen around 100 ppm.

Studying NV centers-paramagnetic species dipolar interactions

Where not otherwise specified, the reagents and solvents were purchased from Sigma (Milan, Italy) and used without further purification.
Mesotetrakis (4-carboxyphenyl) porphyrin was purchased from Frontier Scientific (Logan, Utah, USA).

NMR spectra were recorded on an Avance 600 spectrometer (Jeol) operating at 14T, dissolving samples in proper deuterated solvent. Chemical shifts were referenced per residual solvent signals.
MS spectra were carried out using electrospray ionization (ESI) or by atmospheric pressure chemical ionization (APCI), in positive ion mode, on a Micromass ZQ spectrometer (Waters).
Thermogravimetric measurements were carried out on a TGA 4000 analyser (Perkin Elmer, Waltham, MA, USA) under a high purity argon atmosphere (90 mL min^{-1}), in the temperature range 50–800 °C, with a heating rate of 10 °C min–1 (ca.10 mg of sample were used for each analysis).
For T_1 and ODMR experiments a 532 nm laser for both spin and charge state initialization as well as detection was used. A series of bandpass filters to detect fluorescence from very narrow region (750-800) nm corresponding to NV$^-$ emission was employed. A single-photon counting module (Excelitas, SPCM-AQRH-14-FC) was used to detect the fluorescence. An acousto-optic modulator (AA Optoelectronics, MT 200-A0, 5-VIS) produced the excitation laser pulses, and programmable transistor-transistor logic (TTL) pulse generator (Spincore, Pulse-Blaster ESR-PRO) was used to generate the pulse sequences. A permanent magnet was mounted on a linear translation stage to apply a variable static magnetic field along the vertical (z) axis. 5 ms were chosen for initialization and reset time.
Samples preparation: 300 µL of deionized water were added to 1-2 mg nanodiamonds powder. After shaking and 5 minutes of sonication in ultrasound bath, 2 µL of each suspension were deposited on a glass and air dried. The obtained spots were about 2 mm wide.

Nanodiamond-Cetuximab nanosystems

Cetuximab (Erbitux®, 5 mg/ml) was obtained from A.O.U. Città della Salute e della Scienza di Torino.
CellTracker™ green CMFDA (ThermoFisher) was used.
Gel filtration of thiolated Cetuximab (I) is performed with Sephadex® PD-10 Desalting Column, bed volume 8.3 mL (packed bed dimensions 1.45x5.0 cm), G-25 Medium, particle size range 85-260 µm, gravity protocol volume 1-2.5 mL of PBS (pH 7).

Tuning graphitic and carboxylic surface

For the annealing and etching heat treatments was used a tubular oven ThermoConcept ROT 60/300/12 whose maximum achievable temperature is 1200°C, with a power of 3 kW. The control system allowed to set programmable treatment ramps according to user's needs. The samples are loaded inside the tube in a alumina manufactured shuttle. For annealing treatments, a continuous laminar flow of inert gas (Ar or N_2) of about 0.2 l min^{-1} was established inside the tube, controlled by a Key Instruments FR2A12BVBN flow meter. As for the etching treatments, for the entire duration of the treatment O_2 is fluxed or the sample was kept in the air.
Raman/Photoluminescence spectra of the oxidized samples were acquired with a Horiba Jobin Yvon HR800 Raman micro-spectrometer equipped with a continuous NdYAG 532 nm excitation laser, focused with a 20× air objective, and a CCD detection system with Peltier cooling system (- 70 °C). The system allows the acquisition of spectra with a spatial resolution of 2 µm in diameter and 3 µm in focal depth. A 600 lines mm^{-1} diffraction grating guarantees a spectral resolution of 3 cm^{-1}. In all measurements, the effective power incident on the sample was 17 mW and the acquisition time was set to 1 second, averaging 3 repeated acquisitions. The samples were prepared dispersing the NDs powders in isopropyl alcohol and depositing a thick and dense layer on silicon substrates. A 20× objective was used to acquire a signal coming from a relatively wide sample area. For FTIR measurements, the instrument used (Bruker IFS 66 FTIR) is equipped with a globar source that generates polychromatic light in the infrared region. A MCT detector is based on mercury cadmium telluride (HgCdTe)

operating at low temperatures in the mid-infrared region (from 400 cm-1 to 4000 cm-1). The detector is cooled through a liquid nitrogen system. The spectra were acquired with a resolution equal to 2 cm-1 averaged over 256 acquisitions.

Making high fluorescent nanodiamonds

For the creation of NV centers in nanodiamonds the accelerator AN2000 was used, located at the Legnaro National Laboratories (INFN). It is a Van der Graaf type electrostatic accelerator with single loading stage and has a terminal voltage of 2 MV. The particles that were accelerated with monovalent protons or helium ions. A 60° beam line was used. The treatment chamber is equipped with a manoeuvrable sample holder, which allows movements with micrometric precision. In addition, it is possible to rotate it with a step of 1°, allowing sample inclination with respect to the beam direction. The spot diameter ranges from a few hundred µm up to about 5 mm, depending on the generated ionic current.

Raman/Photoluminescence spectra of NDs were acquired as èreviously described.

Graphite powder (median size 7–10 µm) was purchased from Alfa Aesar (Ward Hill, MA, USA). Chemicals were purchased in reagent grade from Sigma Aldrich (Saint Louis, MO, USA) and Alfa Aesar and were used without further purification.

Ca. 200 mg of graphite were pressed at 50 bar to form targets of 1 cm diameter and 1 mm thickness.

Pulsed laser ablation of the N-doped graphite target was performed by using a KrF excimer laser (Lambda-Physik Coherent LPX220i) having a wavelength of λ = 248 nm, pulse duration τ = 20 ns and repetition rate of 10 Hz. The target was placed in a glass vial, which was then filled with water till a ~5 mm thick liquid layer covers the top surface of the target. The laser beam was focused on the target surface with a 40 cm-focal length lens, to form a laser spot size of ~1 mm^2. Laser single-pulse energy was set to ~500 mJ, for a total of 3000 pulses. Once the ablation was performed, the target was removed from the vial, and the liquid-suspended powder was slowly dried in an oven. Finally, the powder was dispersed in 250 µL of isopropanol and then 2 µL were deposited on a substrate for characterization.

Morphological and compositional analysis of the laser-synthesized samples was performed with a JEOL LSM-7001F Field Emission Scanning Electron Microscopy (SEM), using a working distance (WD) of 10 mm and with an energy beam of 20 keV.

Raman and photoluminescence characterizations were made with a Jobin- Yvon Horiba LabRam Aramis confocal micro-Raman system, operated in the following set: confocal hole 1000 µm, slit width 100 µm and grating 1800 lines/mm. The excitation source was a DPSS laser with 532 nm wavelength, and the signal was collected with an air-cooled multichannel CCD in the range 100–8000 cm–1 (corresponding to 535–926 nm with a 532 nm excitation), with an accuracy of ±1 cm^{-1}. Wide-field PL imaging was performed with a Nikon Ti-E inverted wide-field microscope using a 532 nm laser pump (model: CNI laser mod. MGL-III-532/50 mW). The PL signal was collected by a 40× (NA = 0.75 and 0.66 mm working distance) refractive objective, and then filtered by a TRITC (Tetramethylrhodamine) dichroic beamsplitter, before being measured by an sCMOS camera (ORCA-Flash4.0 V2, Hamamatsu, Hamamatsu City, Japan). ODMR spectra were obtained with the same apparatus: under continuous laser excitation, the RF signal, which was obtained with a WindFreak RF generator (SynthHD v1.4 54 MHz–13.6 GHz) and amplified with a Mini Circuits ZVE- 3W-83+ 2W RF, are delivered on the sample with a homemade Au-coated copper loop terminated with a high power RF dumper. The temporal sequence of the experiment (RF delivery and camera acquisition) was obtained by suitably programming a SpinCore 100 MHz TTL generator (Mod. TTL: PB12-100-4K). Finally, the collected images were processed with the Nikon software NIS-Elements Advanced Research.

5. EXPERIMENTAL SECTION

5.1 Synthetic procedures for NDs-paramagnetic species nanosystems

Synthesis of tert-butyl (2-aminoethyl)carbamate (a)

3.34 ml of ethane-1,2-diamine (50 mmol) are dissolved in 30 mL of dichloromethane and the solution was cooled down to 0 °C. Maintaining the mixture temperature between 0 °C and 5 °C, A solution of *tert*butyldicarbonate (1.09g, 5 mmol) in dichloromethane (5 ml) are slowly added, and subsequently, the reaction mixture was allowed to stir at room temperature for 24 h. The pH value was then adjusted to 7 by adding HCl 0.1M and the mixture was stirred at room temperature for 24 h. HCl 0.1M was then added to the solution until pH value was decreased down to 4 and the mixture was extracted with DCM (3×10 ml). A second extraction with DCM (3×10 ml) was carried out after increasing pH to 9 by addition of NaOH 0.5M solution. The organic layer resulting from the second extraction was dried over sodium sulphate and the solvent was removed under reduced pressure, obtaining the desired product as pale-yellow oil (668 mg, 4.17 mmol, 86% yield).

Mass spectrometry (MS) and Nuclear Magnetic Resonance (NMR) were performed.

MS ESI+: calculated for $C_7H_{16}N_2O_2$ 160.21, found $[M+H]^+$= 161.01 , $[M+Na]^+$= 183.01.

^{1}H NMR (600 MHz, $CDCl_3$): δ = 5.004 (bs, 1H, *4*), 3.145 (m, 2H, *5*), 2.773 (t, *J* = 6 Hz, 2H, *6*), 1.411 (s, 9H, *1*).

^{13}C NMR (600 MHz, $CDCl_3$): δ = 155.973 (*3*), 78.905 (*2*), 42.981 (*5*), 41.535 (*6*), 28.054 (*1*).

Synthesis of tert-butyl N-(8-amino-3,6-dioxaoctyl)carbamate (b)

9.94 ml of 1,8-diamino-3,6-dioxaoctane (67.7. mmol) were dissolved in 200 ml of a mixture of H2O/ethanol 1:1 and the solution was cooled down to 0 °C. Maintaining the mixture temperature between 0 °C and 5 °C, a solution of *tert*butyldicarbonate (9.85g, 45.1 mmol) in dioxane (74 ml) was slowly added, and subsequently, the reaction mixture was allowed to stir at 0 °C for 4 h. The pH value was then adjusted to 7 by adding HCl 0.1M and the mixture was stirred at room temperature for 24 h. HCl 0.1M was then added to the solution until pH value was decreased down to 4 and the mixture was extracted with DCM (3×50 ml). A second extraction with DCM (3×50 ml) was carried out after increasing pH to 9 by addition of NaOH 0.5M solution. The organic layer resulting from the second extraction was dried over sodium sulphate and the solvent was removed under reduced pressure, obtaining the desired product as pale-yellow oil (10.5g, 42.4 mmol, 94% yield).

MS-ESI+: calculated for $C_{11}H_{24}N_2O_4$ 248.17, found $[M+H]^+$=249.28,
$[M+Na]^+$=271.16

^{1}H NMR (600 MHz, $CDCl_3$): δ = 5.152 (bs, 1H, *4*), 3.606 (s, 4H, *7*,*8*), 3.535 (t, *J* = 4.8 Hz, 2H, *6*), 3.505 (t, *J* = 4.8 Hz, 2H, *9*), 3.312 (m, 2H, *5*), 2.868 (t, *J* = 4.8 Hz, 2H, *10*), 1.427 (s, 9H, *1*).

^{13}C NMR (600 MHz, $CDCl_3$): δ = 156.142 (*3*), 79.286 (*2*), 73.598 (*7,8*), 70.324 (*9*), 41.877 (*5*), 40.441 (*10*), 28.539 (*1*).

Synthesis of tert-butyl (2-((furan-2-ylmethyl)amino)ethyl)carbamate (c)

Compound (a) (500 mg, 3.10 mmol) was dissolved in methanol (15 ml) and then the pH was adjusted to 5 by adding HCl 0.1 M. A solution of freshly distilled furfural (171 µl, 2.05 mmol) in DCM (15 ml) was added to the mixture and stirred at room temperature for 2 h. Then, solid $NaBH_3CN$ (236 mg, 3.72 mmol) was added stepwise (3 portions, one each 30 min) maintaining the pH value around 5. After stirring for 12 h, the solvent was removed under vacuum, the residue dissolved in DCM (25 ml) and washed with water (25 ml). The aqueous layer was extracted with DCM (3×30 ml), the organic phases were combined, dried over sodium sulphate and subsequently the solvent was removed. The final product was recovered as dark yellow oil (360 mg, 1.50 mmol, 73% yield).

MS-ESI+: calculated for $C_{12}H_{20}N_2O_3$ 240.3, found $[M+H]^+$=241.04.
^{1}H NMR (600 MHz, $CDCl_3$): δ = 7.357 (s, 1H, *12*), 6.313 (dd, *J* = 1.8, 3.0 Hz, 1H, *11*), 6.188 (d, *J* = 3.6 Hz, 1H, *10*), 5.001 (bs, 1H, *4*), 3.793 (s, 2H, *8*), 3.226 (m, 2H, *5*), 2.744 (t, *J* = 5.4 Hz, 2H, *6*), 2.079 (s, 1H, *7*), 1.433 (s, 9H, *1*).
^{13}C NMR (600 MHz, $CDCl_3$): δ = 156.107 (*3*), 153.110 (*9*), 141.994 (*12*), 110.167 (*11*), 107.323 (*10*), 79.221 (*2*), 48.103 (*8*), 45.585 (*5*), 40.070 (*6*), 28.322 (*1*).

Synthesis of tert-butyl (2-(2-(2-((furan-2-ylmethyl)amino)ethoxy)ethoxy)ethyl) carbamate (d)

Compound (b) (202 mg, 0.81 mmol) was dissolved in methanol (7 ml) and then the pH was adjusted to 5 by adding HCl 0.1 M. A solution of freshly distilled furfural (45 µl, 0.54 mmol) in DCM (7 ml) was added to the mixture and stirred at room temperature for 2h. Then, solid $NaBH_3CN$ (51 mg, 0.82 mmol) was added stepwise (3 portions, one each 30 min) maintaining the pH value around 5. After stirring for 12 h, the solvent was removed under vacuum, the residue dissolved in DCM (15 ml) and washed with water (15 ml). The aqueous layer was extracted with DCM (3×15 ml), the organic phases were combined, dried over sodium sulphate and subsequently the solvent was removed. The final product was recovered as dark yellow oil (110 mg, 0.34 mmol, 62% yield).
MS-ESI+: calculated for $C_{16}H_{28}N_2O_5$ 328.20, found $[M+H]^+$=329.10.
^{1}H NMR (600 MHz, $CDCl_3$): δ = 7.377 (s, 1H, *4*), 6.326 (m, 1H, *13*), 6.284 (m, 1H, *14*), 5.190 (bs, 1H, *16*), 3.902 (s, 2H, *11*), 3.662 (m, 2H, *8*), 3.609 (s, 2H, *7*), 3.538 (t, *J* = 4.8 Hz, 2H, *6*), 3.479 (m, 2H, *9*), 3.302 (m, 2H, *5*), 2.873 (m, 2H, *10*), 1.433 (s, 9H, *1*).
^{13}C NMR (600 MHz, $CDCl_3$): δ = 156.158 (*3*), 154.245 (*12*), 142.851 (*15*), 110.756 (*13*), 107.951 (*14*), 70.351 (*7,8*), 57.530 (*6,9*), 48.157 (*11*), 45.196 (*5*), 40.573 (*10*), 28.634 (*1*).

Synthesis of NDs-short linker and NDs-long linker (1)-a, (1)-aea, (2)-a, (2)-aea

60 mg of annealed or annealed-etched-annealed NDs and 0.125 mmol of linker (compound (c) 30 mg, compound (d) 41 mg) were suspended in 6 mL DMF. The mixture was reacted at 130°C for 2 hours under magnetic stirring. After cooling to

room temperature, the suspensions were centrifuged (6000 rpm, 8 min) and the supernatant discarded. NDs were subjected to several centrifugation cycles (water, 6000 rpm, 8 min, 3×; methanol, 6000 rpm, 8 min, 3×; dichloromethane, 6000 rpm, 8 min, 3×), then dried at 50°C for 12 h, yielding to NDs-linker (1)-a, (1)-aea, (2)-a, (2)-aea.
(1) MW = 240.3 g/mol, (2) MW = 328.41.

Synthesis of NDs-AAZTAtBoc and NDs-CEDTAtBoc (3)-a, (3)-aea, (4)-a, (4)-aea, (5)-a, (5)-aea, (6)-a, (6)-aea

NDs-short linker and NDs-long linker were conjugated with chelating agents shown in Figure E1.

AAZTA(tBu)C4COOH
(MW = 671.86)

CEDTA(tBu)
(MW = 560.69)

E1. AAZTA(tBu)C4COOH and CEDTA(tBu) chelant agents for Gd and Mn respectively, used for the synthesis of NDs-chelant nanosystems.

50 mg of NDs-linker (1) and (2) were suspended in 1 mL of dichloromethane, 1 mL of trifluoroacetic acid and 1 drop of anisol and reacted for 2 hours at room temperature. The reaction mixture was diluted with 3 mL dichloromethane, centrifuged (6000 rpm, 8 min) and the supernatant discarded. NDs are subjected to several centrifugation cycles (dichloromethane, 6000 rpm, 8 min, 6×), then dried at 50°C for 2 h, leading to NDs-linker-NH_2.

On the base of linker surface loadings estimated by thermogravimetry, the conjugation reaction was performed taking into account the amino groups grafted on NDs surface (1 eq).

30 mg of NDs-linker-NH_2, chelating agent (3 eq), HBTU (4 eq) and DIPEA (10 eq) were suspended in 1 mL DMF and reacted for 3 hours at 50°C, under magnetic stirring. The suspensions were centrifuged (6000 rpm, 8 min) and the supernatant discarded. NDs were subjected to several centrifugation cycles (water, 6000 rpm, 8 min, 3×; methanol, 6000 rpm, 8 min, 3×; dichloromethane, 6000 rpm, 8 min, 3×), then dried at 50°C for 12 h, yielding to NDs-chelant (3), (4), (5) and (6).
(3) MW = 794.04 g/mol, (4) MW = 882.27, (5) MW = 684.86 g/mol, (6) MW = 772.97 .

Synthesis of NDs-Gd and NDs-Mn (7)-a, (7)-aea, (8)-a, (8)-aea, (9)-a, (9)-aea, (10)-a, (10)-aea

30 mg of NDs-chelator are suspended in 1 mL of dichloromethane, 1 mL of trifluoroacetic acid and 1 drop of anisol and reacted for 2 hours at room temperature. The reaction mixture is diluted with 3 mL dichloromethane, centrifuged (6000 rpm, 8 min) and the supernatant discarded. NDs are subjected to several centrifugation cycles (dichloromethane, 6000 rpm, 8 min, 6×), then dried at 50°C for 2 h, leading to NDs-chelator-COOH.
30 mg of NDs-chelator-COOH were suspended in 3 mL of a 15 mM paramagnetic agent pH 5 aqueous solution ($GdCl_3*6H_2O$ or $MnCl_2*4H_2O$) and sonicated for 15 minutes. The suspension was reacted for 1 hour at 55°C, under magnetic stirring. The suspensions were centrifuged (6000 rpm, 8 min) and the supernatant discarded. NDs were subjected to centrifugation cycles (water, 6000 rpm, 8 min, 3×); 1 mL of a pH 5 solution of EDTA is added to NDs and the suspension is sonicated for 10 minutes at room temperature, then centrifuged (6000 rpm, 8 min) and the supernatant discarded. NDs were subjected to centrifugation cycles (water, 6000 rpm, 8 min, 3×) methanol, 6000 rpm, 8 min, 3×; dichloromethane, 6000 rpm, 8 min, 3×), then dried at 60°C for 12 h, yielding to NDs-paramagnetic (7), (8), (9) and (10).

Synthesis of NDs-Mn(II) and NDs-Mn(III) (9)-Mn(II), (10)-Mn(II), (9)-Mn(III), (10)-Mn(III)

10 mg of NDs-Mn (9) and (10) were suspended in 1 mL of a 50 mM solution of sodium thiosulphate, leading to NDs-Mn(II).

Samples were ready for T_1 experiments.
10 mg of NDs-Mn (9) and (10) were suspended in 1 mL of a 50 mM solution of hydrogen peroxide, leading to NDs-Mn(III). Samples were ready for T_1 experiments.

Synthesis of NDs-Lys (11)

In a round bottom flask, 50 mg of NDs were suspended in 10 mL of solvent. Paraformaldehyde (1.67 mmol, 50 mg) and lysine (2.00 mmol, 292 mg) then were added.
The reaction mixtures were sonicated for 10', then reacted at 130°C for 2h under magnetic stirring
After cooling to room temperature, the suspensions are centrifuged (6000 rpm, 8 min) and the supernatant discarded. NDs were subjected to several centrifugation cycles (water, 6000 rpm, 8 min, 3×; methanol, 6000 rpm, 8 min, 3×; dichloromethane, 6000 rpm, 8 min, 3×), then dried at 100°C for 12 h, yielding to NDs-Lys (11) (MW = 114 g/mol).

Synthesis of NDs-AAZTAtBoc and NDs-CEDTAtBoc (12)-250-a, (12)-250-aea, (12)-50-a, (12)-50-aea, (13)-250-a, (13)-250-aea, (13)-50-a, (13)-50-aea

On the basis of linker surface loadings estimated by thermogravimetry, the conjugation reaction was performed taking into account the amino groups grafted on NDs surface (1 eq).
30 mg of NDs-linker-NH_2, chelating agent (3 eq), HBTU (4 eq) and DIPEA (10 eq) were suspended in 1 mL DMF and reacted for 3 hours at 50°C, under magnetic stirring. The suspensions were centrifuged (6000 rpm, 8 min) and the supernatant discarded. NDs were subjected to several centrifugation cycles (water, 6000 rpm, 8 min, 3×; methanol, 6000 rpm, 8 min, 3×; dichloromethane, 6000 rpm, 8 min, 3×), then dried at 50°C for 12 h, yielding to NDs-chelator (12), (13).
(12) MW = 785.09 g/mol, (13) MW = 673.90.

Synthesis of NDs-Gd and NDs-Mn (14)-250-a, (14)-250-aea, (14)-50-a, (14)-50-aea, (15)-250-a, (15)-250-aea, (15)-50-a, (15)-50-aea

30 mg of NDs-chelator are suspended in 1 mL of dichloromethane, 1 mL of trifluoroacetic acid and 1 drop of anisol and reacted for 2 hours at room temperature. The reaction mixture was diluted with 3 mL dichloromethane, centrifuged (6000 rpm, 8 min) and the supernatant discarded. NDs are subjected to several centrifugation cycles (dichloromethane, 6000 rpm, 8 min, 6×), then dried at 50°C for 2 h, leading to NDs-chelator-COOH.

30 mg of NDs-chelator-COOH were suspended in 3 mL of a 15 mM paramagnetic agent pH 5 aqueous solution ($GdCl_3*6H_2O$ or $MnCl_2*4H_2O$) and sonicated for 15 minutes. The suspension was reacted for 1 hour at 55°C, under magnetic stirring. The suspensions were centrifuged (6000 rpm, 8 min) and the supernatant discarded. NDs were subjected to centrifugation cycles (water, 6000 rpm, 8 min, 3×); 1 mL of a pH 5 solution of EDTA is added to NDs and the suspension is sonicated for 10 minutes at room temperature, then centrifuged (6000 rpm, 8 min) and the supernatant discarded. NDs were subjected to centrifugation cycles (water, 6000 rpm, 8 min, 3×) methanol, 6000 rpm, 8 min, 3×; dichloromethane, 6000 rpm, 8 min, 3×), then dried at 60°C for 12 h, yielding to NDs-paramagnetic (14), (15).

Synthesis of NDs-COOH (16)

In a round bottom flask, 100 mg of 50 nm annealed NDs were suspended in 10 mL of sulfonitric mixture (nitric acid: sulfuric acid 1:3) and stirred overnight at reflux. The suspension was centrifuged (6000 rpm, 8 min) and the supernatant was discarded. NDs were suspended in 10 mL NaOH 1M and reacted for 3 hours at reflux under magnetic stirring. The suspension was centrifuged (6000 rpm, 8 min) and the supernatant was discarded. Then NDs were suspended in 10 mL HCl 1M and reacted for 3 hours at reflux under magnetic stirring. The suspension was centrifuged (6000 rpm, 8 min) and the supernatant was discarded. NDs were subjected to several centrifugation cycles (water, 6000 rpm, 8 min, 5×; methanol, 6000 rpm, 8 min, 3×; dichloromethane, 6000 rpm, 8 min, 3×), then dried at 100°C for 12 h.

5.2 Characterization of NDs-paramagnetic species nanosystems

Surface loadings were estimated starting from weight % loss, with respect to bare NDs. Surface loadings, expressed in µmol of adduct / mg NDs were calculated from weight loss % at 650°C from thermogravimetric profiles. Surface loadings of NDs-chelating agents are estimated considering the weight loss % caused by the grafted linker and the chelating agent.

5.2.1 Nanosystems obtained with the Diels-Alder approach

In Figure E2 chelating surface loading estimations are reported. MW of both linkers and chelating agents are considered:

(1)-a, (1)-aea: 240.3 g/mol
(2)-a, (2)-aea: 328.41 g/mol
(3)-a, (3)-aea: 794.04 g/mol
(4)-a, (4)-aea 882.27 g/mol
(5)-a, (5)-aea 684.86 g/mol
(6)-a, (6)-aea 772.97 g/mol

Sample		Thermogravimetric analysis			
		Δm %		Surface loading (μmol/mg)	
		NDs-linker	NDs-chelant	NDs-linker	NDs-chelant
Gadolinium	(3)-a	5.5 ±0.5	13.6 ±0.5	0.22 ±0.02	0.14 ±0.01
	(3)-aea	1.6 ±0.5	2.8 ±0.5	0.06 ±0.02	0.01 ±0.01
	(4)-a	2.6 ±0.5	6.6 ±0.5	0.07 ±0.02	0.06 ±0.01
	(4)-aea	3.9 ±0.5	5.2 ±0.5	0.11 ±0.02	0.02 ±0.01
Manganese	(5)-a	5.5 ±0.5	6.9 ±0.5	0.22 ±0.02	0.02 ±0.01
	(5)-aea	1.6 ±0.5	3.2 ±0.5	0.06 ±0.02	0.03 ±0.01
	(6)-a	2.6 ±0.5	5.3 ±0.5	0.07 ±0.02	0.05 ±0.01
	(6)-aea	3.9 ±0.5	6.5 ±0.5	0.11 ±0.02	0.04 ±0.01

E2. Surface loading estimations of NDs-chelant agents, starting from weight loss % calculated from thermogravimetric analysis. NDs-AAZTA short (3) and long (4) systems and NDs-CEDTA short (5) and ling (6) systems are analysed.

In Figure E3 chelator surface loading estimations are shown in diagram bars.

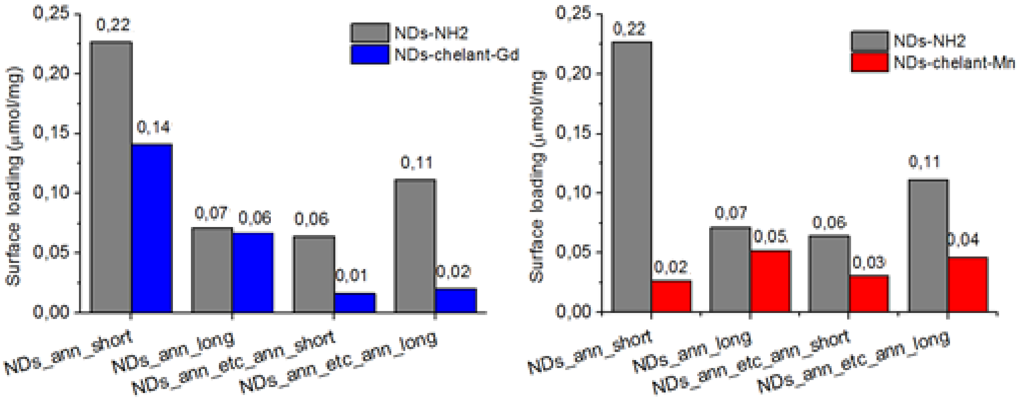

E3. Diagram bars showing surface loading estimations of NDs-AAZTA (blu bars) and NDs-CEDTA (red bars) systems. Linker surface loadings (grey bars) are reported as well. Errors are shown in figure E2.

5.2.2 Nanosystems obtained with the 1,3-dipolar approach

In Figure E4 chelators surface loading estimations are reported. MW of both linkers and chelant agents are considered:

NDs-Lys (11): 114.23 g/mol
(12)-250-a, (12)-250-aea, (12)-50-a, (12)-50-aea: 785.09 g/mol
(13)-250-a, (13)-250-aea, (13)-50-a, (13)-50-aea: 673.90 g/mol

Sample		**Thermogravimetric analysis**			
		Δm %		Surface loading (µmol/mg)	
		NDs-linker	NDs-chelant	NDs-linker	NDs-chelant
Gadolinium	(12)-250-a	12.2 ±0.5	19.6 ±0.5	0.12 ±0.02	0.02 ±0.01
	(12)-250-aea	14.0 ±0.5	20.5 ±0.5	0.14 ±0.02	0.03 ±0.01
	(12)-50-a	16.9 ±0.5	41.2 ±0.5	0.17 ±0.02	0.05 ±0.01
	(12)-50-aea	15.5 ±0.5	24.2 ±0.5	0.16 ±0.02	0.02 ±0.01
Manganese	(13)-250-a	12.2 ±0.5	21.0 ±0.5	0.12 ±0.02	0.03 ±0.01
	(13)-250-aea	14.0 ±0.5	20.4 ±0.5	0.14 ±0.02	0.02 ±0.01
	(13)-50-a	16.9 ±0.5	22.7 ±0.5	0.17 ±0.02	0.02 ±0.01
	(13)-50-aea	15.5 ±0.5	24.7 ±0.5	0.16 ±0.02	0.01 ±0.01

E4. Surface loading estimations of NDs-chelant agents, starting from weight loss % calculated from thermogravimetric analysis. NDs-AAZTA short (3) and long (4) systems and NDs-CEDTA short (5) and ling (6) systems are analysed.

5.3 Synthetic procedures for NDs-porphyrin nanosystems

Cycloaddition reaction on NDs (11)-50-a

In a round bottom flask, 50 mg of NDs were suspended in 10 mL of DMF. Paraformaldehyde (1.66 mmol, 50 mg) and lysine (2.00 mmol, 292 mg) then were added. The reaction mixtures were sonicated for 10′, then reacted at 130°C for 2h under magnetic stirring.

After cooling to room temperature, the suspensions were centrifuged (6000 rpm, 8 min) and the supernatant discarded. NDs were subjected to several centrifugation cycles (water, 6000 rpm, 8 min, 3×; methanol, 6000 rpm, 8 min, 3×; dichloromethane, 6000 rpm, 8 min, 3×), then dried at 100°C for 12 h, yielding to NDs-NH_2 (11)-50-a.

Conjugation with porphyrin (17)

Porphyrin molar equivalents were calculated on the base of NDs-NH_2 (11)-50-a surface loading, estimated by TGA (0.109 mmol/100mg).

To a suspension of 60 mg of NDs-NH_2 (11)-50-a (0.0654 mmol of NH_2) in 10 mL of DMF, 5,10,15,20-tetrakis(4-carboxyphenyl)porphyrin (3 eq, 0.196 mmol, 99 mg), (2-(1H-benzotriazol-1-yl)-1,1,3,3-tetramethyluronium hexafluorophosphate (HBTU, 4 eq, 0.654 mmol, 87 mg,) and N,N-Diisopropylethylamine (DIPEA, 10 eq, 0.112 mmol, 85 mg, 115 µL) were added. The suspension was stirred at room temperature for 3h. The suspension was centrifuged (6000 rpm, 8 min) and the supernatant discarded. NDs were subjected to several centrifugation cycles (water, 6000 rpm, 8 min, 3×; methanol, 6000 rpm, 8 min, 3×; dichloromethane, 6000 rpm, 8 min, 3×), then dried at 100°C for 12 h, yielding to NDs-porphyrin (17).

5.4 Characterization of NDs-porphyrin nanosystems

NDs-NH_2 (11)-50-a and NDs-porphyrin nanosystems (17) thermogravimetric derivative profiles show thermal transitions of the respective adducts (Figure E5).

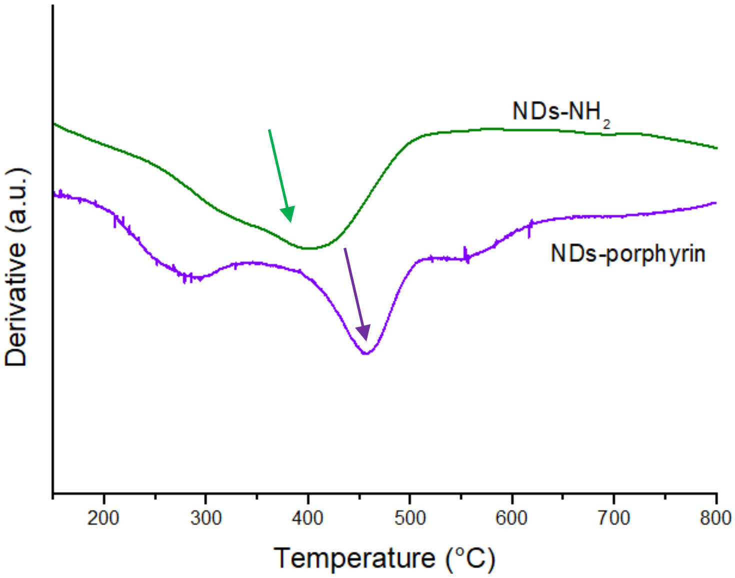

E5. Derivatives of NDs-NH_2 (green line) and NDs-porphyrin (purple line) nanosystems thermogravigrams, showing typical thermal transitions (arrows).

Surface loadings were then estimated starting from weight % loss, with respect to bare NDs (Figure E6).

NDs	**Thermogravimetric analysis**	
	Δm(%)	**Surface loading (mmol/100mg)**
NDs-NH_2 (11)-50-a	12.4 ±0.5	0.11 ±0.02
ND-porphyrin (17)	24.2 ±0.5	0.02 ±0.01

E6. NDs-pyrrolidine (11)-50-a and NDs-porphyrin (17) surface loading estimations.

Surface loadings, expressed in mmol of adduct / 100 mg NDs were calculated from nanosystems thermogravimetric weight loss % at 650°C profiles, considering adduct MW:

(11)-50-a: 114 g/mol, weight loss 12.4%;
(17): 775 g/mol, weight loss 24.2-12.4 = 11.8% (referred to the porphyrin component)

Porphyrin surface loading was expressed as mmol of porphyrins / 100 mg bare NDs, taking in to account the weight loss caused by pyrrolidine cycloaddition adduct.
Porphyrin conjugation yield was calculated as mmol porphyrins / 100 mg bare NDs and mmol pyrrolidine adducts / 100 mg bare NDs ratio.
Conjugation yield: 0.02/0.11 = 26%

5.5 Graphitic surface tunability with azomethine ylides

Surface loadings, expressed in mmol of adduct / 100 mg NDs, were calculated from nanosystems thermogravimetric weight loss % at 650°C profiles, considering the MW of the adduct.

Synthesis and characterization of 2-aminobutyl-NDs in different solvents (11)-s1, s2, s3, s4

In a round bottom flask, 50 mg of NDs were suspended in 10 mL of solvent. Paraformaldehyde (1.67 mmol, 50 mg) and lysine (2.00 mmol, 292 mg) then were added. In the case of DMF/water mixture, water (8.35 mmol, 150mg, 150µL) was added. The reaction mixtures were sonicated for 10’, then reacted at 130°C for 2h under magnetic stirring.
After cooling to room temperature, the suspensions were centrifuged (6000 rpm, 8 min) and the supernatant discarded. NDs were subjected to several centrifugation cycles (water, 6000 rpm, 8 min, 3×; methanol, 6000 rpm, 8 min, 3×; dichloromethane, 6000 rpm, 8 min, 3×), then dried at 100°C for 12 h, yielding to NDs-NH_2 (11) s1, s2, s3, s4 (MW = 114 g/mol).

Thermogravimetric profiles (Figure E7) and surface loadings estimations (Figure E8) are reported.

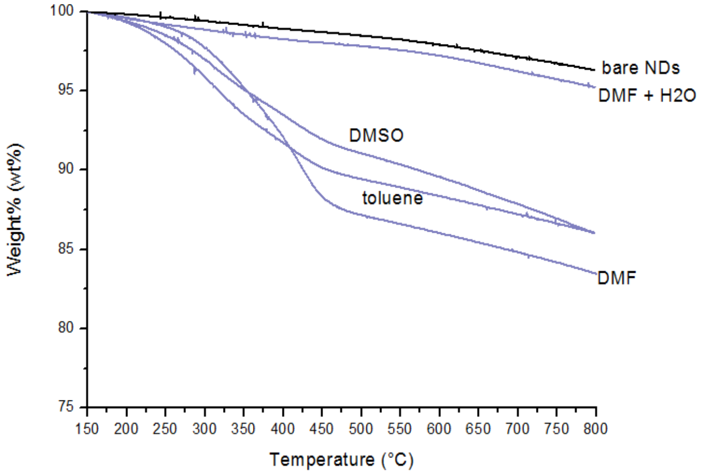

E7. Thermogravimetric profiles of NDs reacted with lysine and paraformaldehyde, in different solvents: DMF and water, DMSO, toluene and DMF.

NDs	**Thermogravimetric analysis**	
	Δm(%)	**Surface loading (mmol/100mg)**
NDs-(11)-s1	13.1 ±0.5	0.11 ±0.02
NDs-(11)-s2	7.3 ±0.5	0.06 ±0.02
NDs-(11)-s3	6.4 ±0.5	0.05 ±0.02
NDs-(11)-s4	0.6 ±0.5	0.01 ±0.02

E8. NDs-DMF (11)-s1, NDs-toluene (11)-s2, NDs-DMSO (11)-s3 and NDs-DMF+H_2O (11)-s4 surface loading estimations

Synthesis and characterization of 2-aminobutyl-NDs with different reaction times (11)-t1, t2, t3, t4

In a round bottom flask, 50 mg of NDs were suspended in 10 mL of DMF. Paraformaldehyde (1.67 mmol, 50 mg) and lysine (2.00 mmol, 292 mg) then were added. The reaction mixtures were sonicated for 10', then reacted at 130°C for the selected time under magnetic stirring.

After cooling to room temperature, the suspensions were centrifuged (6000 rpm, 8 min) and the supernatant discarded. NDs were subjected to several centrifugation cycles (water, 6000 rpm, 8 min, 3×; methanol, 6000 rpm, 8 min, 3×; dichloromethane, 6000 rpm, 8 min, 3×), then dried at 100°C for 12 h, yielding to NDs-NH_2 (11)-t1, t2, t3, t4 (MW = 114 g/mol).

Thermogravimetry and grafting estimations are reported (Figure E9 and E10).

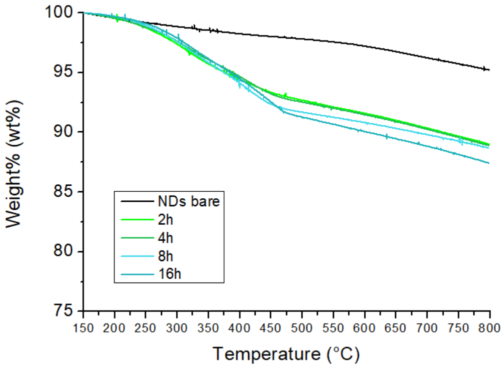

E9. Thermogravimetric profiles of NDs reacted with lysine and paraformaldehyde, at different times (2h, 4h, 6h, 8h).

NDs	Thermogravimetric analysis	
	Δm(%)	Surface loading (mmol/100mg)
NDs-(11)-t1	6.0 ±0.5	0.05 ±0.01
NDs-(11)-t2	6.0 ±0.5	0.05 ±0.01
NDs-(11)-t3	6.3 ±0.5	0.05 ±0.01
NDs-(11)-t4	7.3 ±0.5	0.06 ±0.01

E10. NDs-(11)-t1, NDs-(11)-t2, NDs-(11)-t3, NDs-(11)-t4 surface loading estimations.

Synthesis and characterization of 2-aminobutyl-NDs at different concentrations NDs-Lys (Q/4, Q/2, Q, Qx2, Qx4)

In a round bottom flask, 50 mg of NDs were suspended in 10 mL of DMF. Paraformaldehyde (condition Q/4: 0.21 mmol, 6.25 mg; condition Q/2: 0.42 mmol, 12.5 mg; condition Q: 0.83 mmol, 25 mg; condition Qx2: 1.67 mmol, 50 mg; condition Qx4: 3.33 mmol, 100 mg) and lysine (condition Q/4: 0.25 mmol, 36.5 mg; condition Q/2: 0.50 mmol, 73 mg; condition Q: 1.00 mmol, 146 mg; condition Qx2: 2.00 mmol, 292 mg; condition Qx4: 4.00 mmol, 585 mg) then were added. The reaction mixtures were sonicated for 10', then reacted at 130°C for 2h under magnetic stirring.
After cooling to room temperature, the suspensions were centrifuged (6000 rpm, 8 min) and the supernatant discarded. NDs were subjected to several centrifugation cycles (water, 6000 rpm, 8 min, 3×; methanol, 6000 rpm, 8 min, 3×; dichloromethane, 6000 rpm, 8 min, 3×), then dried at 100°C for 12 h, yielding to NDs-Lys (Q/4, Q/2, Q, Qx2, Qx4) (MW = 114 g/mol).

Surface loadings estimations are reported (Figure E11).

NDs	**Thermogravimetric analysis**	
	Δm(%)	**Surface loading (mmol/100mg)**
NDs-Lys (Q/4)	1.9 ±0.5	0.02 ±0.02
NDs-Lys (Q/2)	3.3 ±0.5	0.03 ±0.02
NDs-Lys (Q)	6.0 ±0.5	0.05 ±0.02
NDs-Lys (Qx2)	12.4 ±0.5	0.10 ±0.02
NDs-Lys (Qx4)	20.8 ±0.5	0.18 ±0.02

E11. NDs-Lys (Q/4). NDs-Lys (Q/2), NDs-Lys (Q). NDs-Lys (Qx2) and NDs-Lys (Qx4) surface loading estimations.

Synthesis and characterization of 2-mercaptomethylpyrrolidin-NDs NDs-Cys (Q/4, Q/2, Q, Qx2, Qx4)

In a round bottom flask, 25 mg of NDs were suspended in 5 mL of DMF. Paraformaldehyde (condition Q/4: 0.11 mmol, 3.6 mg; condition Q/2: 0.21 mmol, 6.3 mg; condition Q: 0.42 mmol, 12.5 mg; condition Qx2: 0.83 mmol, 25 mg; condition Qx4: 1.67 mmol, 50 mg) and cysteine were added (condition Q/4: 0.13 mmol, 16 mg; condition Q/2: 0.25 mmol, 31 mg; condition Q: 0.50 mmol, 61 mg; condition Qx2: 1.00 mmol, 122 mg; condition Qx4: 2.00 mmol, 242 mg). The reaction mixture was sonicated for 10’, then reacted at 130°C for 2h under magnetic stirring.

After cooling to room temperature, the suspension was centrifuged (6000 rpm, 8 min) and the supernatant discarded. NDs were subjected to several centrifugation cycles (water, 6000 rpm, 8 min, 3×; methanol, 6000 rpm, 8 min, 3×; dichloromethane, 6000 rpm, 8 min, 3×), then dried at 100°C for 12 h, yielding to NDs-Cys (Q/4, Q/2, Q, Qx2, Qx4) (MW = 89 g/mol).

Surface loadings estimations (Figure E12) are reported.

NDs	**Thermogravimetric analysis**	
	Δm(%)	**Surface loading (mmol/100mg)**
NDs-Cys (Q/4)	1.4 ±0.5	0.02 ±0.02
NDs-Cys (Q/2)	2.8 ±0.5	0.03 ±0.02
NDs-Cys (Q)	5.4 ±0.5	0.06 ±0.02
NDs-Cys (Qx2)	8.6 ±0.5	0.09 ±0.02
NDs-Cys (Qx4)	17.8 ±0.5	0.19 ±0.02

E12. NDs-Cys (Q/4). NDs-Cys (Q/2), NDs-Cys (Q). NDs-Cys (Qx2) and NDs-Cys (Qx4) surface loading estimations.

Synthesis and characterization of 2-hydroxymethypyrrolidin-NDs NDs-Ser (Q, Qx2, Qx4)

In a round bottom flask, 25 mg of NDs were suspended in 5 mL of DMF. Paraformaldehyde (condition Q: 0.42 mmol, 12.5 mg; condition Qx2: 0.83 mmol, 25 mg; condition Qx4: 1.67 mmol, 50 mg) and serine (condition Q: 0.50 mmol, 53 mg; condition Qx2: 1.00 mmol, 106 mg; condition Qx4: 2.00 mmol, 212 mg) were added. The reaction mixture was sonicated for 10', then reacted at 130°C for 2h under magnetic stirring.

After cooling to room temperature, the suspensions were centrifuged (6000 rpm, 8 min) and the supernatant discarded. NDs were subjected to several centrifugation cycles (water, 6000 rpm, 8 min, 3×; methanol, 6000 rpm, 8 min, 3×; dichloromethane, 6000 rpm, 8 min, 3×), then dried at 100°C for 12 h, yielding to NDs-Ser (*Q, Qx2, Qx4*) (MW = 73 g/mol).

Surface loadings estimations are reported (Figure E13).

NDs	**Thermogravimetric analysis**	
	Δm(%)	**Surface loading (mmol/100mg)**
NDs-Ser (Q)	2.6 ±0.5	0.03 ±0.01
NDs-Ser (Qx2)	3.4 ±0.5	0.04 ±0.01
NDs-Ser (Qx4)	4.9 ±0.5	0.06 ±0.01

E13. NDs-Ser (Q), NDs-Ser (Qx2), and NDs-Ser (Qx4) surface loading estimations.

Synthesis and characterization of 2-(4-hydroxyphenyl)-methylpyrrolidin-NDs NDs-Tyr-(Q/2, Q, Qx2, Qx4)

In a round bottom flask, 25 mg of NDs were suspended in 5 mL of DMF. Paraformaldehyde (Q/2: 0.21 mmol, 6.3 mg; condition Q: 0.42 mmol, 12.5 mg; condition Qx2: 0.83 mmol, 25 mg; condition Qx4: 1.67 mmol, 50 mg) and tyrosine (Q/2: 0.25 mmol, 45 mg; condition Q: 0.50 mmol, 91 mg; condition Q2: 1.00

mmol, 182 mg; condition Q4: 2.00 mmol, 364 mg) were added. The reaction mixture was sonicated for 10', then reacted at 130°C for 2h under magnetic stirring.

After cooling to room temperature, the suspension was centrifuged (6000 rpm, 8 min) and the supernatant discarded. NDs were subjected to several centrifugation cycles (water, 6000 rpm, 8 min, 3×; methanol, 6000 rpm, 8 min, 3×; dichloromethane, 6000 rpm, 8 min, 3×), then dried at 100°C for 12 h, yielding to NDs-Tyr *(Q/2, Q, Qx2, Qx4*) (MW = 149.21 g/mol).

Thermogravimetric analysis of NDs-Cys, NDs-Ser, NDs-Tyr

Thermogravigrams derivatives of NDs-Cys, NDs-Ser and NDs-Tyr confirm the different nature of the pyrrolidine adducts on NDs surface, since they present characteristic transition temperatures (Figure E14).

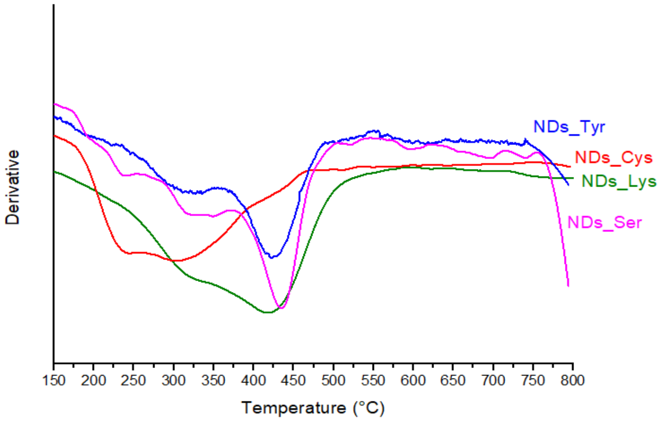

E14. Derivative profiles of thermogravigrams of NDs reacted with paraformaldehyde and cysteine (red), serine (magenta) or tyrosine (blue).

Moreover, derivatives profiles of NDs-Tyr synthetised in different reagents concentrations conditions suggest the presence of different polymeric-like adducts on NDs (Figure E15).

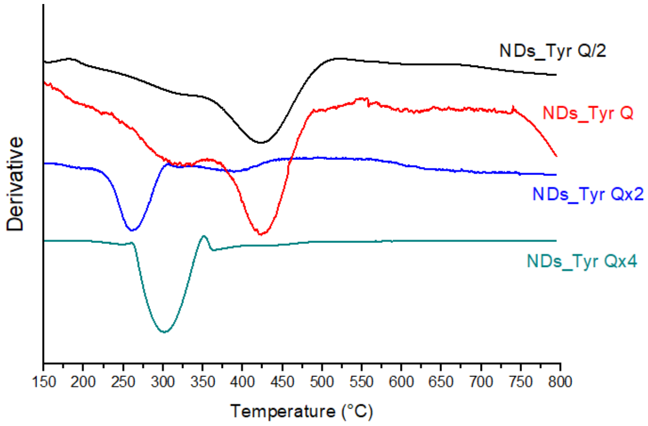

E15. Derivative profiles of NDs-Tyr (Q/2), NDs-Tyr (Q), NDs-Tyr (Qx2), NDs-Tyr (Qx4) thermogravigrams.

Surface loadings estimations (Figure E16) are reported.

NDs	Thermogravimetric analysis	
	Δm(%)	Surface loading (mmol/100mg)
NDs-Tyr (Q/2)	1.8 ±0.5	0.01 ±0.01
NDs-Tyr (Q)	2.5 ±0.5	0.01 ±0.01
NDs-Tyr (Qx2)	10.3 ±0.5	0.06 ±0.01
NDs-Tyr (Qx4)	46.5 ±0.5	0.31 ±0.01

E16. NDs-Tyr (Q/2), NDs-Tyr (Q), NDs-Tyr (Qx2), and NDs-Tyr (Qx4) surface loading estimations.

Synthesis of 6-((((9H-fluoren-9-yl)methoxy)carbonyl)amino)hexanoic acid (e)

In a round bottom flask, a solution of 1.57 g (4.67 mmol) of Fmoc N-hydroxy succinimide ester in 33 mL of 1,4-dioxane was added to a solution of 557 mg (4.25 mmol) of 6-aminohexanoic acid in 33 mL of $NaHCO_3$ saturated water. The reaction mixture was allowed to react at room temperature for 16 hours under magnetic stirring. Then, the solvent was removed under reduced pressure, the residue was dissolved in 10 mL of HCl 1M, extracted with ethyl acetate (3x20mL) and washed with brine. The organic phases were combined, dried over sodium sulphate and subsequently the solvent was removed. A white solid is recovered (1.656 g, 4.69 mmol, 94% yield).

MS ESI+: calculated for $C_{21}H_{23}NO_4$ 354.42, found $[M+H]^+$= 354.01 , $[M+Na]^+$= 376.03.

^{1}H NMR (600 MHz, MeOD): δ = 7.766 (d, J = 7.2 Hz, 2H, 14), 7.632 (d, J = 7.2 Hz, 2H, 11), 7.367 (t, J = 7.2 Hz, 2H, 13), 7.288 (t, J = 7.2 Hz, 2H, 12), 4.330 (d, J = 6.6 Hz, 2H, 8), 4.170 (m, 1H, 9), 3.079 (t, J = 6.6 Hz, 2H, 6), 2.274 (t, J = 7.2 Hz, 2H, 2), 1.598 (m, 2H, 5), 1.480 (m, 2H, 4), 1.328 (m, 2H, 3).

^{13}C NMR (600 MHz, MeOD): δ = 177.532 (1), 158.890 (7), 145.351 (15), 142.603 (10), 128.739 (14), 128.116 (11), 126.154 (13), 120.907 (12), 67.508 (8), 41.551 (9), 34.829 (6), 30.559 (2), 27.332 (5), 26.269 (4), 25.743 (3).

Synthesis of (9H-fluoren-9-yl)-methyl-(6-chloro-6-oxohexyl)-carbamate (f)

In a round bottom flask, 700 mg (2.0 mmol) of 6-((((9H-fluoren-9-yl)methoxy)carbonyl)amino hexanoic acid were solubilized in 3.5 mL of dichloromethane, then 1 mL of thionyl chloride (1.630 g, 13.7 mmol) were dropped. The mixture was allowed to react for 0.5 hours at room temperature, under magnetic stirring. The solvent was removed under reduced pressure and the residue was washed five times with dichloromethane. An orange viscous oil was recovered (730 mg, 1.96 mmol, 96% yield).

MS ESI+: calculated for $C_{21}H_{22}ClNO_3$ 371.86, found $[M+H]^+$= 368.09 (as methyl ester).

^{1}H NMR (600 MHz, $CDCl_3$): δ = 7.775 (d, *J* = 7.2 Hz, 2H, *14*), 7.583 (d, *J* = 7.2 Hz, 2H, *11*), 7.405 (t, *J* = 7.2 Hz, 2H, *13*), 7.331 (t, *J* = 7.2 Hz, 2H, *12*), 4.761 (s, 1H, *16*), 4.411 (m, 2H, *8*), 4.215 (m, 1H, *9*), 3.198 (m, 2H, *6*), 2.897 (t, *J* = 6.6 Hz, 2H, *2*), 1.729 (m, 2H, *3*), 1.529 (m, 2H, *5*), 1.377 (m, 2H, *4*).

^{13}C NMR (600 MHz, $CDCl_3$): δ = 173.753 (*1*), 156.404 (*7*), 143.985 (*15*), 141.295 (*10*), 127.651 (*14*), 126.999 (*11*), 124.970 (*13*), 119.952 (*12*), 66.468 (*8*), 47.251 (*9*), 46.887 (*2*), 40.597 (*6*), 29.519 (*5*), 25.469 (*3*), 24.626 (*4*).

NDs-NH_2 functionalization with (9H-fluoren-9-yl)methyl(6-chloro-6-oxohexyl) carbamate (21)

Electrophile equivalents are calculated with respect to the free amount of aminobutyl chain on NDs-Lys (Q), estimated from TGA.
In a solution of (9H-fluoren-9-yl)-methyl-(6-chloro-6-oxohexyl)-carbamate (2.0 eq, 0.032 mmol, 11.8 mg) and DIPEA (5.0 eq, 0.0795 mmol, 10.2 mg) in 1 mL of dichloromethane, 30 mg of NDs-Lys (Q) (condition Q, 0.0159 mmol, 1 eq) were added. After 10’ sonication, the suspension was allowed to react at room temperature for 6 hours, under magnetic stirring. The suspension was centrifuged (6000 rpm, 8 min) and the supernatant discarded. NDs were subjected to several centrifugation cycles (methanol, 6000 rpm, 8 min, 3×; water, 6000 rpm, 8 min, 3×; methanol, 6000 rpm, 8 min, 3×; dichloromethane, 6000 rpm, 8 min, 3×), then dried at 100°C for 12 h, yielding to NDs-(21).

NDs-SH functionalization with N-ethyl maleimide (22)

Electrophile equivalents are calculated with respect to the free amount of mercaptomethyl chain on NDs-Cys (Q/4), estimated from TGA.
To a suspension of 20 mg of NDs-Cys (Q/4) (0.00620 mmol, 1 equivalent) in 0.5 mL of MeOH, *N*-ethyl maleimide (10 eq, 0.0620 mmol, 8.0 mg) is added. The reaction mixture was sonicated for 10’, then was allowed to react under magnetic stirring for 24 hours at room temperature. The suspension was centrifuged (6000 rpm, 8 min) and the supernatant discarded. NDs were subjected to several centrifugation cycles (methanol, 6000 rpm, 8 min, 4×; dichloromethane, 6000 rpm, 8 min, 3×), then dried at 100°C for 12 h, yielding to NDs-(22).

Thermogravimetric analysis of (21) and (22)

Nanosystems (21) and (22) were analysed by thermogravimetry (Figure E17).

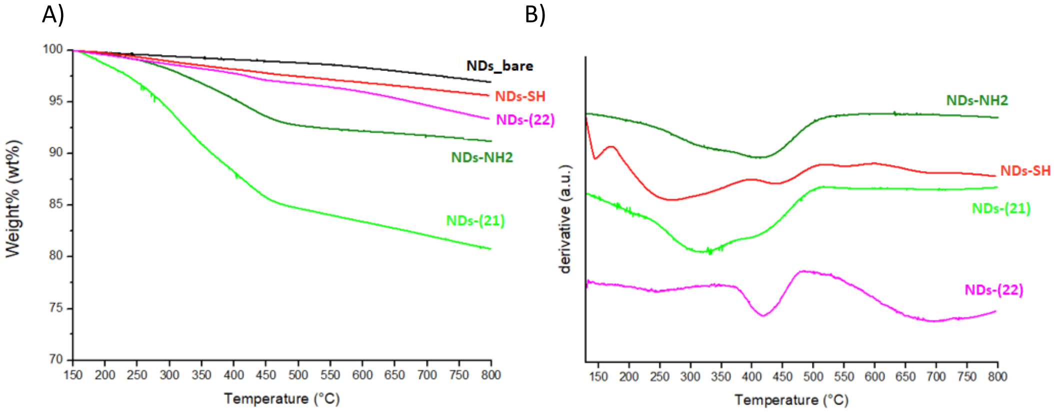

E17. Thermogravigrams (A) and relative derivative profiles (B) of NDs-(21) (light green), NDs-(22) (magenta), NDs-SH (compound NDs-Cys (Q/4), red) and NDs-NH_2 (compound NDs-Lys (Q), green).

Surface loadings were estimated from weight % loss, with respect to bare NDs (Figure E18).

NDs	Thermogravimetric analysis	
	Δm(%)	Surface loading (mmol/100mg)
NDs-Lys (Q)	6.0 ±0.5	0.05 ±0.02
NDs-(21)	15.3 ±0.5	0.02 ±0.01
NDs-Cys (Q/4)	1.4 ±0.5	0.02 ±0.01
ND-(22)	2.7 ±0.5	0.02 ±0.01

E18. NDs-Lys (Q), ND-(21), NDs-Cys (Q/4) and NDs-(22) surface loading estimations.

Surface loadings, expressed in mmol of adduct / 100 mg NDs are calculated from nanosystems thermogravimetric weight loss % at 650°C profiles, considering adduct MW:

NDs-Lys (Q) : 114 mol/g, weight loss 6.0%;
NDs-(21): 336.42 mol/g, weight loss 15.3-6.0 = 9.3% (referred to the electrophile component);
NDs-Cys (Q/4) : 89 mol/g, weight loss 1.4%;
NDs-(22): 126.14 mol/g, weight loss 2.7-1.4 = 1.3% (referred to the electrophile component).

Electrophile surface loading is expressed as mmol of electrophile / 100 mg bare NDs, taking in to account the weight loss caused by pyrrolidine cycloaddition adduct.
Electrophile conjugation yield is calculated as mmol electrophile / 100 mg bare NDs and mmol pyrrolidine adducts / 100 mg bare NDs ratio.
Conjugation yields:

NDs-(21): 0.027/0.0529 = 52%
NDs-(22): 0.005/0.016 = 31%

NDs functionalization with lysine and cysteine (23) and characterization

To a suspension of 25 mg of NDs-NH_2 (condition Q/2) in 2.5 mL of DMF, paraformaldehyde (condition Q: 0.42 mmol, 12.5 mg) and cysteine (condition Q: 0.50 mmol, 61 mg) were added. The reaction mixture was sonicated for 10' and allowed to react for 2 hours at 130°C under magnetic stirring. After cooling to room temperature, the suspensions were centrifuged (6000 rpm, 8 min) and the supernatant discarded. NDs were subjected to several centrifugation cycles (water, 6000 rpm, 8 min, 3×; methanol, 6000 rpm, 8 min, 3×; dichloromethane, 6000 rpm, 8 min, 3×), then dried at 100°C for 12 h, yielding to NDs-NH_2-SH (23).

Surface loadings were estimated from weight % loss, with respect to bare NDs (Figure E19).

NDs	**Thermogravimetric analysis**	
	Δm(%)	**Surface loading (mmol/100mg)**
NDs-Lys (Q/2)	2.8 ±0.5	0.02 ±0.02
NDs-(23)	8.9 ±0.5	0.06 ±0.01

E19. NDs-Lys (Q/2) and (23) surface loading estimations.

Surface loadings, expressed in mmol of adduct / 100 mg NDs were calculated from nanosystems thermogravimetric weight loss % at 650°C profiles, considering adduct MW:

NDs-Lys (Q/2) : 114 mol/g, weight loss 2.8%;
NDs-(23): 89 mol/g, weight loss 8.9-2.8 = 6.1% (referred to 2-mercaptomethyl pyrrolidine adduct)

5.6 Synthetic procedures for NDs-Cetuximab nanosystems

Synthesis of 3-(2,5-dioxo-2,5-dihydro-1H-pyrrol-1-yl)propionyl chloride (g)

To a 4 mL solution of 3-(maleimido)propionic acid (100 mg, 0.60mmol) in dichloromethane, thionyl chloride (0.5 mL) was slowly added. The reaction mixture was stirred at reflux, overnight, under nitrogen atmosphere. Dichloromethane and thionyl chloride were evaporated under reduced pressure and the residue was washed with dichloromethane (5x6mL). A pale oil was obtained (110 mg, 0.57 mmol, 97% yield).
MS-ESI+: calculated for $C_7H_6ClNO_3$ 187.58.
^{1}H NMR (600 MHz, $CDCl_3$): δ = 6.737 (s, 1H, *5*), 3.868 (t, *J* = 6.6 Hz, 2H, *2*), 3.251 (t, *J* = 6.6 Hz, 2H, *3*).
^{13}C NMR (600 MHz, $CDCl_3$): δ = 171.529 (*1*), 170.102 (*4*), 134.484 (*5*), 44.989 (*3*), 33.212 (*2*).

Synthesis of tert-butyl (2-(2-(2-(3-(2,5-dioxo-2,5-dihydro-1H-pyrrol-1-yl)propanamido)ethoxy) ethoxy)ethyl)carbamate (h)

A 2 mL dichloromethane solution of compound (g) (100 mg, 0.533 mmol) was slowly added to a 3.5 mL dichloromethane solution of compound (b) (120 mg, 0.484 mmol) and DIPEA (63 mg, 83 µL, 0.484 mmol). The mixture was reacted at room temperature, overnight, under magnetic stirring. The organic layer was washed with HCl 0.1N (3x5mL), then evaporated under reduced pressure, leading to a pale-yellow oil (168 mg, 0.42 mmol, 87% yield).

MS-ESI+: calculated for $C_{18}H_{29}N_3O_7$ 399.44, found $[M+H]^+$=400.01, $[M+Na]^+$=422.98

^{1}H NMR (600 MHz, $CDCl_3$): δ = 6.696 (s, 2H, *14*), 5.019 (bs, 1H, *8*), 3.844 (t, *J* = 7.8 Hz, 2H, *12*), 3.605 (m, 4H, *5,6*), 3.565 (m, 2H, *8*), 3.532 (t, *J* = 4.8 Hz, 2H, *7*), 3.428 (m, 2H*, 4*), 3.332 (m, 2H, *3*), 2.523 (t, *J* = 7.2 Hz, 2H, *11*), 1.436 (s, 9H, *1*).

^{13}C NMR (600 MHz, $CDCl_3$): δ = 170.529 (*13*), 165.723 (*10*), 156.138 (*2*), 134.231 (*14*), 70.406 (*5*), 70.310 (*6*), 70.138 (*7*), 69.755 (*4*), 53.468 (*12*), 44.458 (8), 39.068 (*3*), 33.476 (*11*), 28.382 (*1*).

Synthesis of N-(2-(2-(2-aminoethoxy)ethoxy)ethyl)-3-(2,5-dioxo-2,5-dihydro-1H-pyrrol-1-yl)propenamide (i)

Compound (h) (160 mg, 0.40 mmol) is solubilized in 7 mL of dichloromethane; 1 mL of trifluoroacetic acid was slowly added. The suspension was allowed to react at room temperature for 1 hour, under magnetic stirring. The solvent was evaporated under reduced pressure. A pale-yellow viscous oil was obtained (160 mg, 0.39 mmol, 97% yield).

MS-ESI+: calculated for $C_{13}H_{21}N_3O_5$ 299.33, found $[M+H]^+$=300.12.

^{1}H NMR (600 MHz, $CDCl_3$): δ = 6.705 (s, 2H, *14*), 5.300 (bs, 2H, *8*), 4.170 (bs, 2H, *2*), 3.793 (t, *J* = 7.8 Hz, 2H, *12*), 3.694 (m, 4H, *5,6*), 3.604 (m, 2H, *8*), 3.578 (t, *J* = 4.8 Hz, 2H, *7*), 3.437 (m, 2H*, 4*), 3.298 (m, 2H, *3*), 2.584 (t, *J* = 7.2 Hz, 2H, *11*).

^{13}C NMR (600 MHz, MeOD): δ = 172.352 (*13*), 171.270 (*10*), 134.627 (*14*), 70.505 (*5*), 70.390 (*6*), 69.682 (*7*), 67.010 (*4*), 39.818 (*12*), 39.320 (8), 34.810 (*3*), 33.532 (*11*).

Synthesis of Cetuximab-SH system (l)

23 µL of gamma thiobutyrolactone (27 mg, 0.265 mmol) and 50 µL of ethylene glycol were solubilized in 930 µL of PBS. 10 µL of this solution were added to 500 µL of a 5 mg/mL solution of Cetuximab (2.5 mg, 17.1 nmol) and the solution was stirred at room temperature for 2 hours. The desired thiolated Cetuximab (l) was purified by gel filtration on a PD-10 Desalting Column, according to standard procedure. 17 nmol of (l) were eluted with 3.5 mL PBS buffer.

Synthesis of NDs-COOH (16)

In a round bottom flask, 100 mg of 50 nm annealed NDs were suspended in 10 mL of sulfonitric mixture (nitric acid: sulfuric acid 1:3) and stirred overnight at reflux. The suspension was centrifuged (6000 rpm, 8 min) and the supernatant was discarded. NDs were suspended in 10 mL NaOH 1M and reacted for 3 hours at reflux under magnetic stirring. The suspension was centrifuged (6000 rpm, 8 min) and the supernatant was discarded. Then NDs were suspended in 10 mL HCl 1M and reacted for 3 hours at reflux under magnetic stirring. The suspension was centrifuged (6000 rpm, 8 min) and the supernatant was discarded. NDs were subjected to several centrifugation cycles (water, 6000 rpm, 8 min, 5×; methanol, 6000 rpm, 8 min, 3×; dichloromethane, 6000 rpm, 8 min, 3×), then dried at 100°C for 12 h.

Characterization of NDs-COOH (16)

In order to estimate surface carboxylic groups amount, NDs-COOH were analysed by thermogravimetry (Figure E20). It was assumed that the weight loss % of NDs-COOH measured at 650°C, was ascribable to CO_2 (MW=44 g/mol) released from surface carboxylic groups.

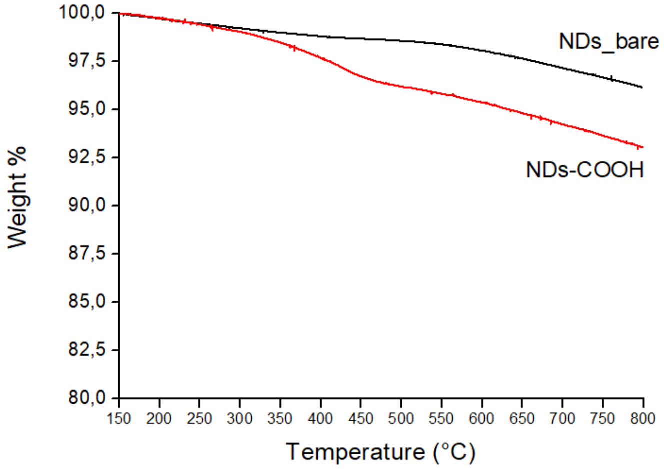

E20. Thermogravigrams of NDs-COOH. Weight loss % is ascribable to CO_2 released from surface carboxylic groups.

Weight loss % (with respect to NDs_bare): 2.9%

COOH surface amount (mmol/100mg NDs): 2.9mg/44mg*mmol/100mg = 0.066mmol /100mg

Synthesis of NDs-COCl (24)

80 mg of NDs-COOH (16) were suspended in 4 mL of freshly distilled thionyl chloride and reacted at 70°C overnight, in nitrogen atmosphere under magnetic stirring. The suspension was centrifuged (6000 rpm, 8 min) and the supernatant was discarded. NDs were subjected to several centrifugation cycles (dichloromethane, 6000 rpm, 8 min, 6×), then stocked under nitrogen atmosphere.

From NDs-COOH (16) characterization, a COCl surface amount of 0.066 mmol/100mg is assumed.

Synthesis of NDs-Linker (25)

To a suspension of 35 mg of NDs-COCl (24) and 108 µL of DIPEA (0.98 mmol, 4.4 eq) in 2 mL of dichloromethane, a solution of 100 mg of compound (i) (0.242

mmol, 1.1 eq with respect to previously calculated COCl) in 3 mL of dichloromethane were slowly added. The reaction mixture was allowed to stir at room temperature over night. The suspension was centrifuged (6000 rpm, 8 min) and the supernatant was discarded. NDs were subjected to several centrifugation cycles (dichloromethane, 6000 rpm, 8 min, 6×).

Synthesis of NDs-Cetuximab nanosystem NDs-Ctx (26)

In 3.5 mL of (I) (17 nmol), 16 mg of NDs-linker (25) (3.36 µL of linker) were suspended. The mixture was allowed to stir for 4 hours at room temperature. The suspension was centrifuged (6000 rpm, 3 min) and the supernatant was discarded. NDs were subjected to several centrifugation cycles (PBS, 6000 rpm, 3 min, 3×).

5.7 Characterization of NDs-Cetuximab nanosystems

NDs-linker (25) and NDs-Cetuximab nanosystems (26) thermogravimetric derivative profiles show thermal transitions of the respective adducts (**Figure E21**)

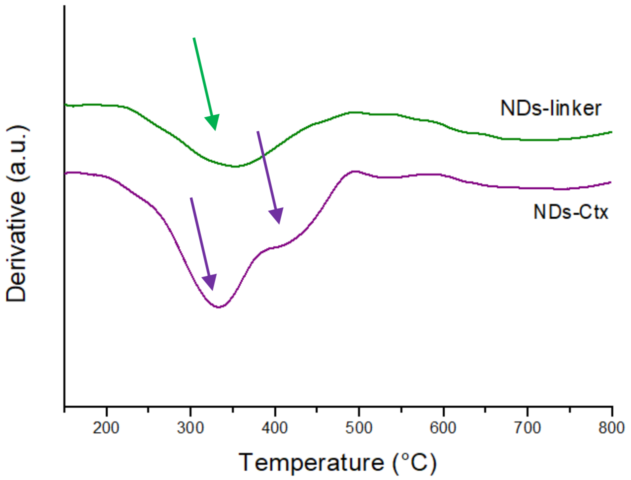

E21. Derivatives of NDs-linker (green line) and NDs-Cetuximab (purple line) nanosystems thermogravigrams, showing typical thermal transitions (arrows).

NDs-Cetuximab (26) nanosystems surface loadings were then estimated (see Figure E22), starting from thermogravimetric analysis (see Figure E23).

NDs	**Thermogravimetric analysis**	
	Δm(%)	**Surface loading (μmol/100mg)**
NDs-linker (25)	6.3 ±0.5	21 ±2
ND-Cetuximab (26)	13.9 ±0.5	0.11 ±0.04

E22. NDs-linker (25) and NDs-Cetuximab (26) surface loading estimations.

Surface loadings, expressed in μmol of adduct / 100 mg NDs were calculated from nanosystems thermogravimetric weight loss % at 650°C profiles, considering adduct MW:

(25): 326.31 g/mol, weight loss 6.3%;
(26): 146000 g/mol, weight loss 13.9-6.3 = 7.6% (referred to the Cetuximab component).
Cetuximab surface loading is expressed as nmol of Cetuximab / 100 mg bare NDs, taking in to account the weight loss caused by the previously grafted linker.

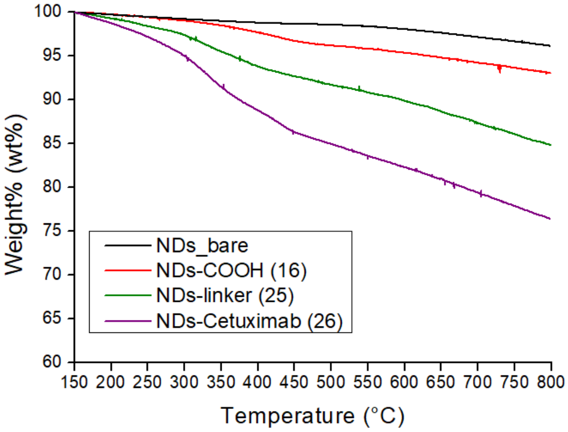

E23. Thermogravimetric profile of NDs-Cetuximab (26) (purple line), NDs-linker (25) (green line) nanosystems. Starting materials NDs_bare (black line) and oxidized NDs-COOH (16) (red line) are reported as well.

5.8 NDs-Cetuximab nanosystems *in vitro* test

HT29 colon-rectal cancer cell line was put on 12 mm round slides in ethanol for 2 hours. Slides then were put in 24 well plate and ethanol was evaporated. Cells were stained with DiFi (30000 in 200 nL) and growth overnight at 37°C.

The plate was washed with PBS 1X and cells were incubated with bare 50 nm NDs in Ham's F12 w/ L- Glutamine pH 7.4 (AUROGENE) (50% without anything, 50% complete), 250 μL for 24 hours.

The plate was washed 2 times with PBS 1X, incubated for 30' with 230 μL medium containing green fluorescent chloromethyl derivatives of fluorescein diacetate (CMFDA) 0.5 μM per well, then washed with PBS 1X. Cells were then stimulated with NDs (bare: 1.54 mg in 337 μL PBS, NDs-linker (25): 2.62 mg in 536 μL PBS, NDs-Cetuximab (26) 16 mg in 3.5 mL PBS), then washed with PBS 1X and observed at confocal microscope.

5.9 NDs surface tunability via carboxylic/graphitic component

5.9.1 Lysine-derived azomethine ylides cycloaddition on NDs

Cycloaddition reaction on NDs (11)-(A, B, C, D)

In a round bottom flask, 50 mg of NDs were suspended in 10 mL of DMF. Paraformaldehyde (0.83 mmol, 25 mg) and lysine (1.00 mmol, 146 mg) then were added. The reaction mixtures were sonicated for 10’, then reacted at 130°C for 2h under magnetic stirring.
After cooling to room temperature, the suspensions were centrifuged (6000 rpm, 8 min) and the supernatant discarded. NDs were subjected to several centrifugation cycles (water, 6000 rpm, 8 min, 3×; methanol, 6000 rpm, 8 min, 3×; dichloromethane, 6000 rpm, 8 min, 3×), then dried at 100°C for 12 h, yielding to NDs-NH_2.

Thermogravimetric analysis and quantification

Surface loading was calculated from weight % loss estimated via thermogravimetry at 650°C, taking in to account the molecular weight of the cycloaddition adduct (see Figure E24).

NDs	Post-annealing treatment	Thermogravimetric analysis	
		Δm(%)	**Surface loading (mmol/100mg)**
NDs-(11)-A	-	6.7 ±0.5	0.06 ±0.02
NDs-(11)-B	**O_2, 400°C, 30'**	6.9 ±0.5	0.06 ±0.02
NDs-(11)-C	**O_2, 500°C, 1h**	6.3 ±0.5	0.05 ±0.02
NDs-(11)-D	**H_2SO_4 /HNO_3**	4.3 ±0.5	0.03 ±0.02

E24. Thermogravimetric weight loss percent and surface amount estimation of oxidized NDs (11)-(A,B,C,D) subjected to 1,3-dipolar cycloaddition reaction.

5.9.2 Condensation reactions on NDs

NDs functionalization with tert-butyl (2-(2-(2-aminoethoxy)ethoxy)ethyl) carbamate (27)-(A, B, C, D)

To a solution of *tert*-butyl (2-(2-(2-aminoethoxy) ethoxy) ethyl) carbamate (1 eq, 0.2 mmol, 50 mg), HBTU (4 eq, 0.8 mmol, 303 mg) and DIPEA (10 eq, 2.0 mmol, of 256 mg) in 2 mL of DMF 20 mg was selected NDs were added. The suspension was sonicated for 10’, then was allowed to react under magnetic stirring overnight at 60°C. The suspension was centrifuged (6000 rpm, 8 min) and the supernatant was discarded. NDs were subjected to several centrifugation cycles (DMF, 6000 rpm, 8 min, 3×; water, 6000 rpm, 8 min, 3×; methanol, 6000 rpm, 8 min, 3×; dichloromethane, 6000 rpm, 8 min, 3×), then dried at 100°C for 12 h.

Thermogravimetric analysis and quantification

Surface loading was calculated from weight % loss estimated via thermogravimetry at 650°C, taking in to account the molecular weight of the cycloaddition adduct (see Figure E25).

NDs	Post-annealing treatment	Thermogravimetric analysis	
		Δm(%)	**Surface loading (mmol/100mg)**
NDs-(27)-A	-	1.4 ±0.5	0.005 ±0.004
NDs-(27)-B	**O_2, 400°C, 30'**	1.5 ±0.5	0.006 ±0.004
NDs-(27)-C	**O_2, 500°C, 1h**	1.7 ±0.5	0.006 ±0.004
NDs-(27)-D	**H_2SO_4 /HNO_3**	2.7 ±0.5	0.011 ±0.004

E25. Thermogravimetric weight loss percent and surface amount estimation of oxidized NDs (27)-(A,B,C,D) subjected to 1,3-dipolar cycloaddition reaction.

5.10 Synthesis of highly fluorescent NDs

5.10.1 Ionic implantation

The process was carried out at the AN2000 accelerator of the INFN national laboratories in Legnaro. The samples were prepared by depositing a thin layer of nanodiamonds on small silicon wafers with approximately 1x1 cm^2 area. The layer thickness was (33 ± 10) µm, estimated by optical microscope images (see Figure E26). The error was indicative of the variability on the single deposition. A 2 MeV proton beam was accelerated, collimated to homogeneously cover a 5×5 mm^2 spot. The current was set between 400-500 nA and the irradiation time 7 minutes, reaching an implantation fluence of 5×10^{15} cm^{-2}.

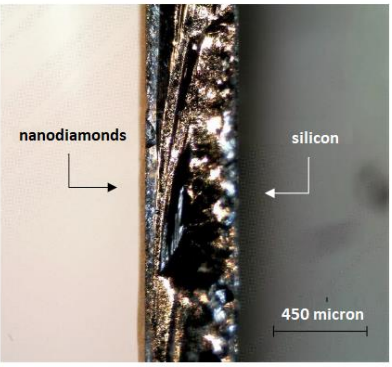

E26. Optical microscope image of the silicon wafer profile with the deposited thin layer of nanodiamonds indicated by arrows.

5.10.2 Synthesis of N-enriched graphite

Synthesis of High N-graphite (28)

1.102 g of graphite were suspended in a solution of 0.550 g of paraformaldehyde (18.3 mmol, 1 eq) and 1.650 g of glycine (22.0 mmol, 1.2 eq) in 20 mL of DMF. The suspension was allowed to react for 2h at 130°C under magnetic stirring. After cooling to room temperature, the reaction mixture was centrifuged (4000 rpm, 8 min) and the supernatant was discarded. The graphite was subjected to several centrifugation cycles (water, 4000 rpm, 8 min, 3x; water/dioxane 1:1, 4000 rpm, 8 min, 3x; dioxane, 4000 rpm, 8 min, 3x). Drying at 70°C for 24 h yielded the functionalized graphite, ready for thermogravimetric analysis.

Synthesis of Low N-graphite (29)

1.010 g of graphite were suspended in a solution of 2.52 g of *p*-nitrobenzaldehyde (16.7 mmol, 1 eq) and 3.080 g of histidine (20.0 mmol, 1.2 eq) in 45 mL of DMF. The suspension was allowed to react for 2h at 130°C under magnetic stirring. After cooling to room temperature, the reaction mixture was centrifuged (4000 rpm, 8 min) and the supernatant was discarded. The graphite was subjected to several centrifugation cycles (methanol, 4000 rpm, 8 min, 3x; methanol/dichloromethane 1:1, 4000 rpm, 8 min, 3x; dichloromethane, 4000 rpm, 8 min, 3x). Drying at 70°C for 24 h yielded the functionalized graphite, ready for thermogravimetric analysis.

5.11 Characterization of N-enriched graphite

Graphite nitrogen amount was calculated from weight % loss estimated via thermogravimetry at 650°C, taking in to account the molecular weight of the cycloaddition adduct.

High-N graphite

Adduct MW: 43.00 g/mol
TG weight loss%: 7.1
mmol adduct /1g of graphite: 7.13mg /100mg*10/43.00g*mol = 1.6 mmol/1g
mmol nitrogen /1g of graphite: mmol adduct/1g of graphite*1 = 1.6 mmol/1g
nitrogen atoms /1g of graphite: 1.66 mmol/1g *6.022*10^{23}=9.9*10^{20} atoms/1g
mg nitrogen / 1g of graphite: 1.66 mmol/1g*14.01 = 23.2 mg/g

Low-N graphite

Adduct MW: 244.27 g/mol
TG weight loss%: 2.5
mmol adduct / 1g of graphite: 2.54mg /100mg*10/244.27*mol = 0.1 mmol/1g
mmol nitrogen /1g of graphite: mmol adduct/1g of graphite*4 = 0.4 mmol/1g
nitrogen atoms /1g of graphite: 0.416 mmol/1g $*6.022*10^{23}=2.5*10^{20}$ atoms/1g
mg nitrogen / 1g of graphite: 0.416 mmol/1g*14.01 = 5.8 mg/g

6. CONCLUSION

NDs are promising carbon-based nanomaterials for many applications. This nanomaterial plays a central role in all biomedical fields, in particular in therapy as drug delivery systems and in diagnosis, as sensing tools. Their surface constitutes an important hooking point for many molecules of interest, from antibodies to porphyrins, to paramagnetic species.

The graphitic component of ND surface can undergo cycloaddition reactions, of which 1,3-dipolar with azomethine ylides generated by amino acids has proved to be more effective, predictable and tunable than Diels-Alder. These features can be exploited when a large, or precise amount of surface molecules are required to obtain hybrid NDs.

On the other hand, partial removal of graphitic surface by oxidation makes NDs more fluorescent and allows the introduction of derivatizable carboxylic groups. Although NDs grafting performed by carboxylic surface exploitation is less efficient than the graphitic one, it has been shown that it is actually modulable, according to oxidative pre-treatment aggressiveness. Taking advantage of this strategy, covalent NDs derivatization with Cetuximab has allowed to produce an efficient targeting system for optical imaging and, maybe in the future, for targeted drug delivery.

It is important to highlight that the surface plays also an active role in the modulation of fluorescence, and then directly affects all those fields in which fluorescence is involved. On the other hand, fluorescence strictly depends on NV center density, which can be increased by ion implantation technique on already prepared NDs, or by generating NV center since from ND inception by laser ablation of N-enriched graphite. The latter can be prepared exploiting the reliability and tunability of the 1,3-dipolar cycloaddition of azomethine ylides on commonplace graphite.

Fluorescence, paramagnetic behaviour and therapy are intimately connected to each other and must all be equally taken into consideration in order to tailor this interesting nanomaterials for theranostics applications, without forgetting the relevant role that the ND surface plays both in derivatization processes and on fluorescence modulation.

7. OUTLOOK

The effective, predictable and tunable covalent functionalization of NDs is an intriguing topic, as it would extend NDs applications in different fields. In this work it has been shown that both the graphitic and carboxylic surface are functionalizable in a reliable manner. In particular, the use of amino acids in 1,3-dipolar cycloaddition via azomethine ylides allows to decorate NDs graphitic surface with different heteroatoms, even on the same nanodiamond. Further derivatization studies could be conducted on nanodiamonds, in order to introduce different molecules of interest on the same nanosystem. Moreover, deeper investigations should be carried out on the 1,3-dipolar cycloaddition strategy varying aldehydes and amino acids, as well as reaction cycles, allowing the production of versatile nanosystems. Given the possibility to combine several active species, NDs would be very useful in therapeutic treatments, where synergistic effects of several drugs are often required. Similar approach could help to better understand the dipolar interactions between nanodiamonds and paramagnetic species, giving the fundamental knowledge to better tailor them for sensing applications. The possibility to conjugate antibodies on the surface of highly fluorescent NDs makes possible to realise very efficient nanosensors with high selectivity towards specific cellular epitopes.

Of course, the in vivo applications of these highly technological hybrid materials requires their sufficient suspendability in aqueous media; thus surface functional groups, introduced by the aforementioned methods, can be exploited to graft hydrophilic moieties which can reduce aggregation and favour suspension stability.

SUPPLEMENTARY INFORMATION

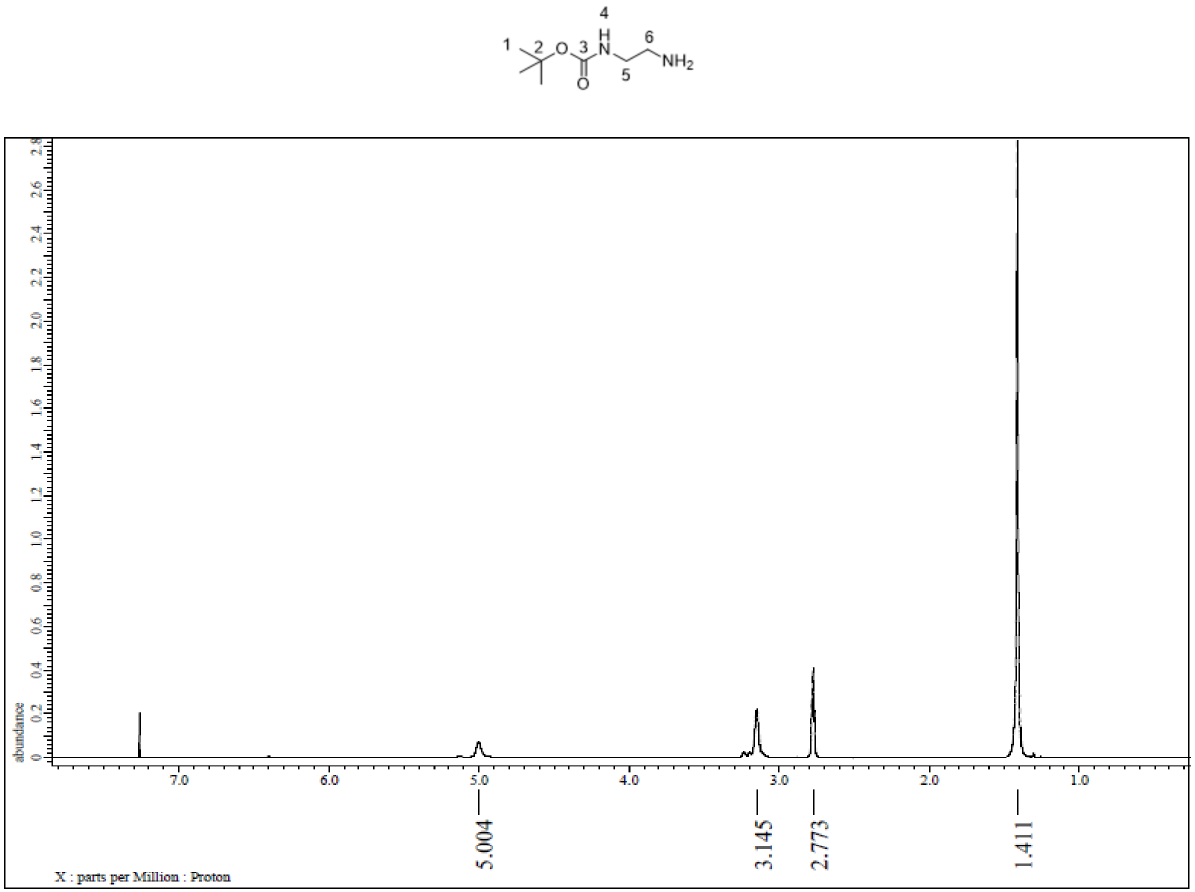

S1. ^{1}H NMR spectrum of compound (a).

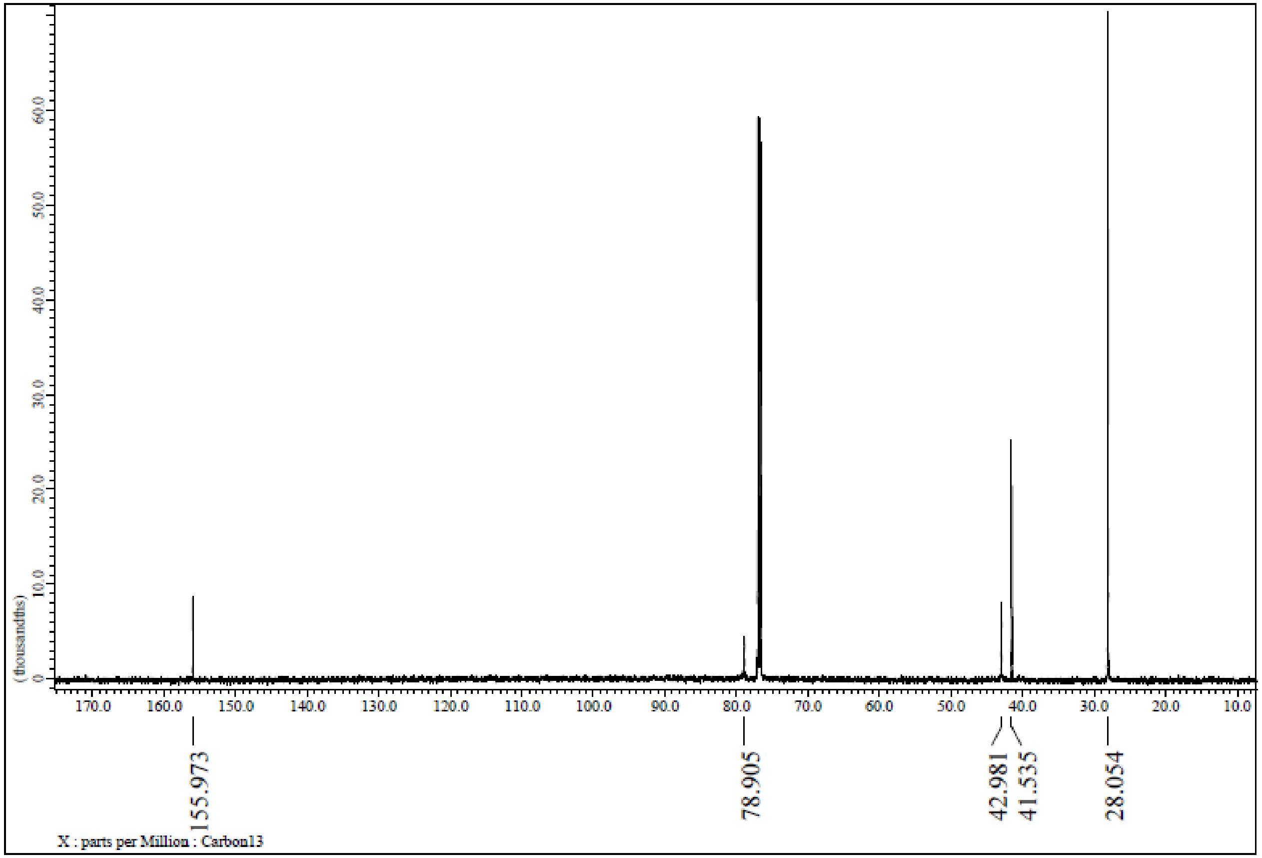

S2. ^{13}C NMR spectrum of compound (a).

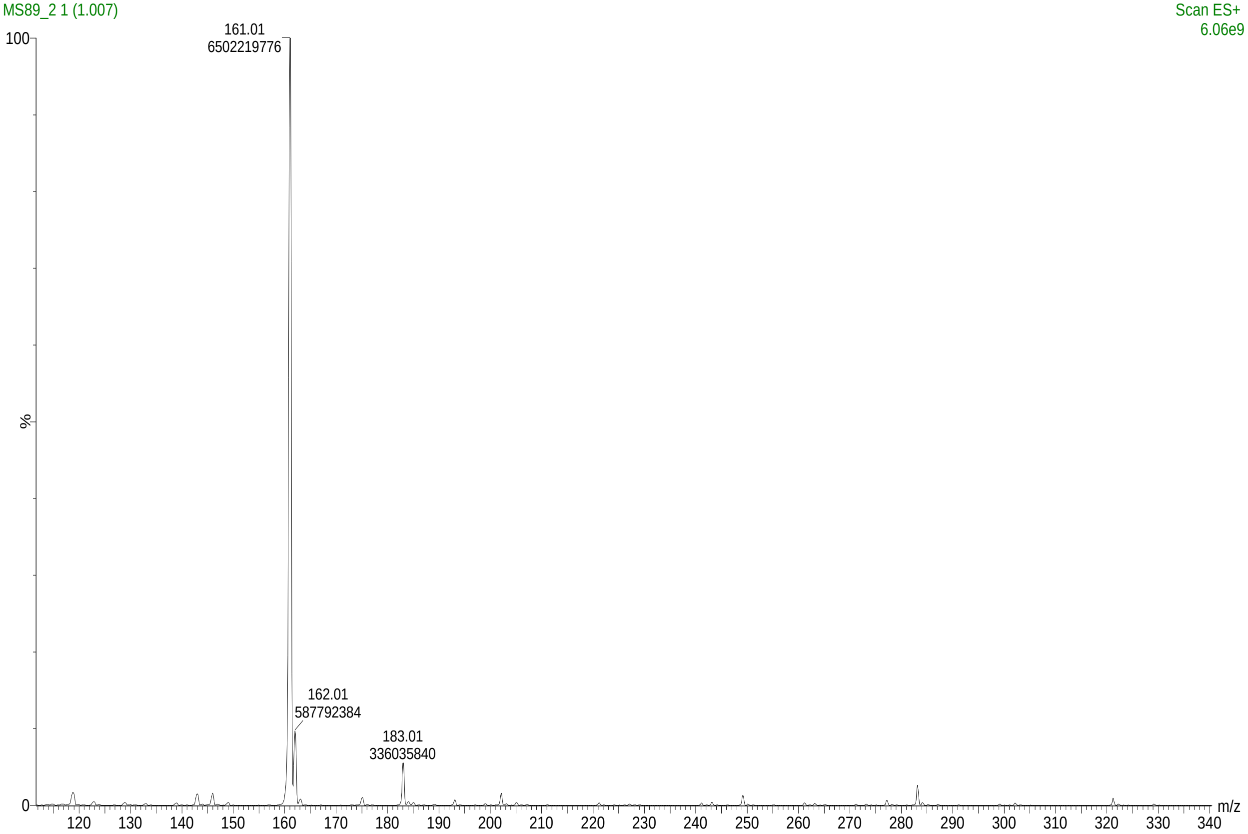

S3. MS spectrum of compound (a).

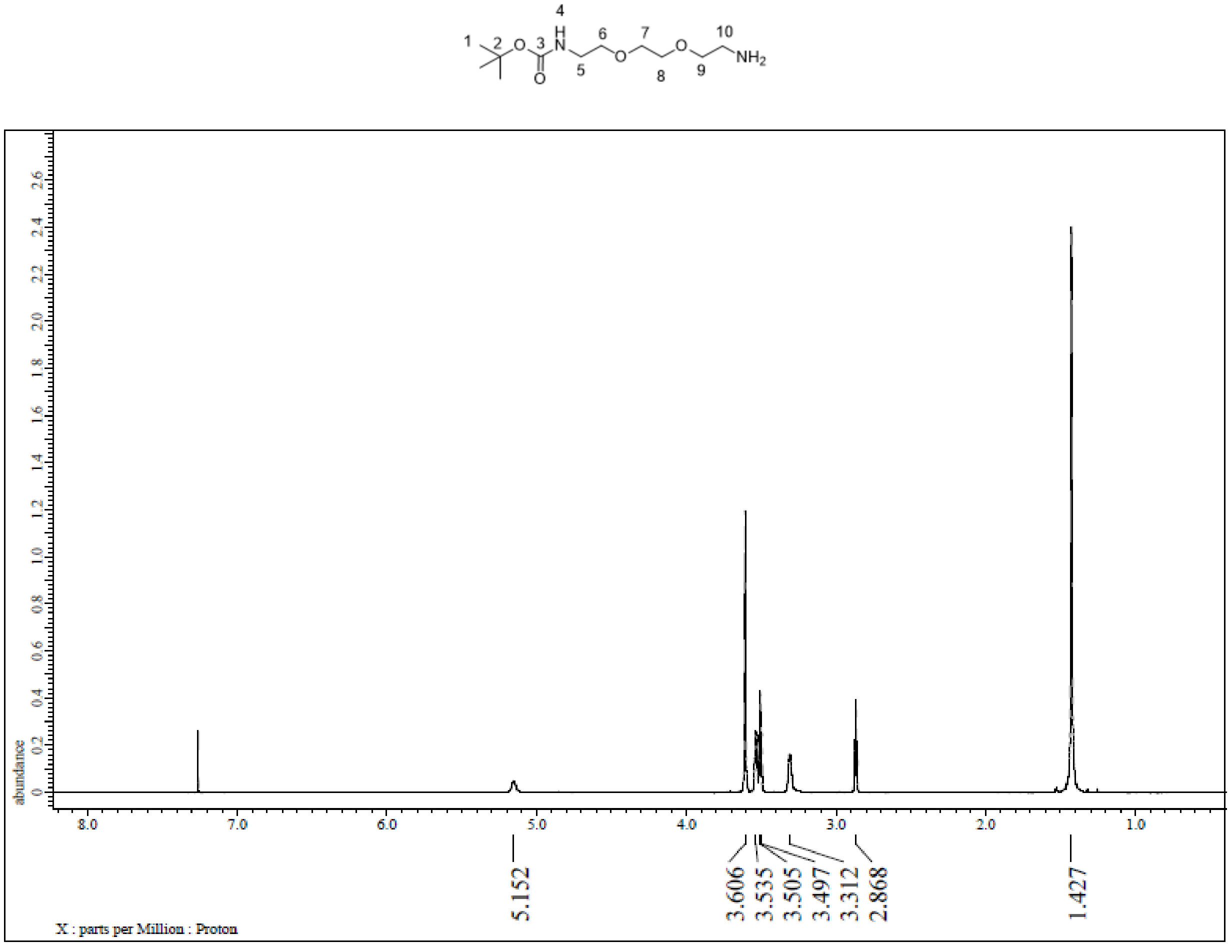

S4. ^{1}H NMR spectrum of compound (b).

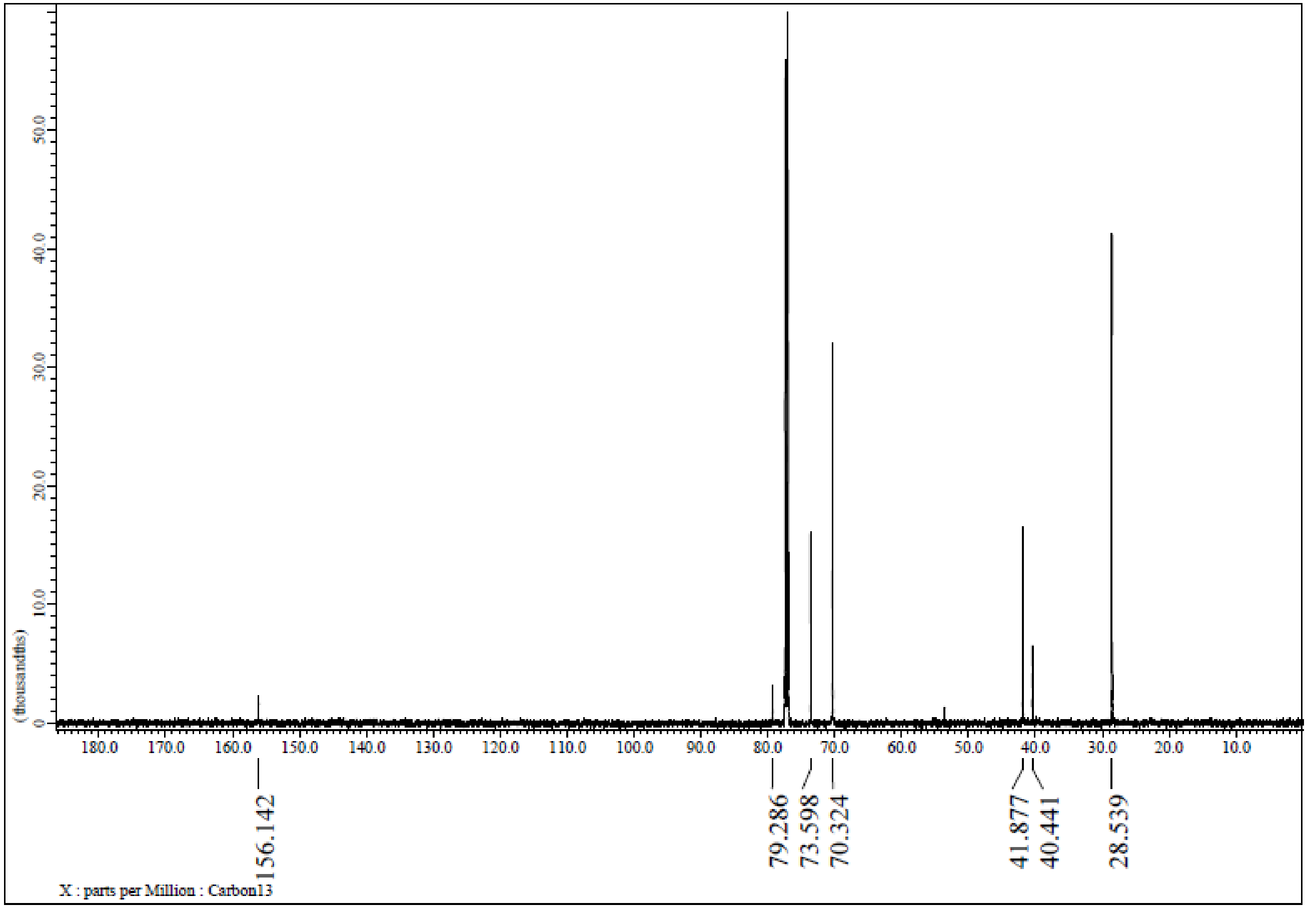

S5. ^{13}C NMR spectrum of compound (b).

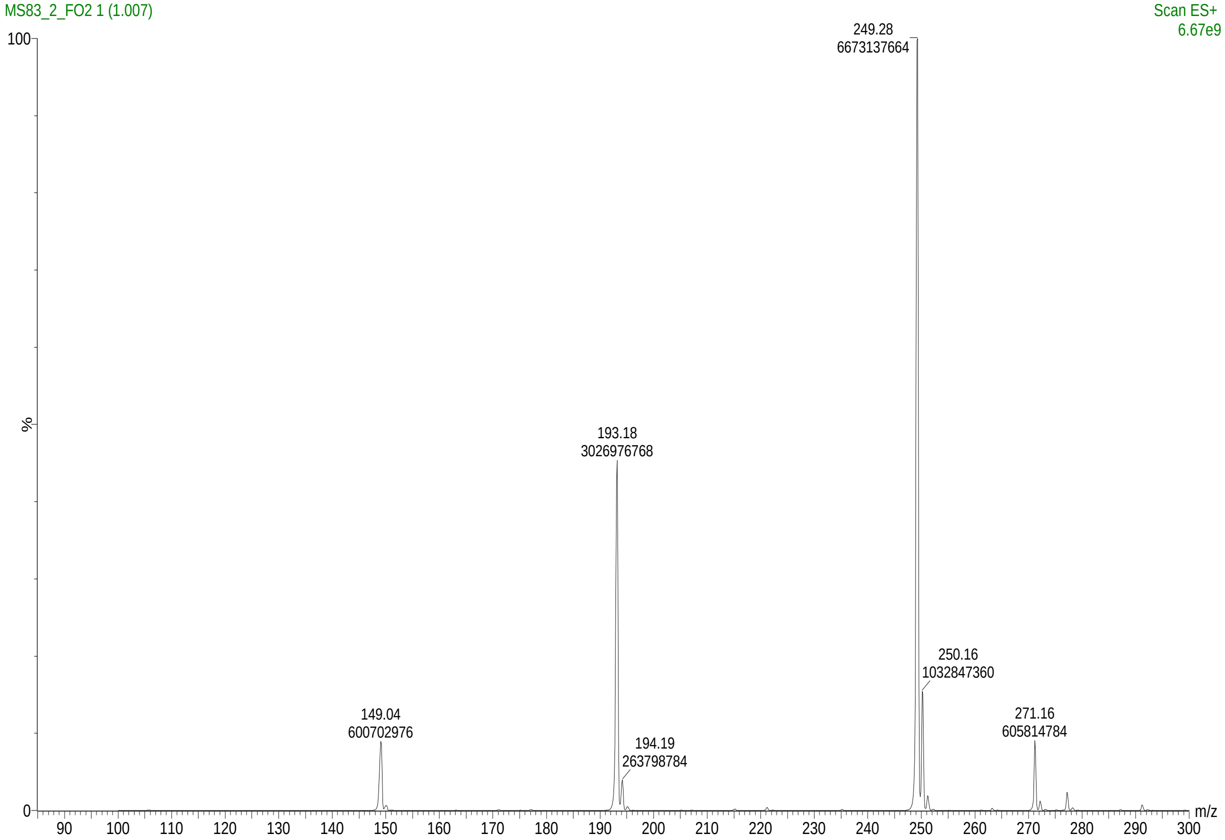

S6. MS spectrum of compound (b).

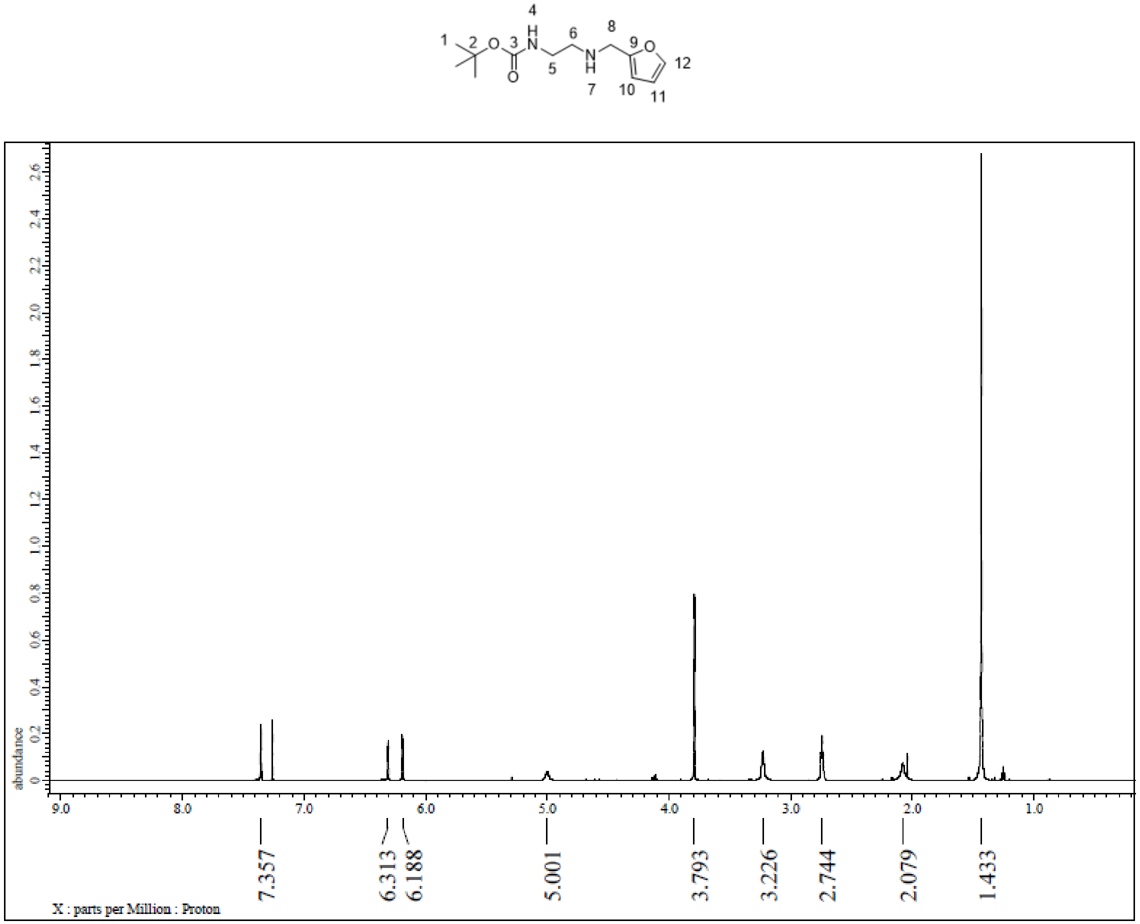

S7. ^{1}H NMR spectrum of compound (c).

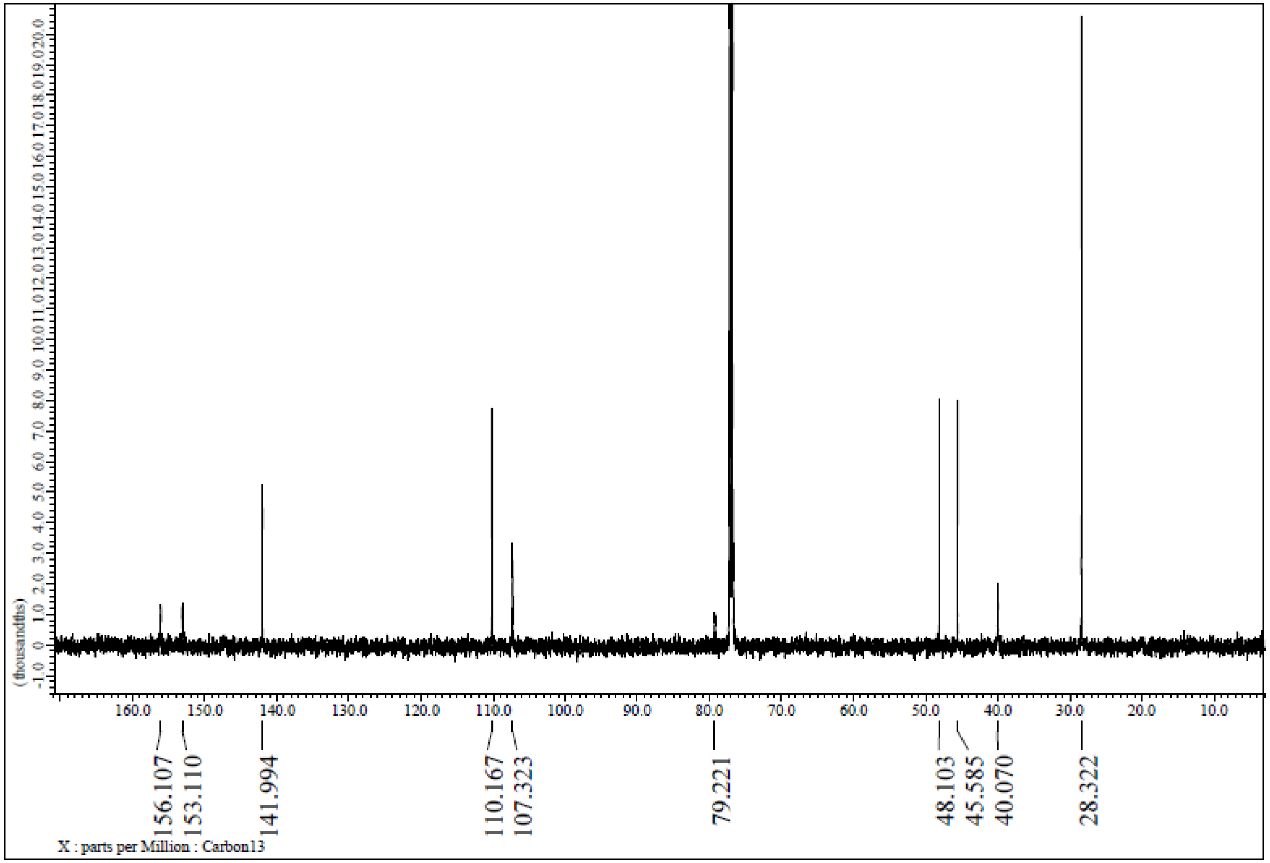

S8. ^{13}C NMR spectrum of compound (c).

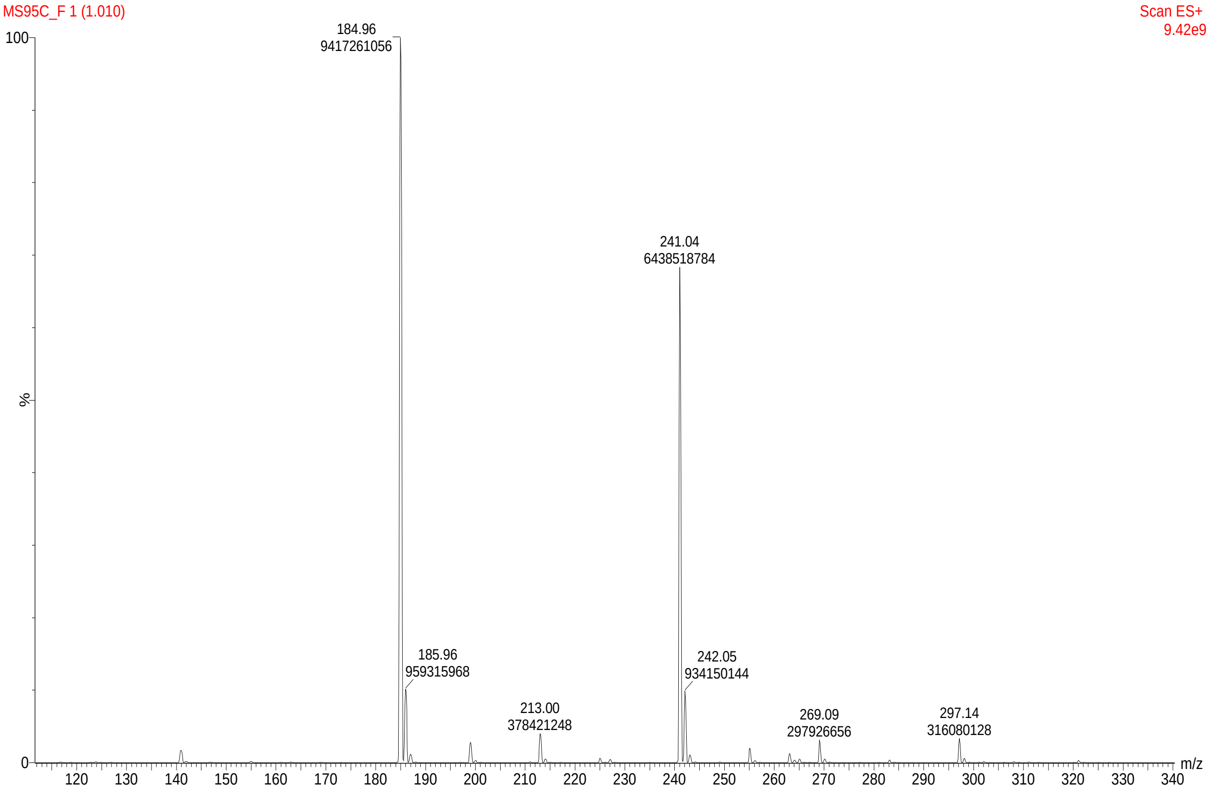

S9. MS spectrum of compound (c).

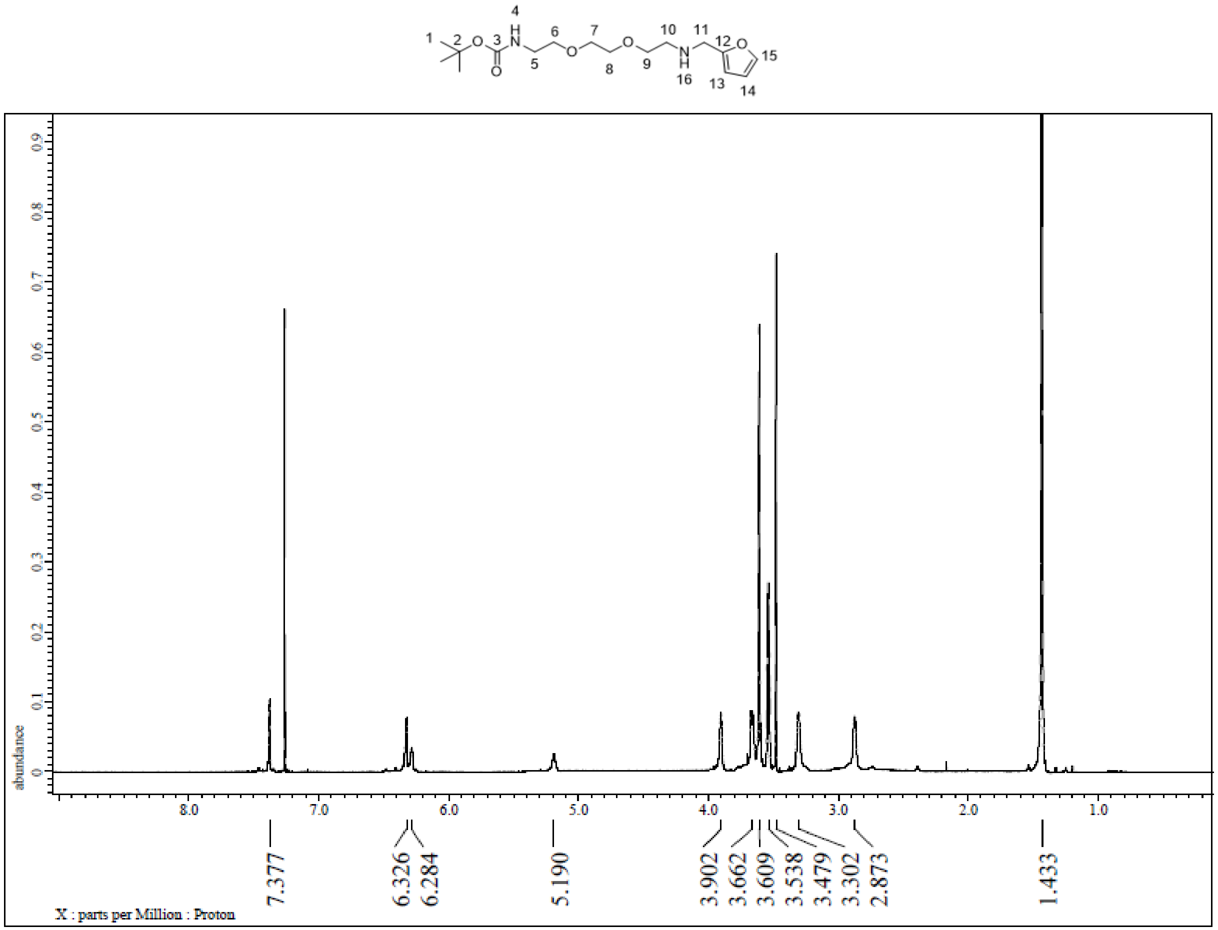

S10. ^{1}H NMR spectrum of compound (d).

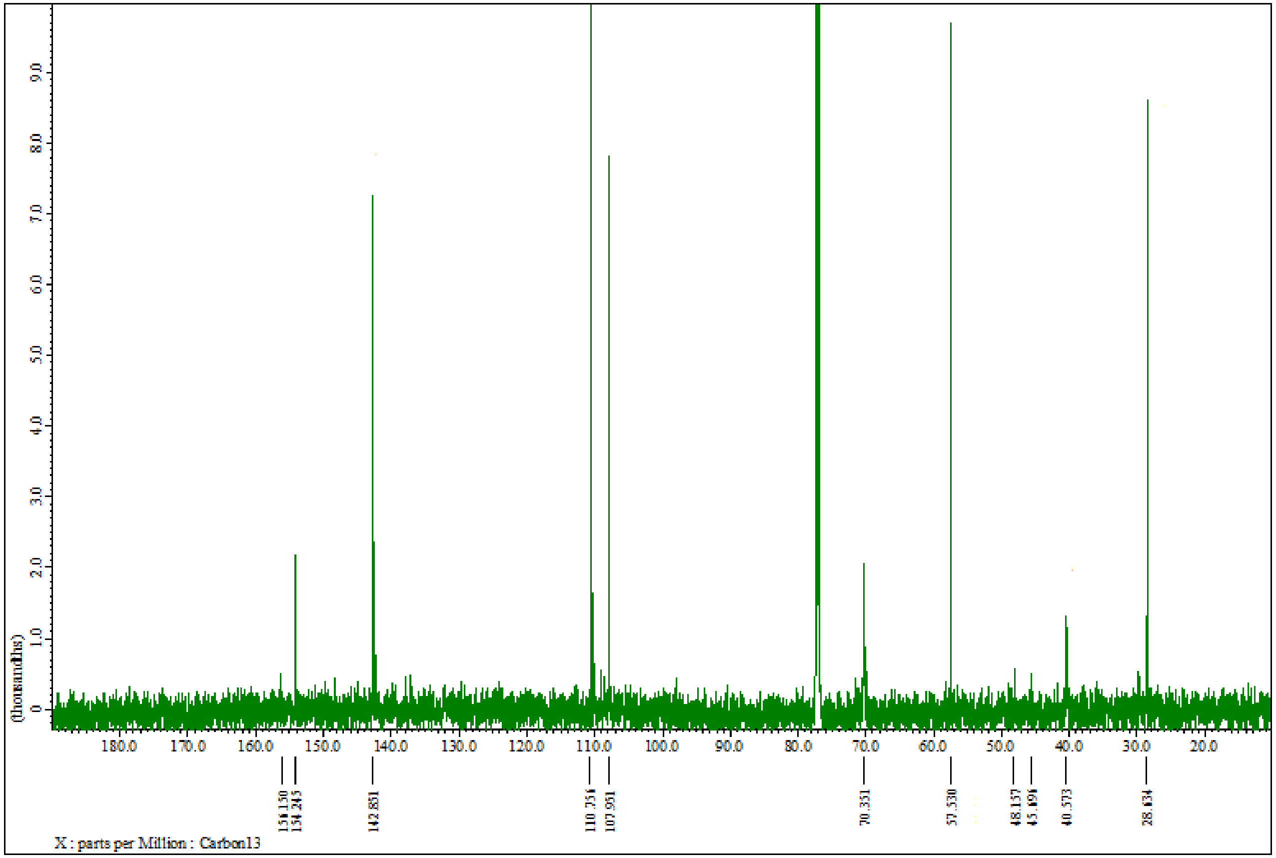

S11. ^{13}C NMR spectrum of compound (d).

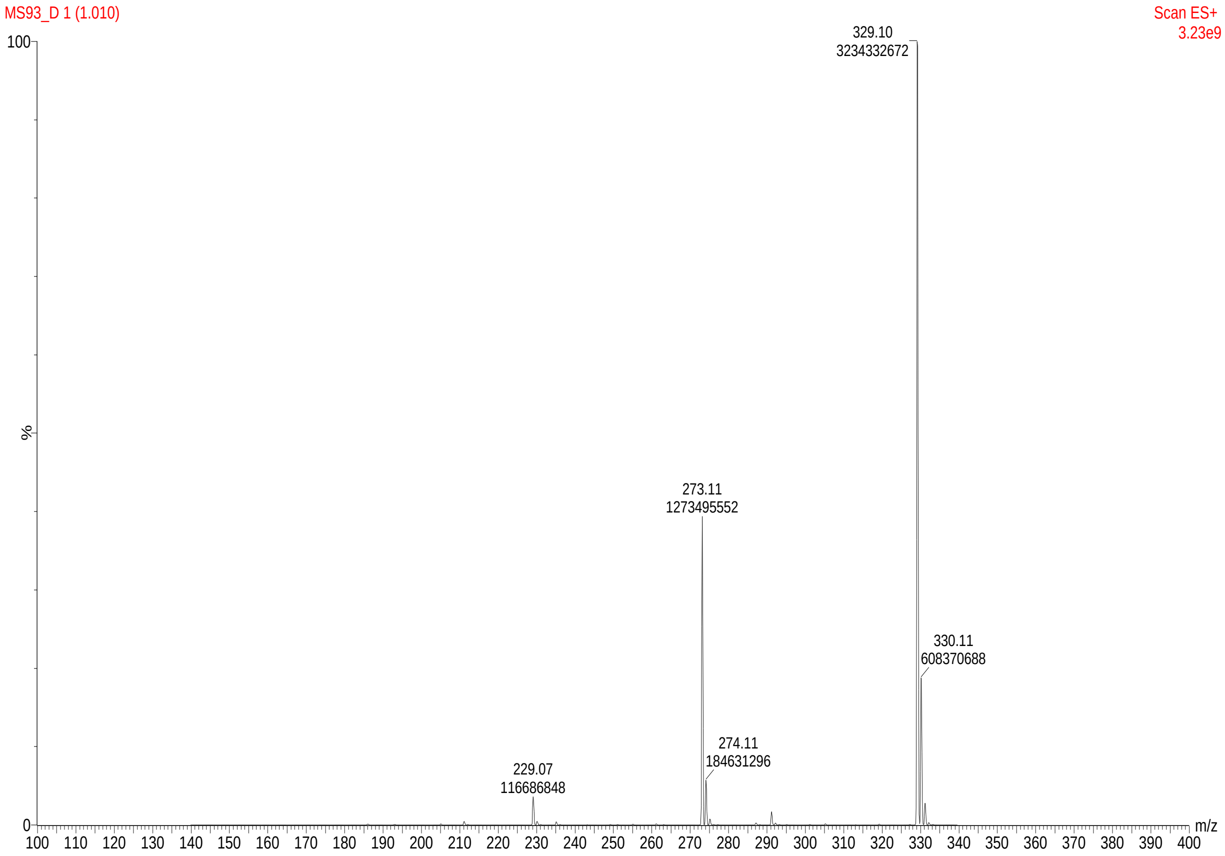

S12. MS spectrum of compound (d).

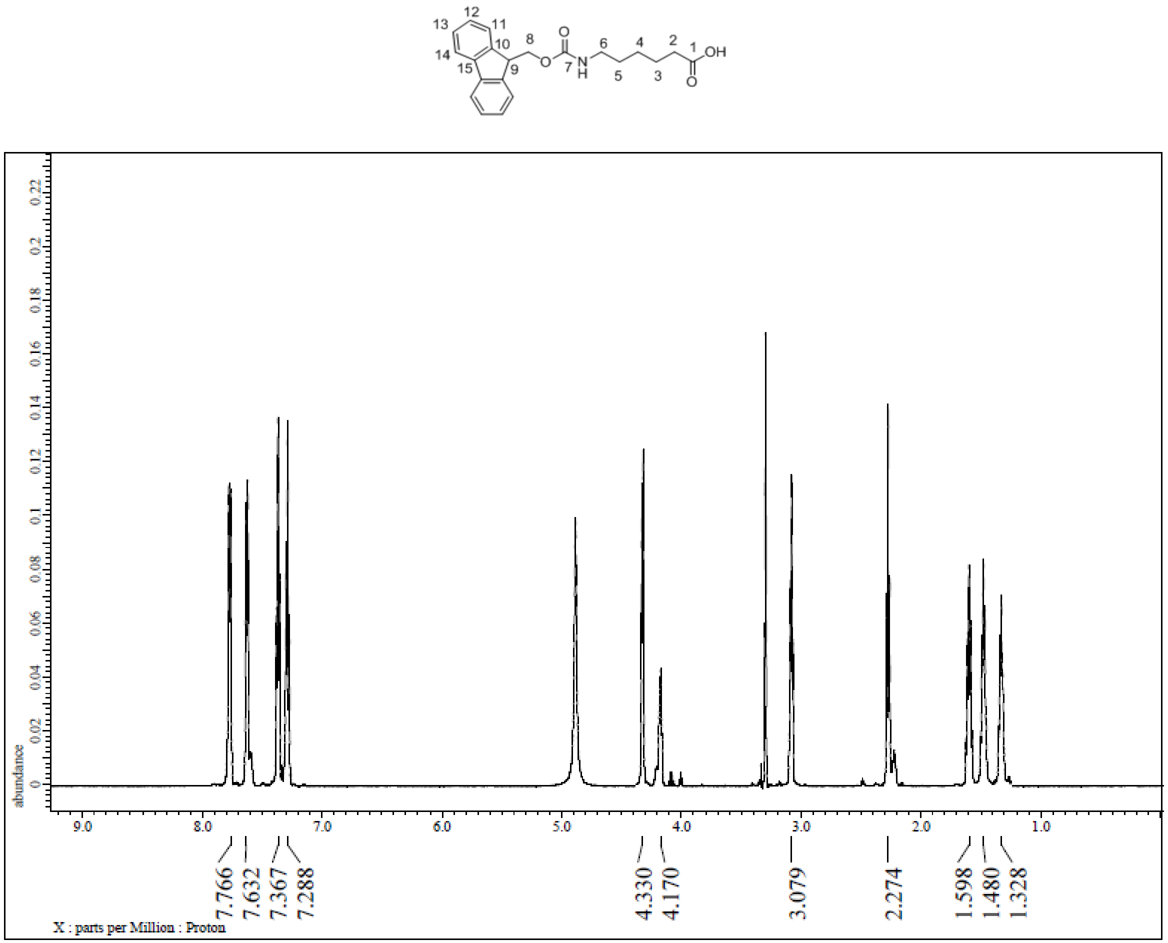

S13. ^{1}H NMR spectrum of compound (e).

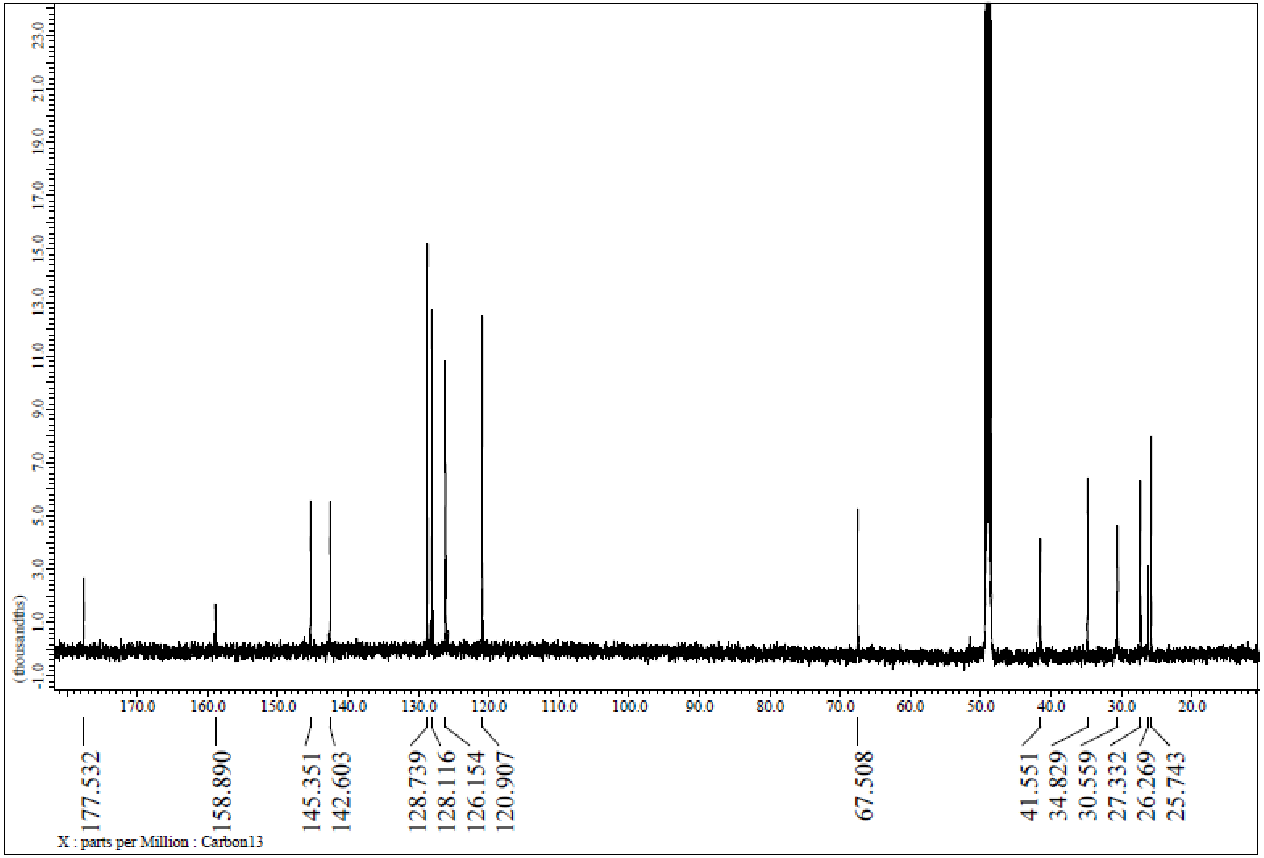

S14. ^{13}C NMR spectrum of compound (e).

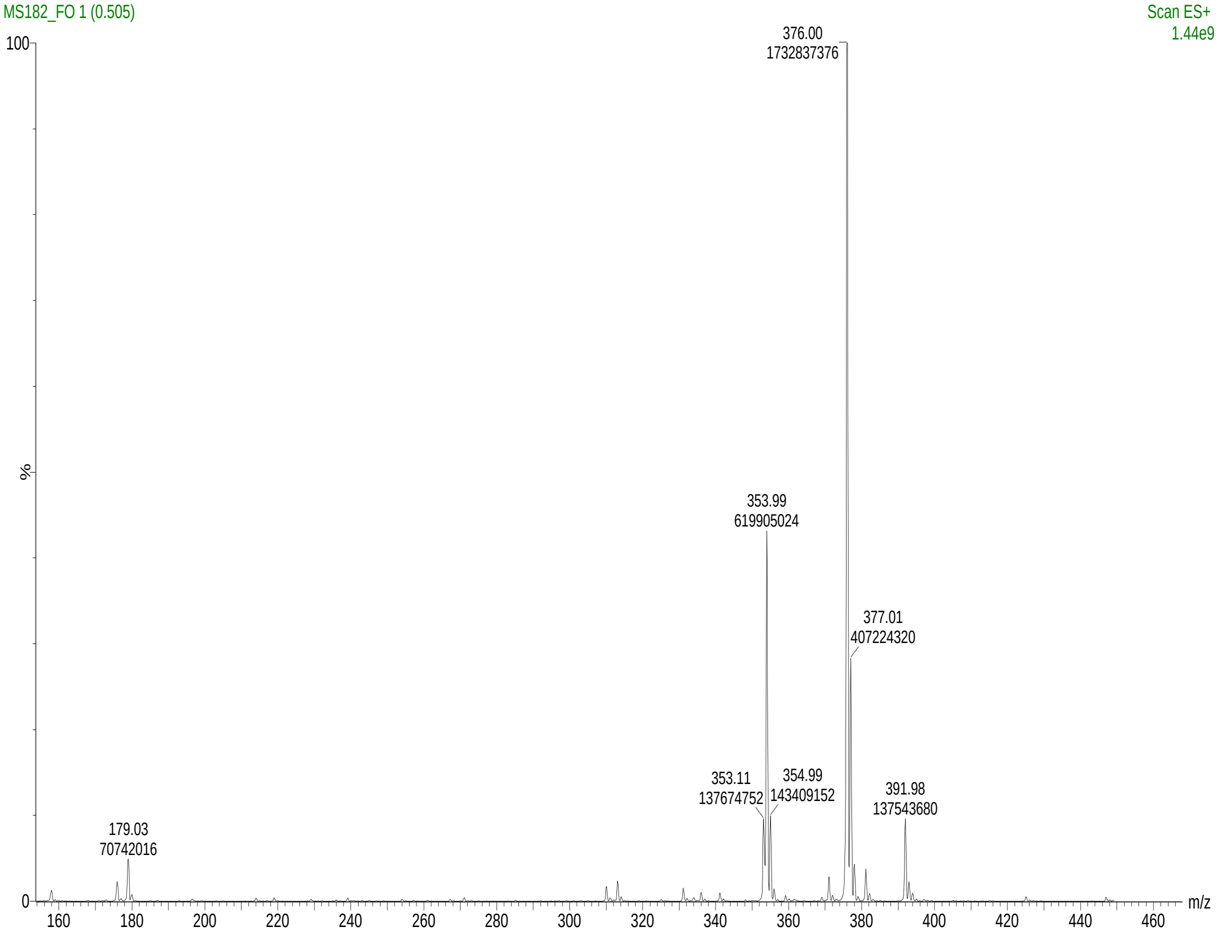

S15. MS spectrum of compound (e).

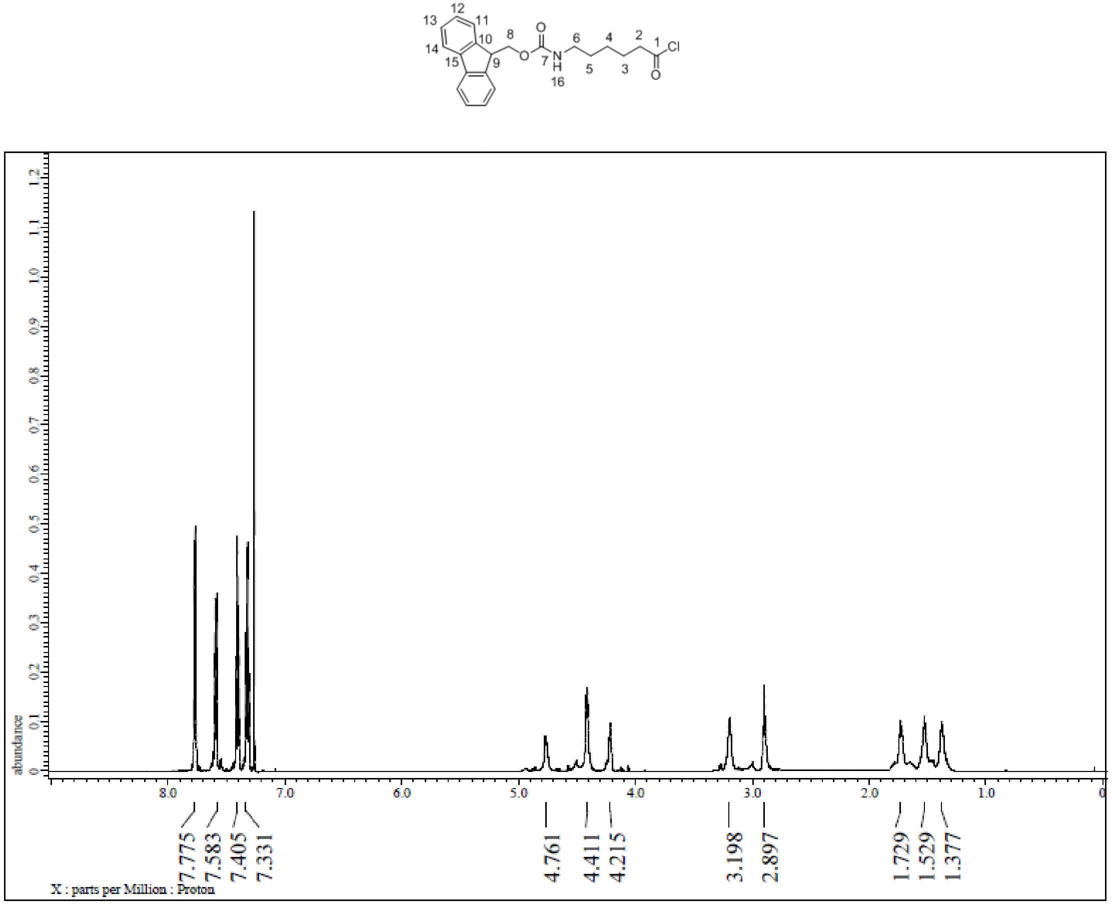

S16. ^{1}H NMR spectrum of compound (f).

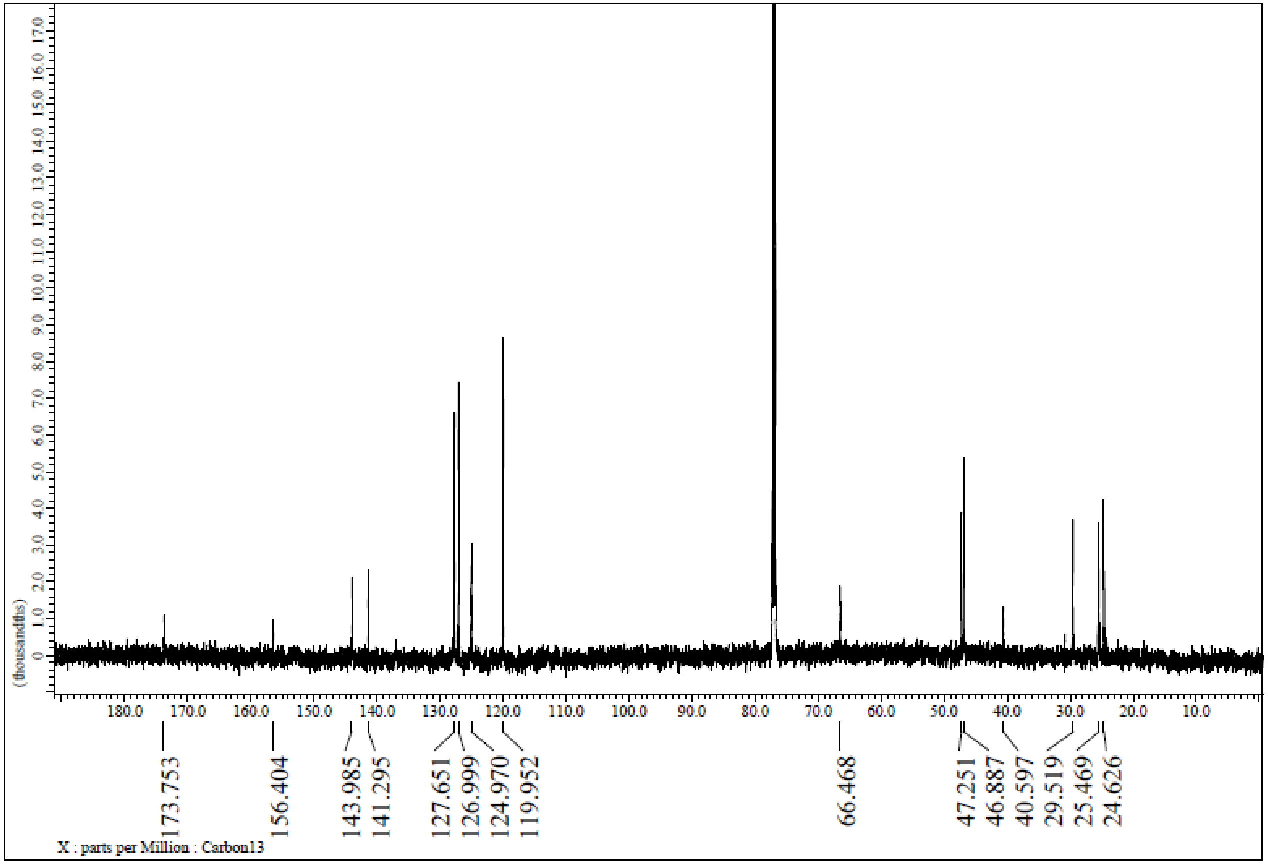

S17. ^{13}C NMR spectrum of compound (f).

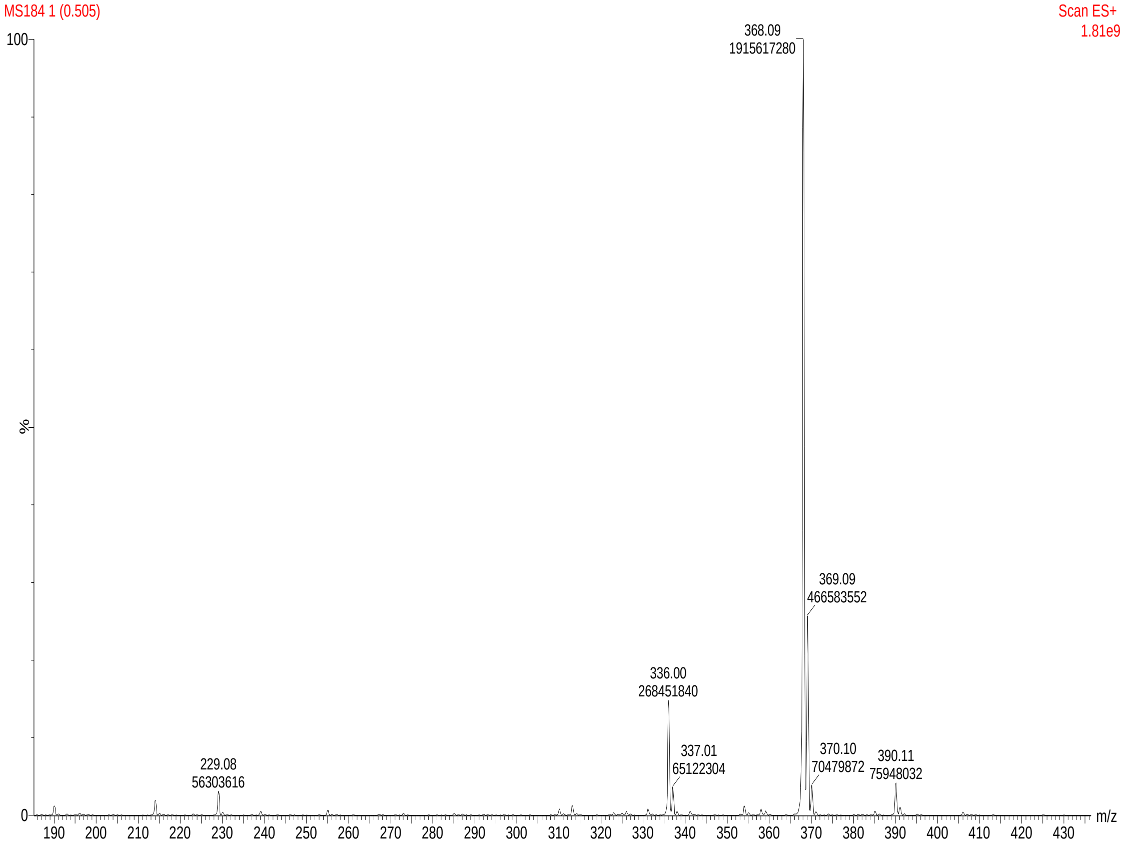

S18. MS spectrum of compound (f).

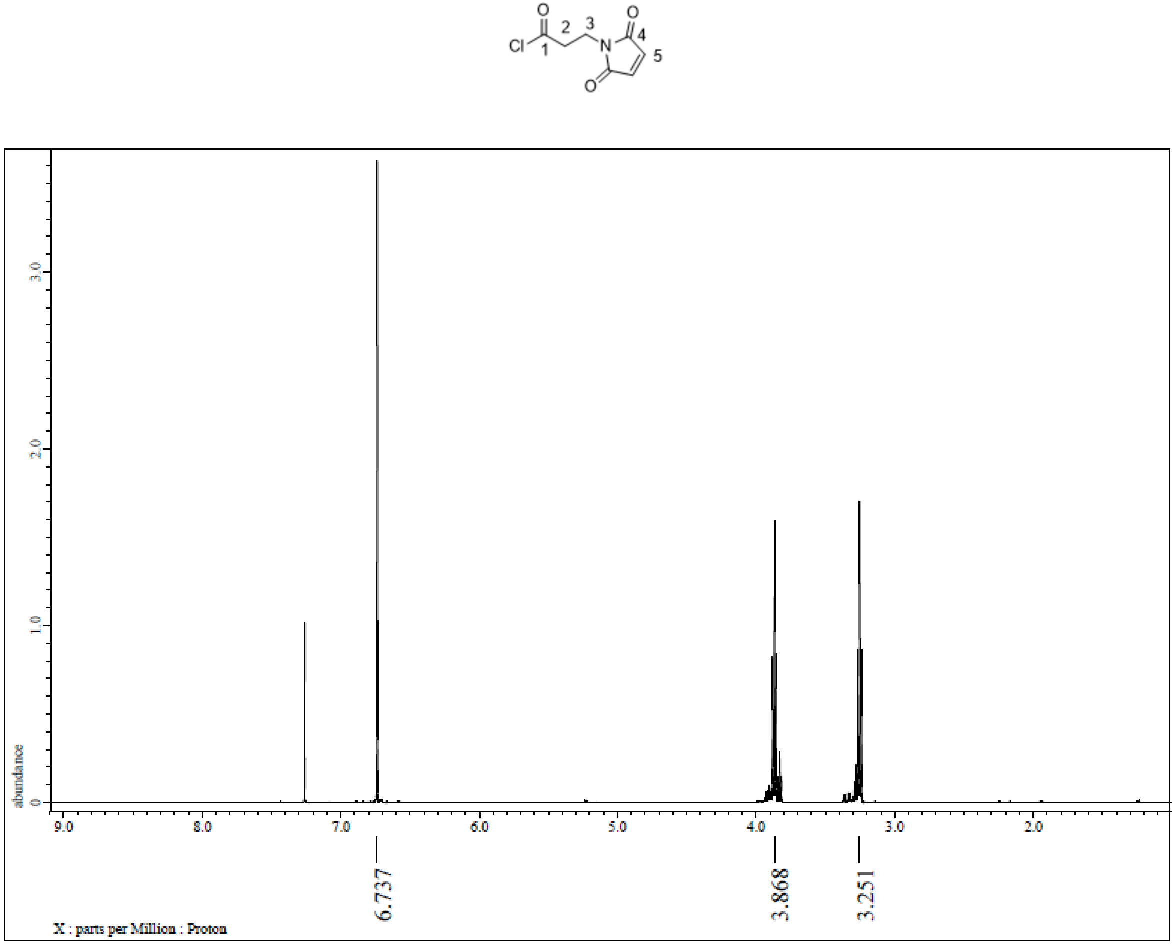

S19. ^{1}H NMR spectrum of compound (g).

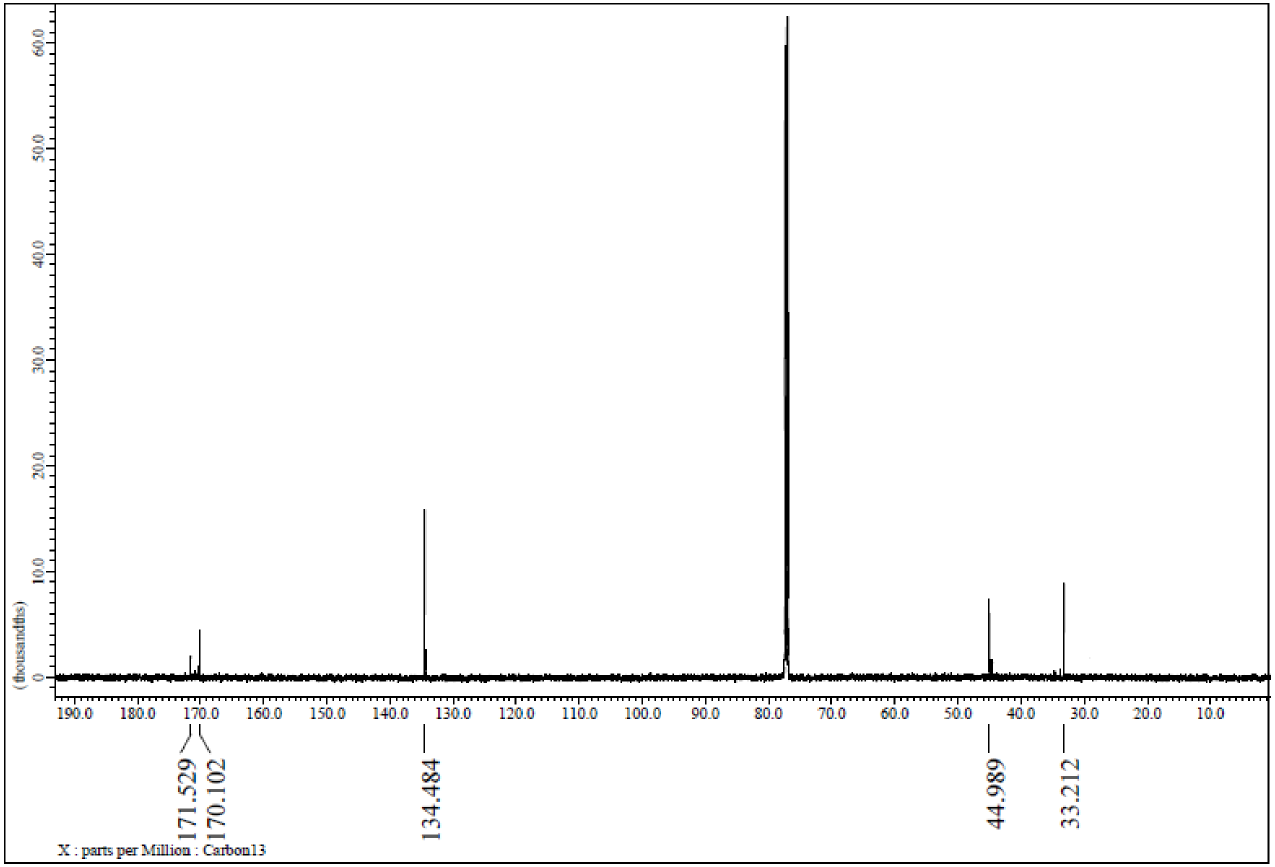

S20. ^{13}C NMR spectrum of compound (g).

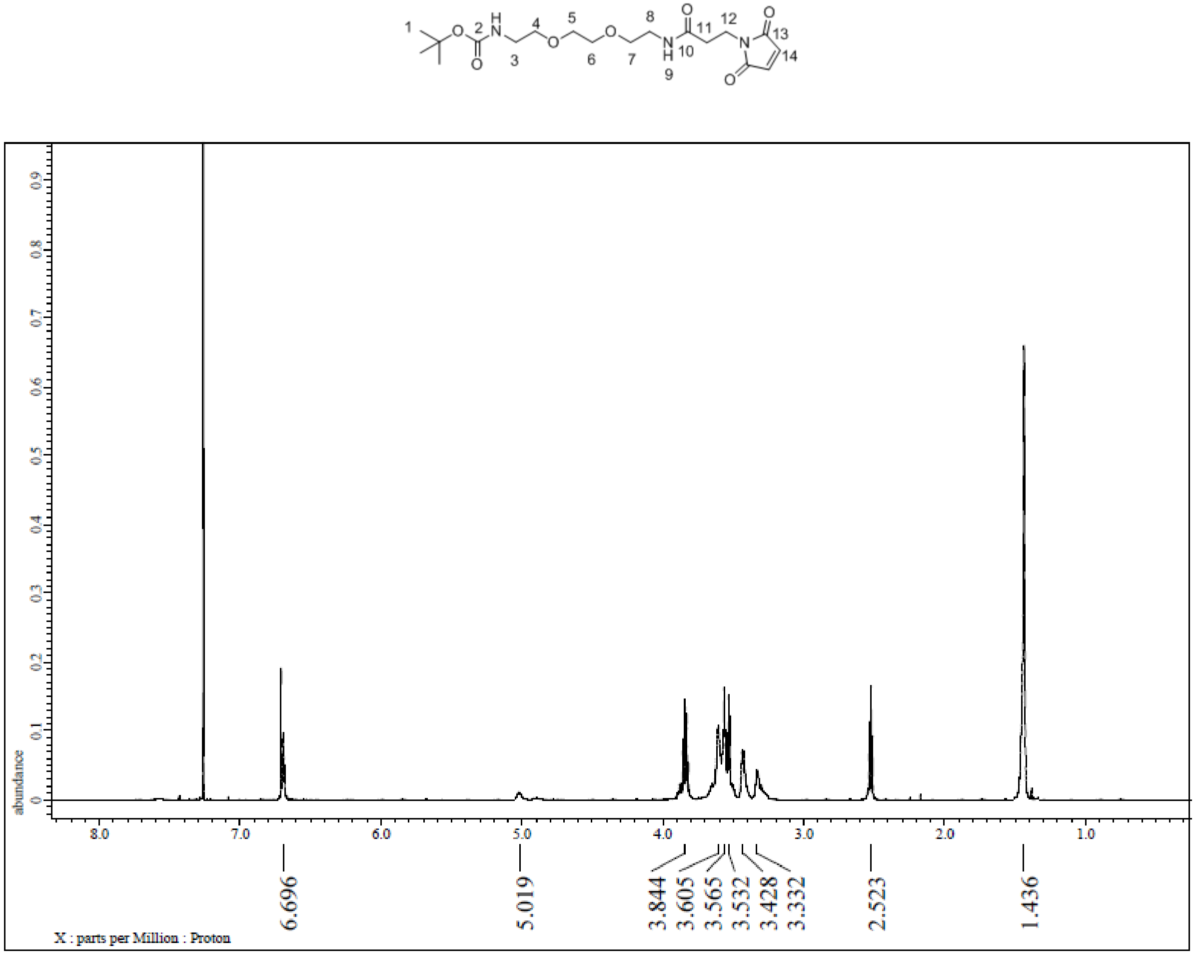

S21. ^{1}H NMR spectrum of compound (h).

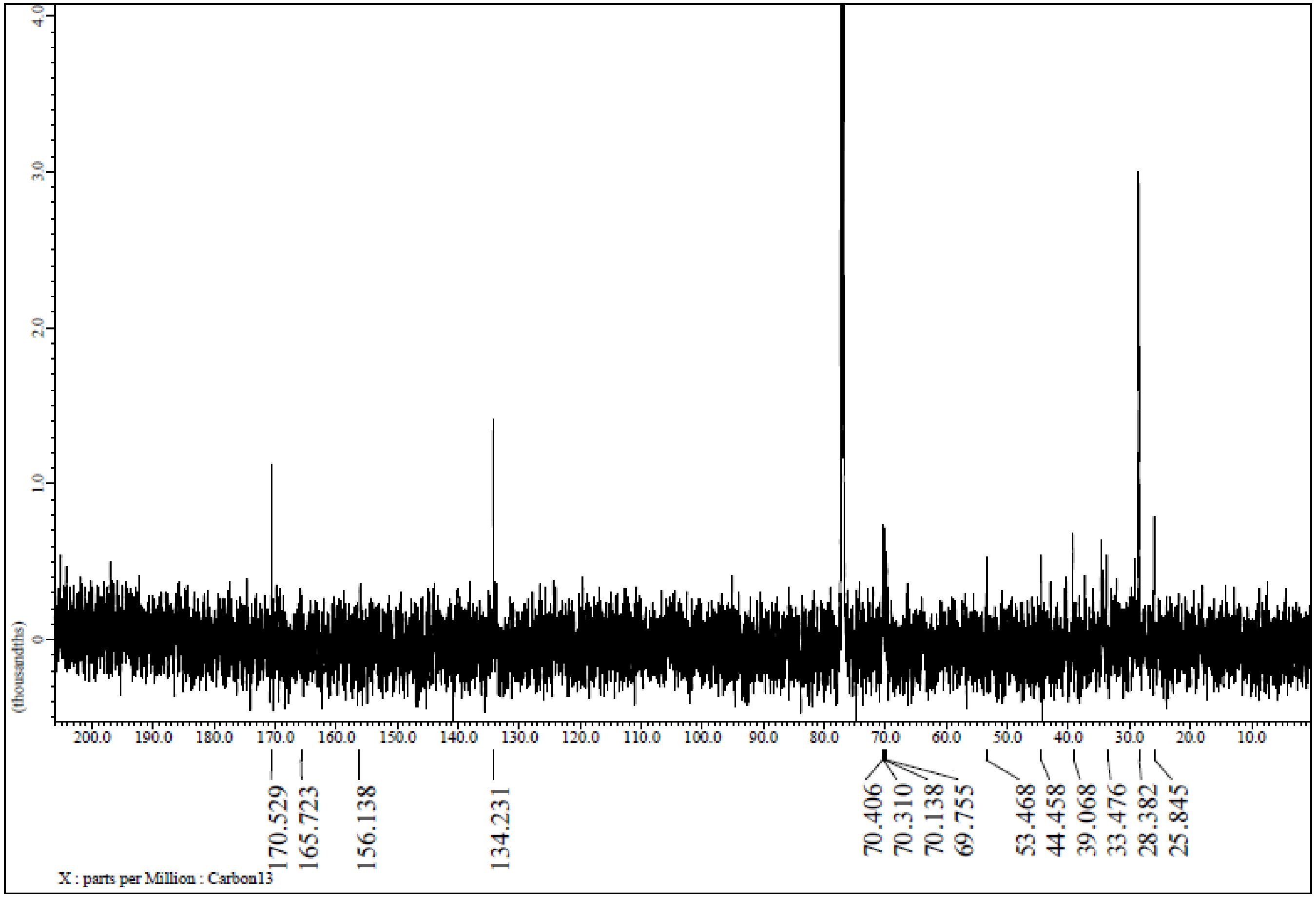

S22. ^{13}C NMR spectrum of compound (h).

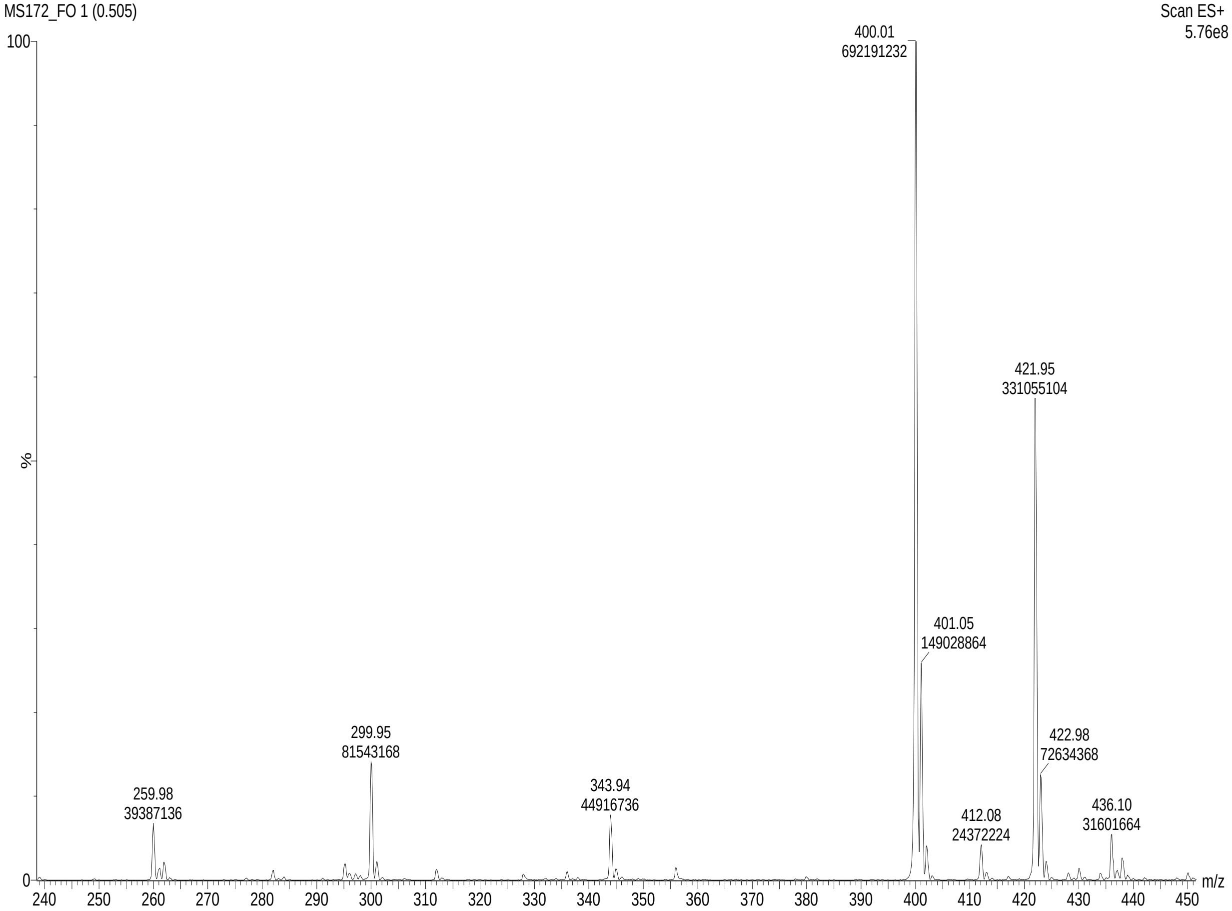

S23. MS spectrum of compound (h).

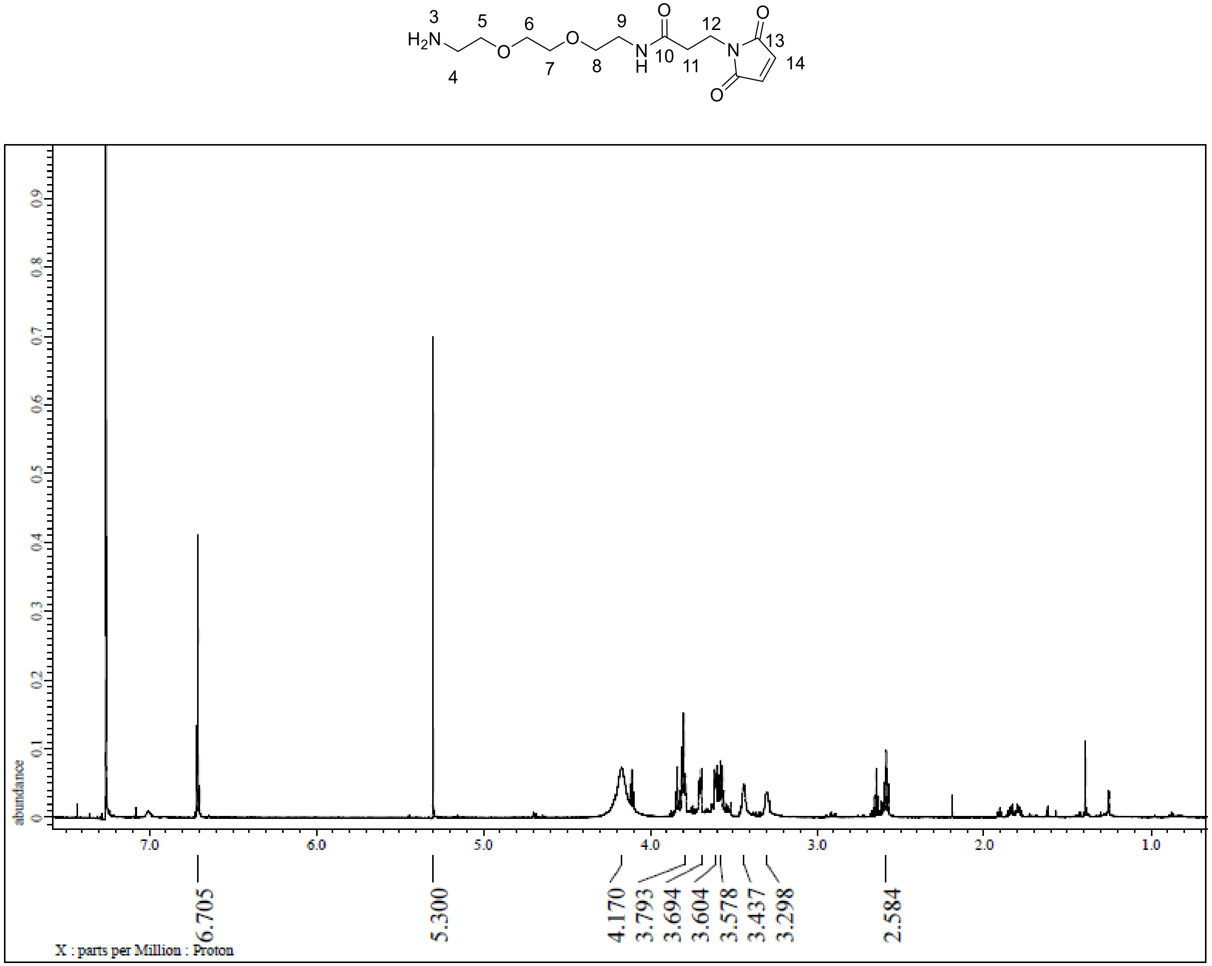

S24. ^{1}H NMR spectrum of compound (i).

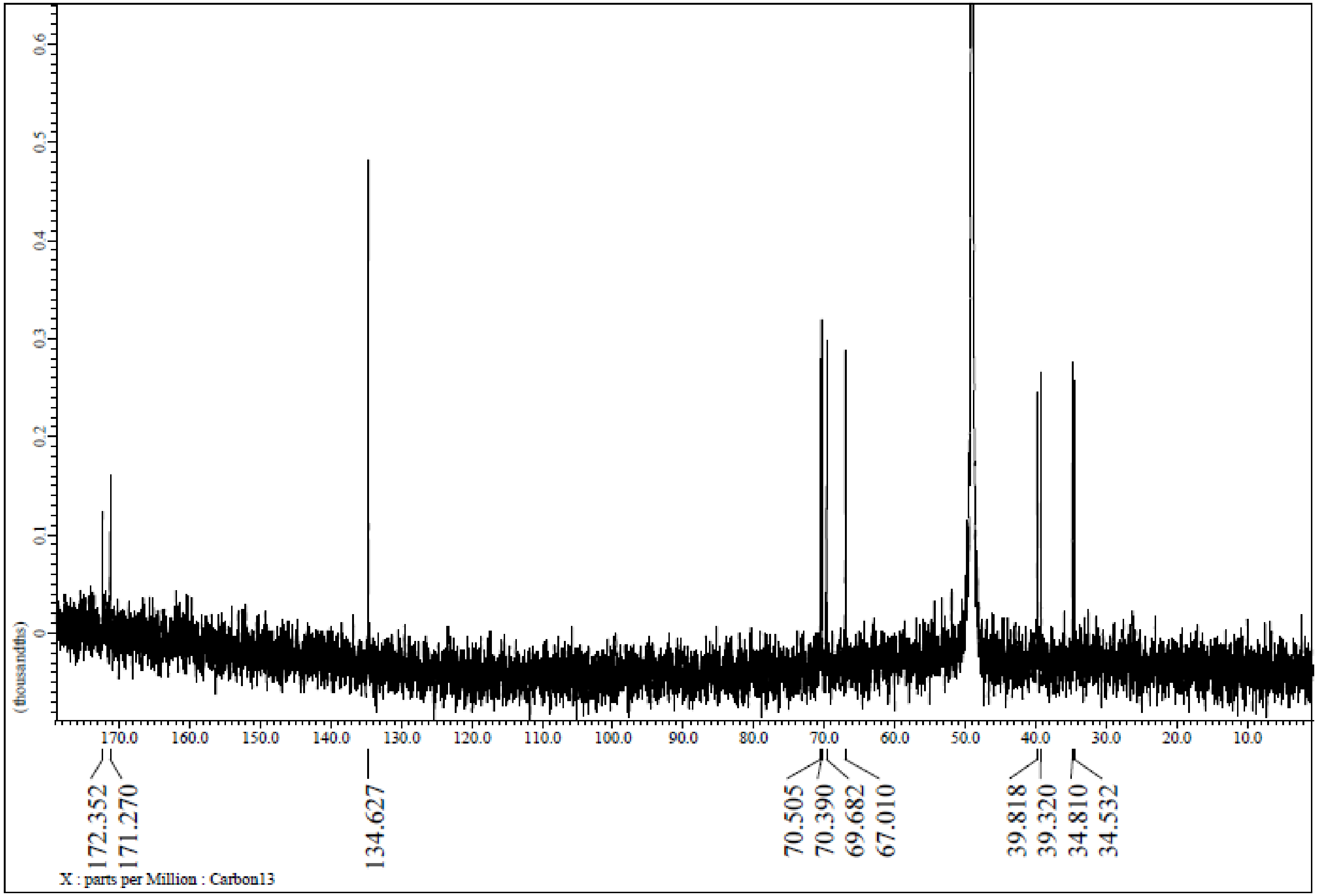

S25. ^{13}C NMR spectrum of compound (i).

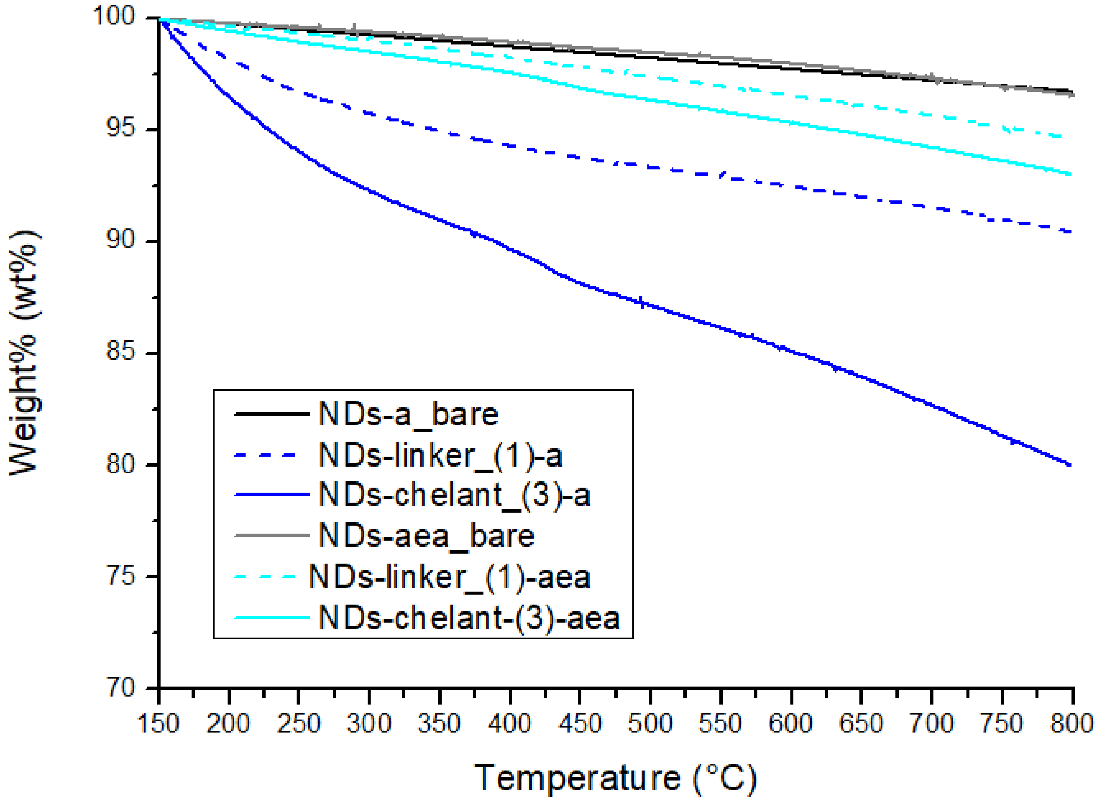

S26. Thermogravigrams of NDs-short linker (1)-a, (1)-aea and NDs-short AAZTA (3)-a, (3)-aea nanosystems obtained with Diels-Alder approach.

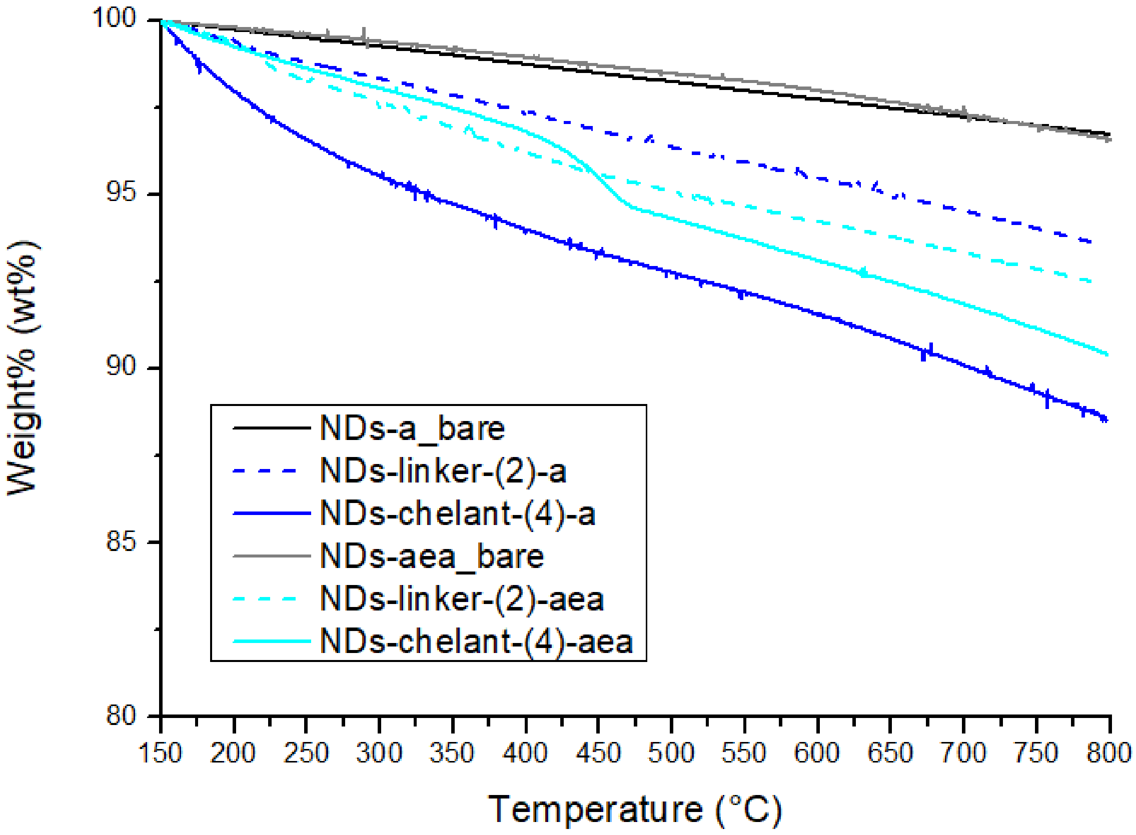

S27. Thermogravigrams of NDs-long linker (2)-a, (2)-aea and NDs-long AAZTA (4)-a, (4)-aea nanosystems obtained with Diels-Alder approach.

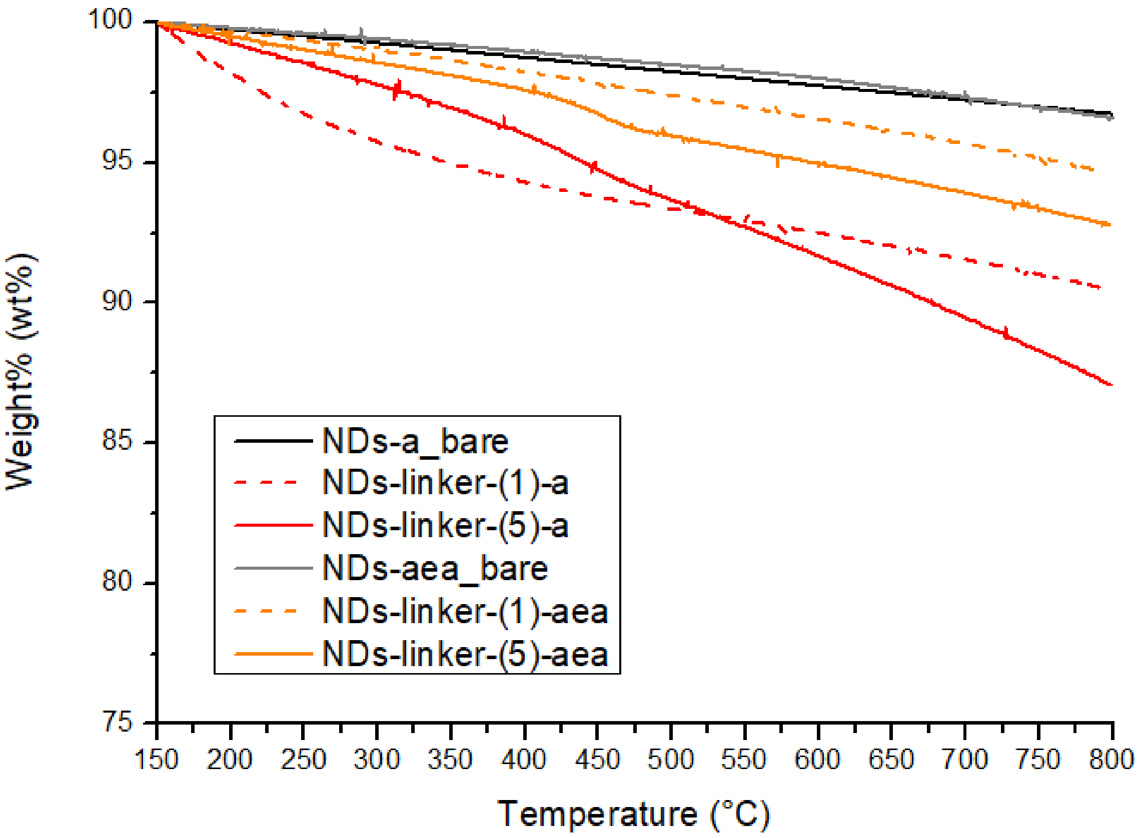

S28. Thermogravigrams of NDs-short linker (1)-a, (1)-aea and NDs-short CEDTA (5)-a, (5)-aea nanosystems obtained with Diels-Alder approach.

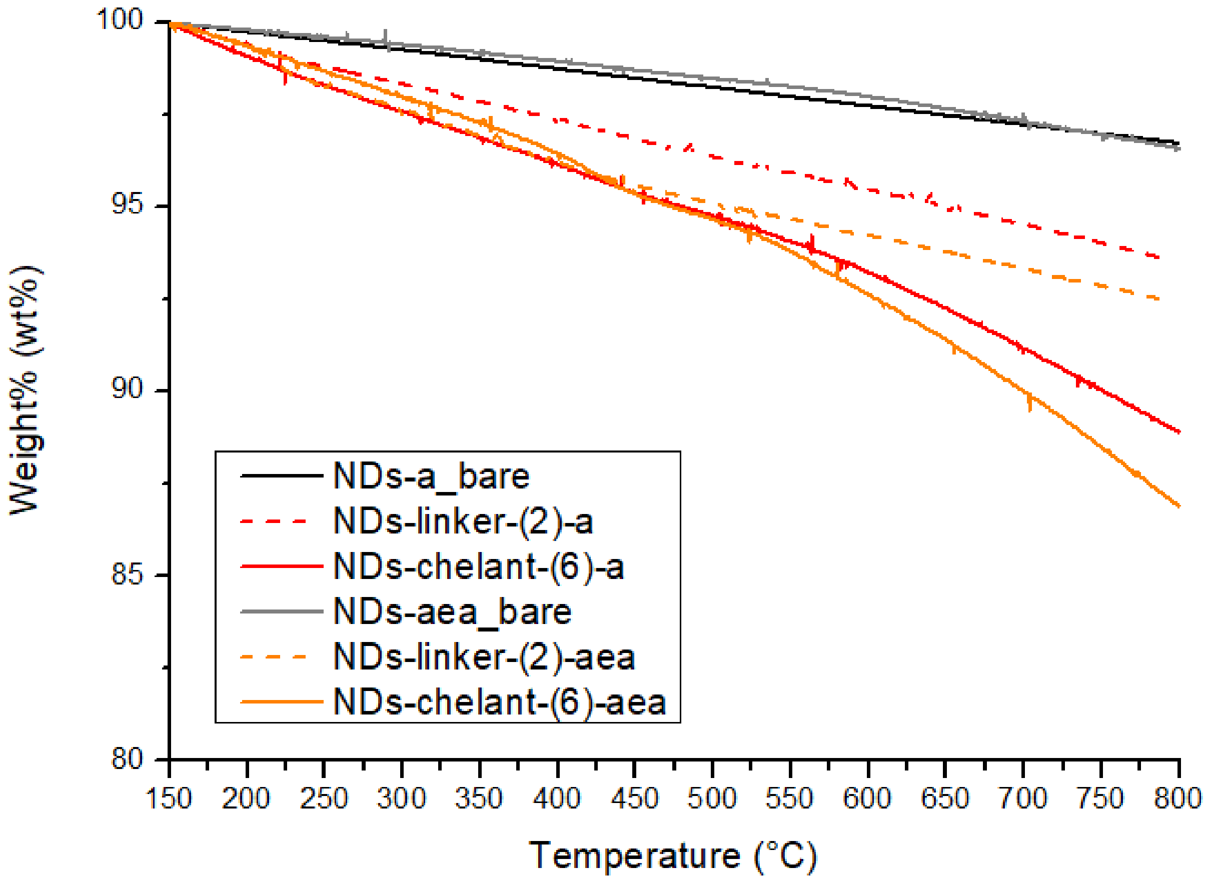

S29. Thermogravigrams of NDs-long linker (2)-a, (2)-aea and NDs-long CEDTA (6)-a, (6)-aea nanosystems obtained with Diels-Alder approach.

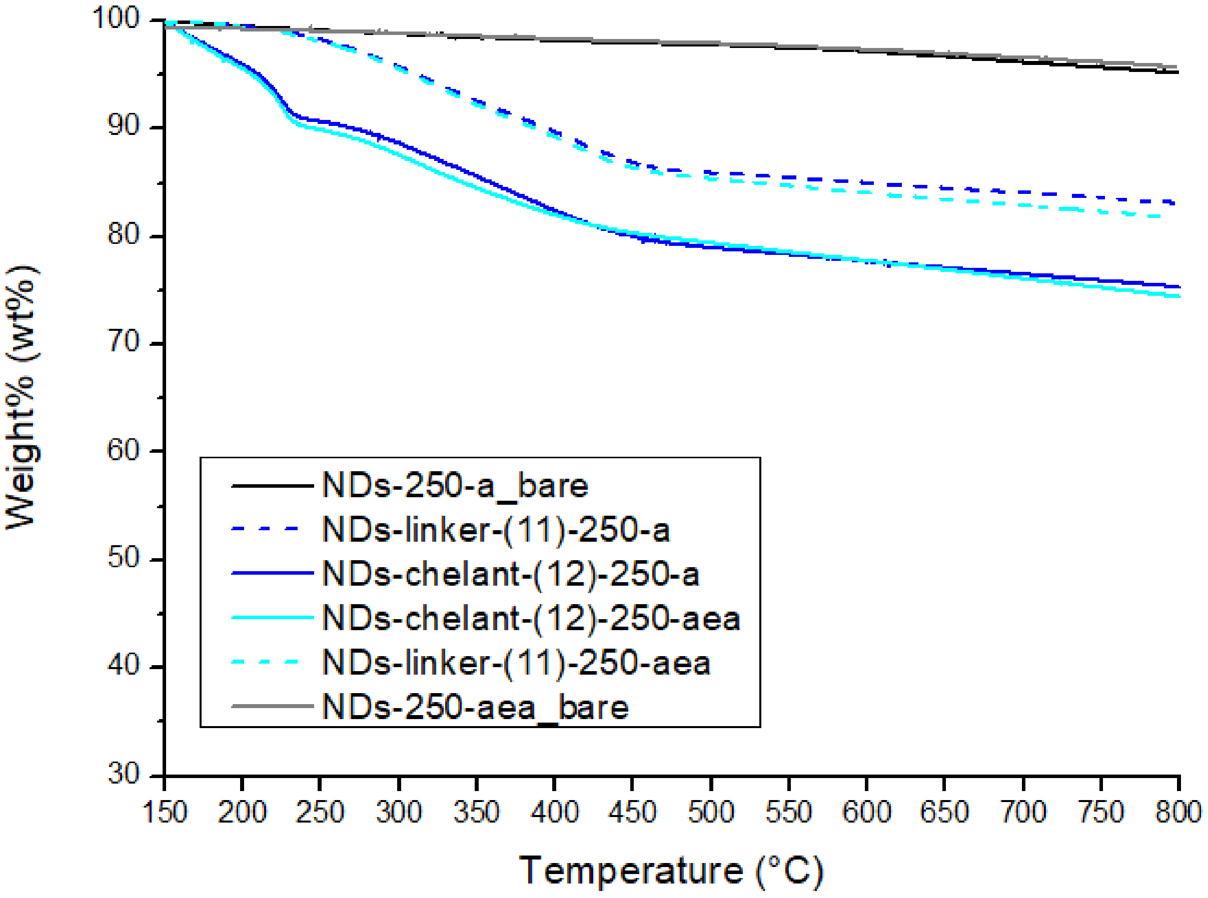

S30. Thermogravigrams of 250nm NDs-linker (11)-250-a, (11)-250-aea and NDs-AAZTA (12)-250-a, (12)-250-aea nanosystems obtained with 1,3-dipolar approach.

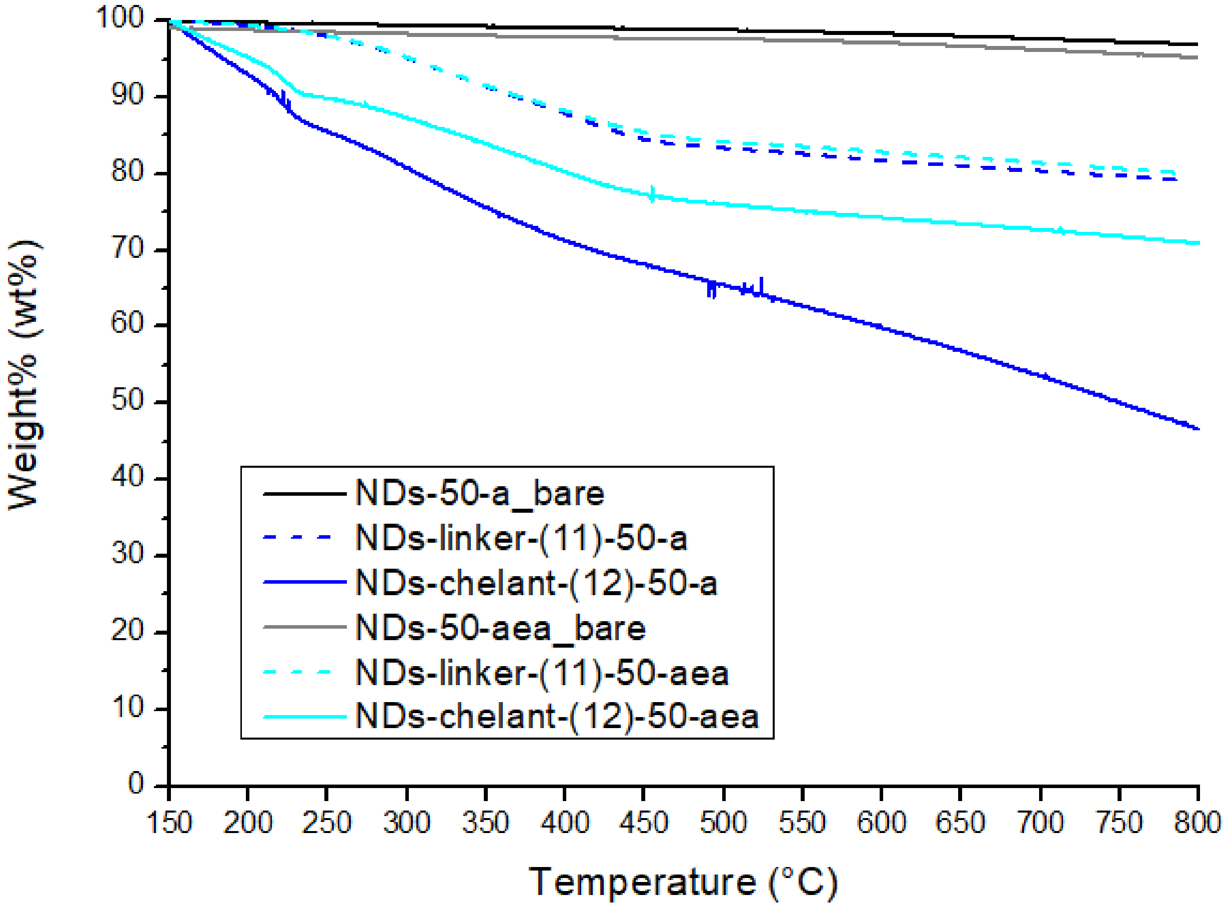

S31. Thermogravigrams of 50nm NDs-linker (11)-50-a, (11)-50-aea and NDs-AAZTA (12)-50-a, (12)-50-aea nanosystems obtained with 1,3-dipolar approach.

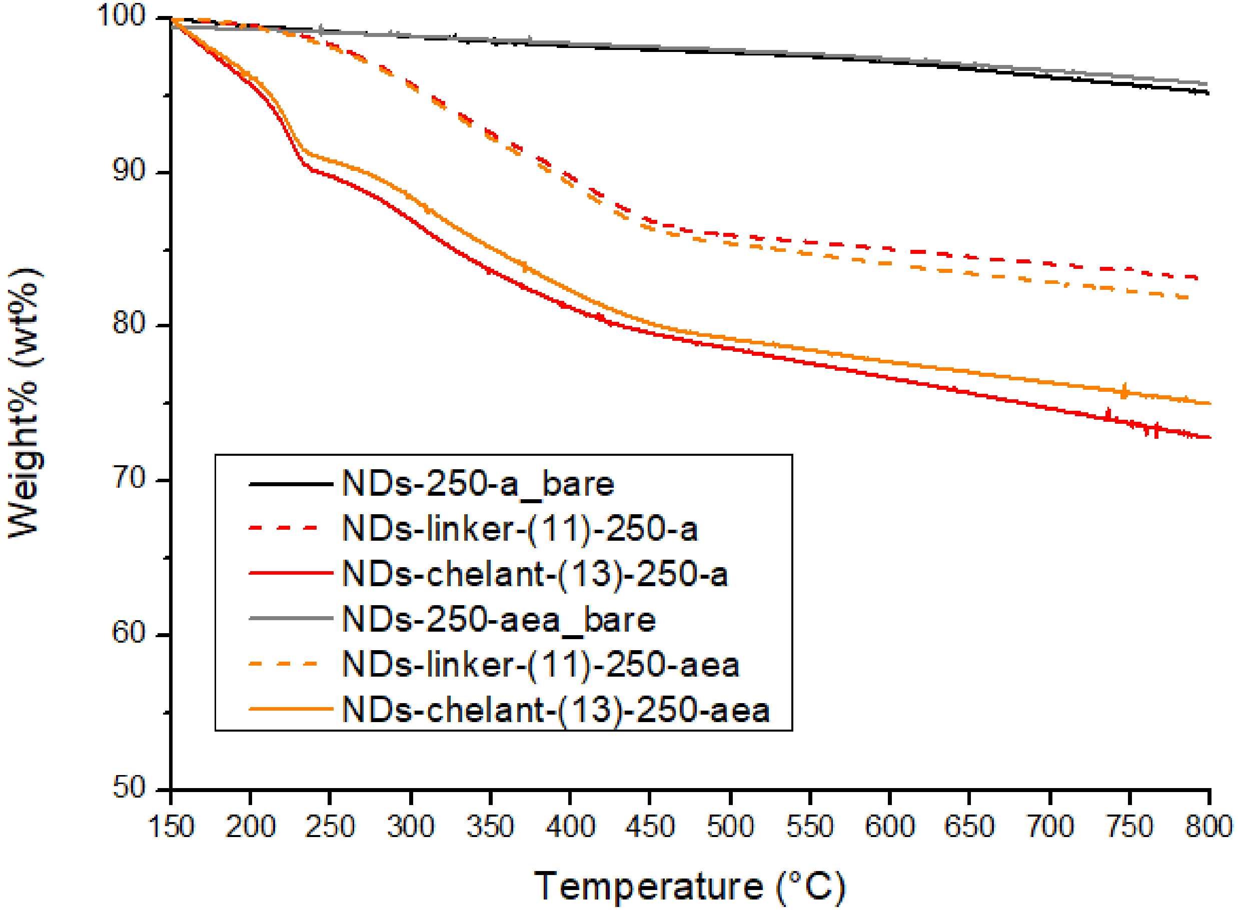

S32. Thermogravigrams of 250nm NDs-linker (11)-250-a, (11)-250-aea and NDs-CEDTA (13)-250-a, (13)-250-aea nanosystems obtained with 1,3-dipolar approach.

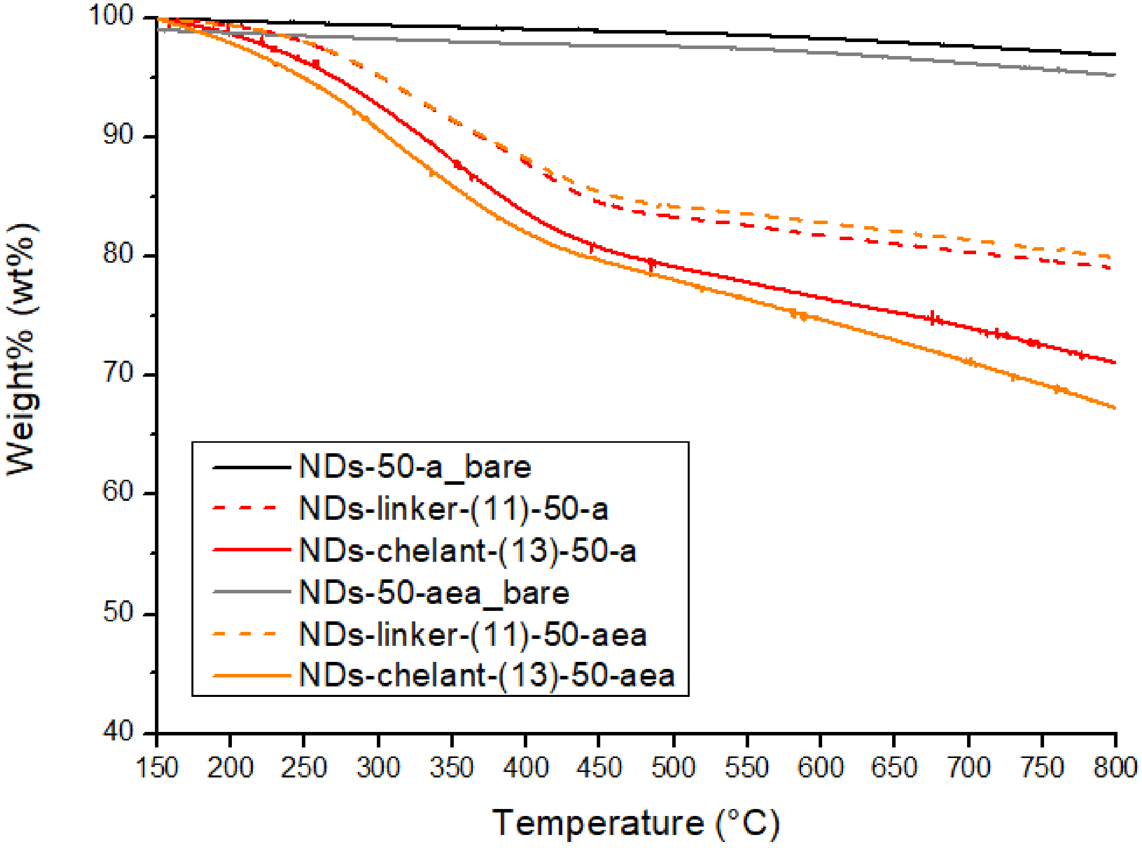

S33. Thermogravigrams of 50nm NDs-linker (11)-50-a, (11)-50-aea and NDs-CEDTA (13)-50-a, (13)-50-aea nanosystems obtained with 1,3-dipolar approach.

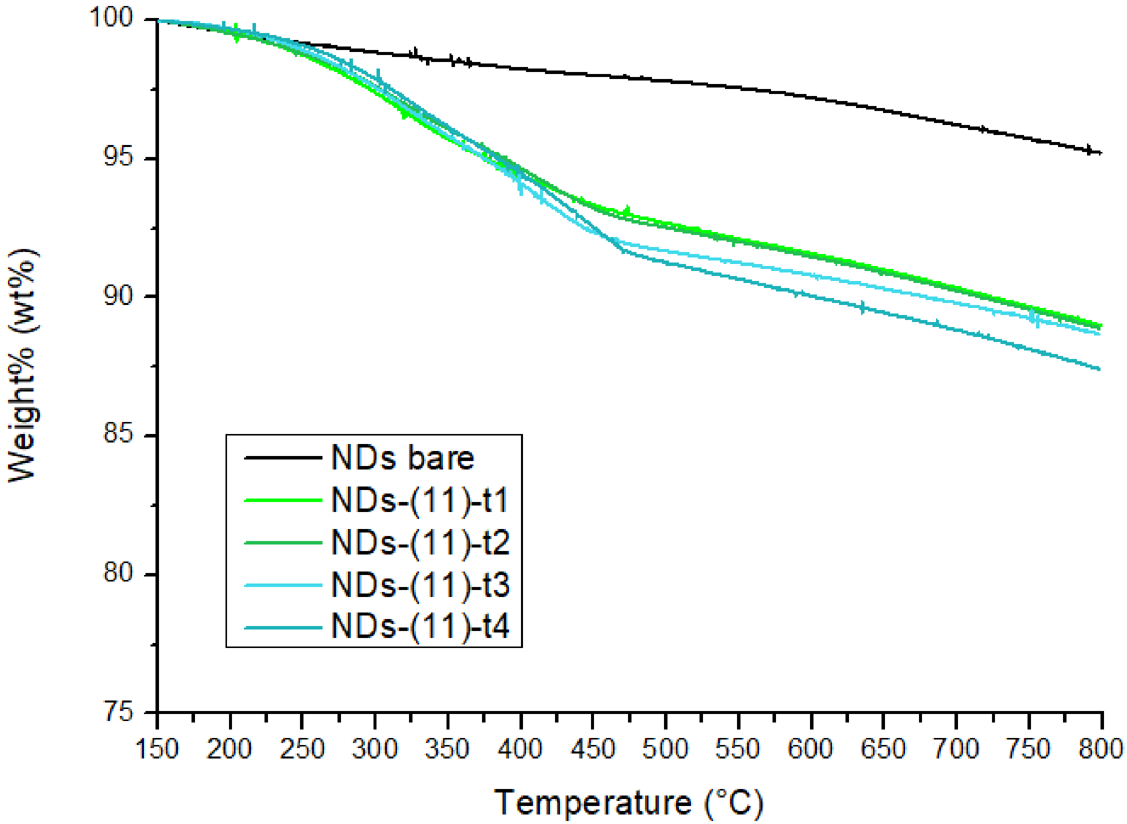

S34. Thermogravigrams of 50 nm NDs reacted with lysine and paraformaldehyde NDs-(11) at different times (t1, t2, t3, t4).

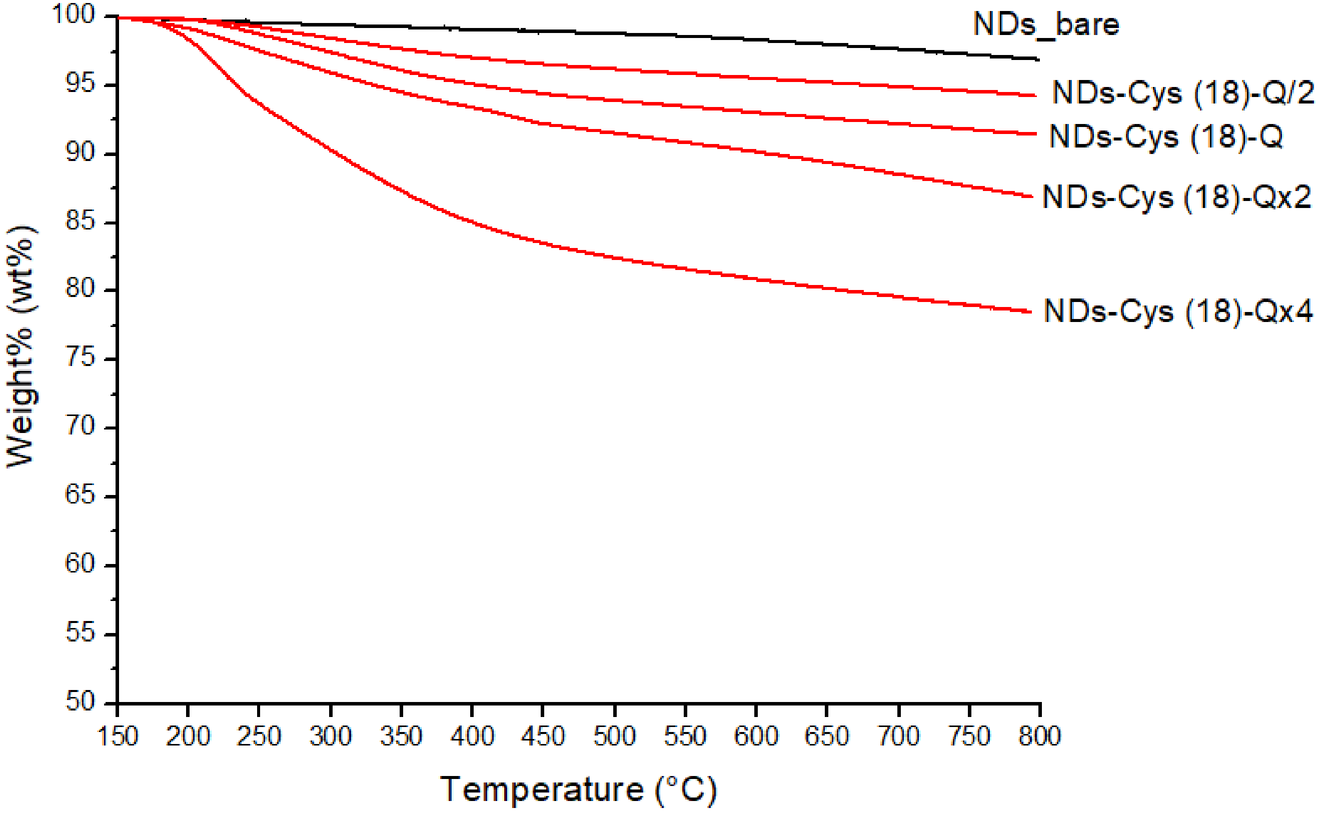

S35. Thermogravigrams of NDs-Cys (18) nanosystem, obtained in condition Q/2, Q, Qx2, Qx4.

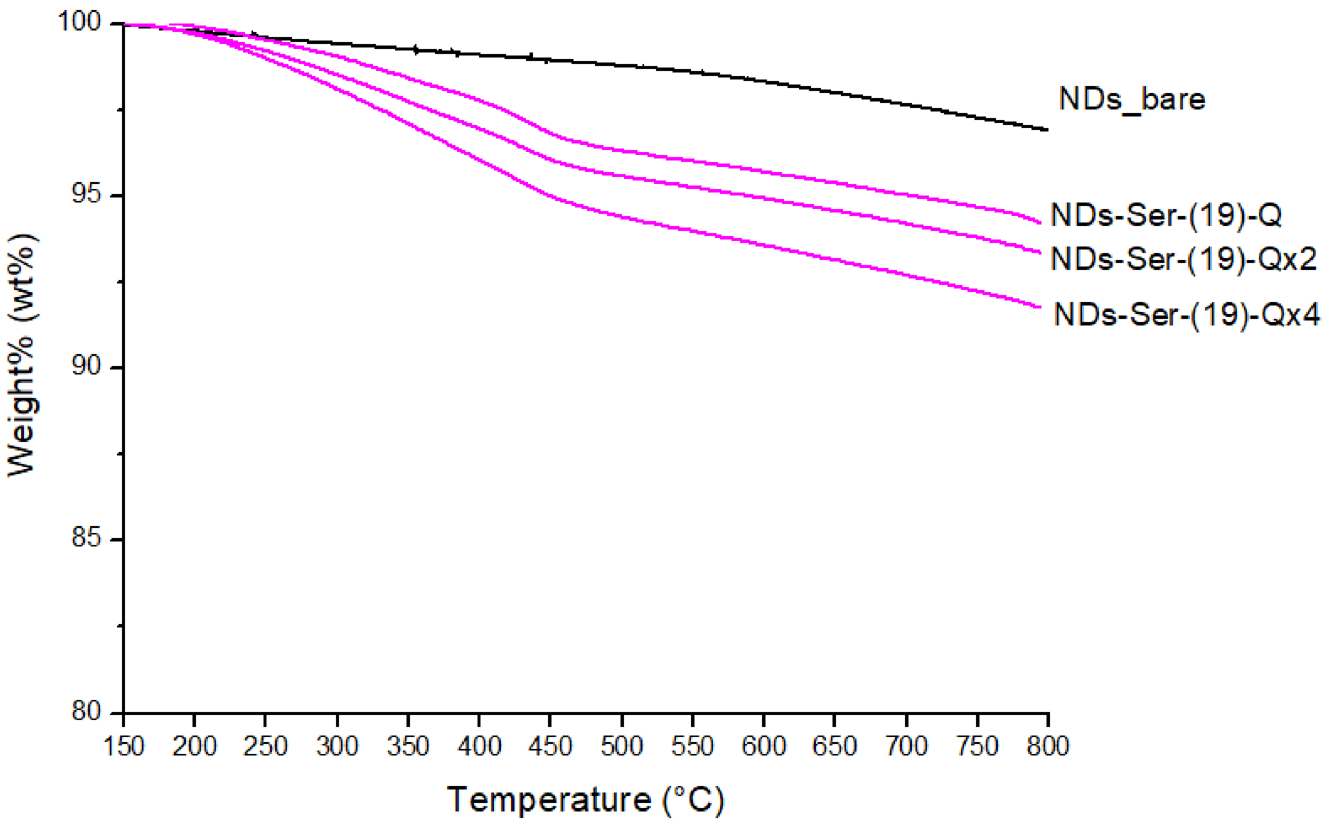

S36. Thermogravigrams of NDs-Ser (19) nanosystem, obtained in condition Q, Qx2, Qx4.

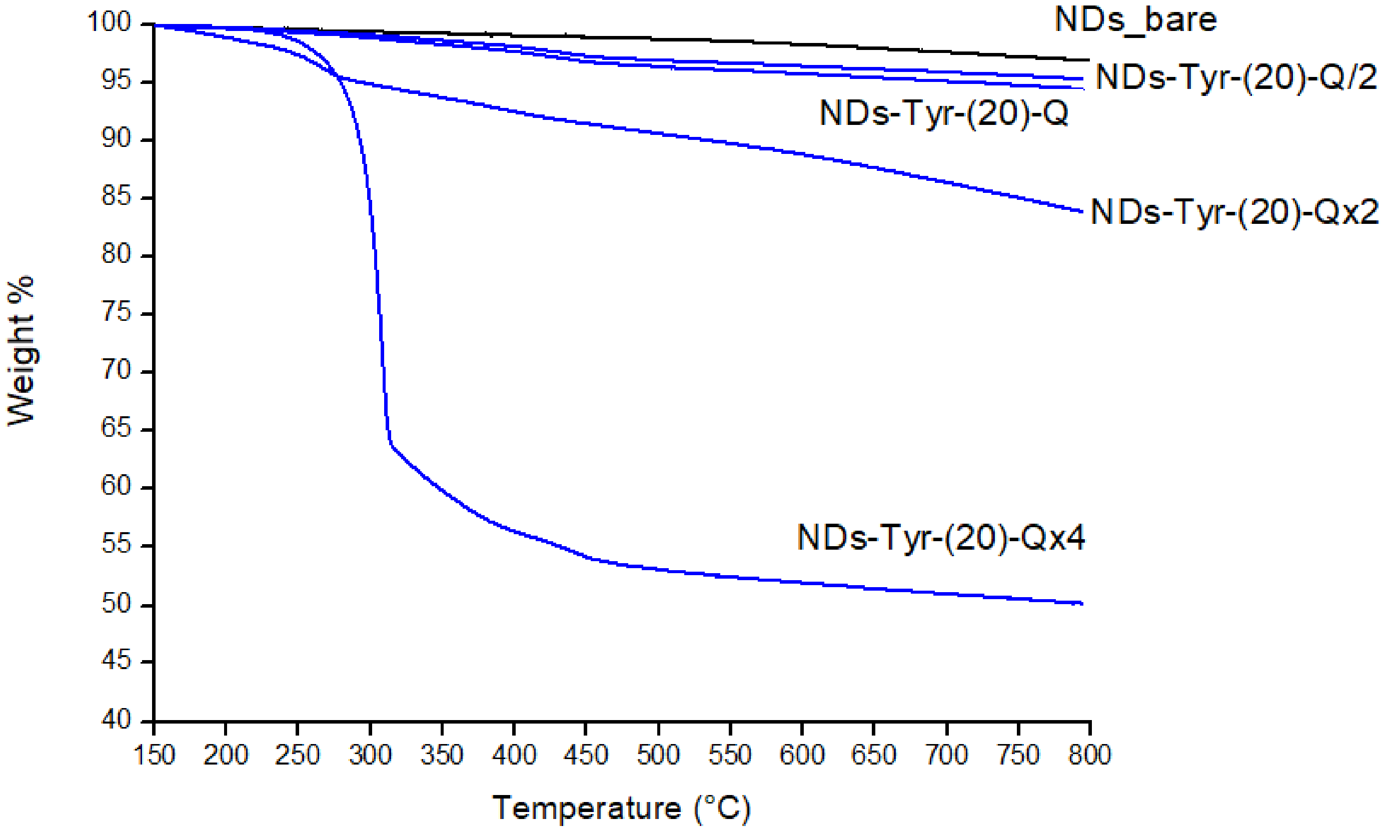

S37. Thermogravigrams of NDs-Tyr (20) nanosystem, obtained in condition Q/2, Q, Qx2, Qx4.

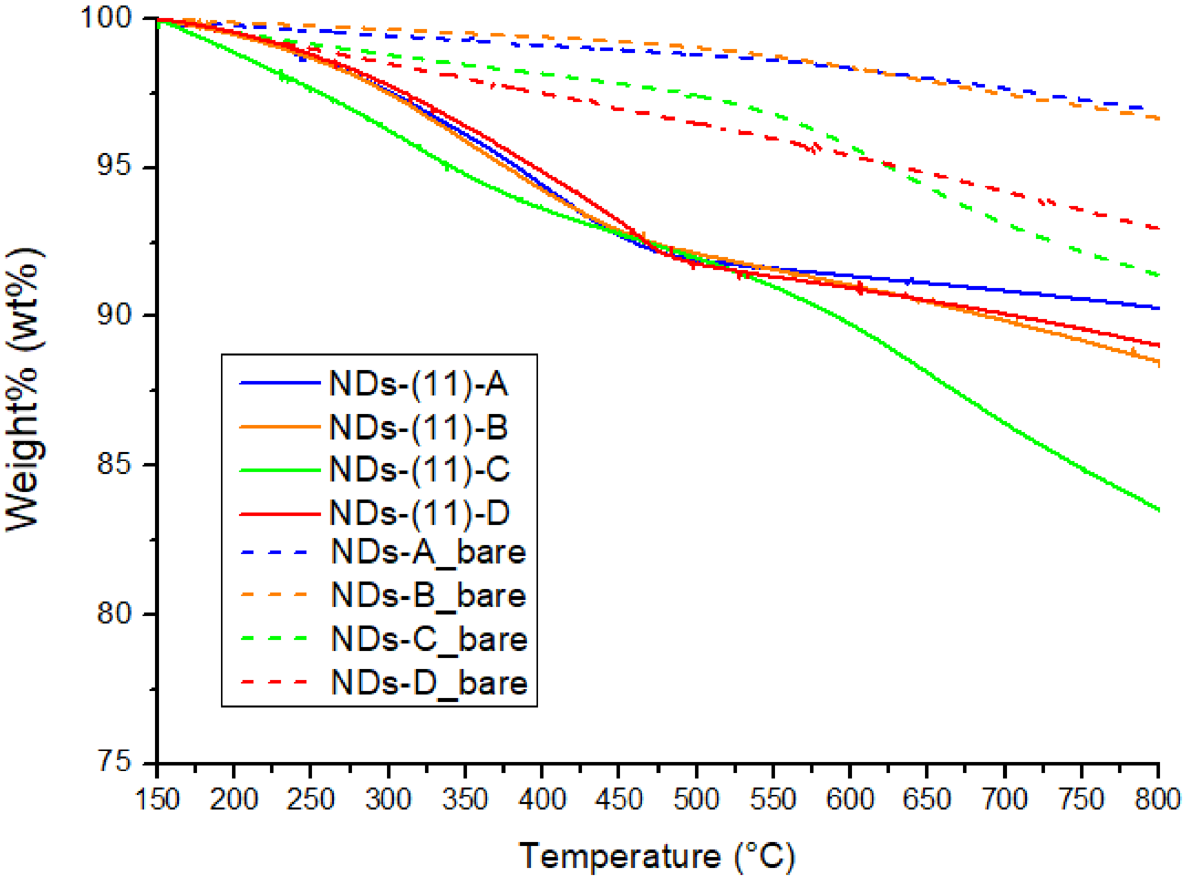

S38. Thermogravigrams of differently oxidized NDs-A (blue dash line), NDs-B (orange dash line), NDs-C (green dash line), NDs-D (red dash line), reacted with lysine and paraformaldehyde, leading to the corresponding NDs-(11)-(A, B, C, D) (solid lines).

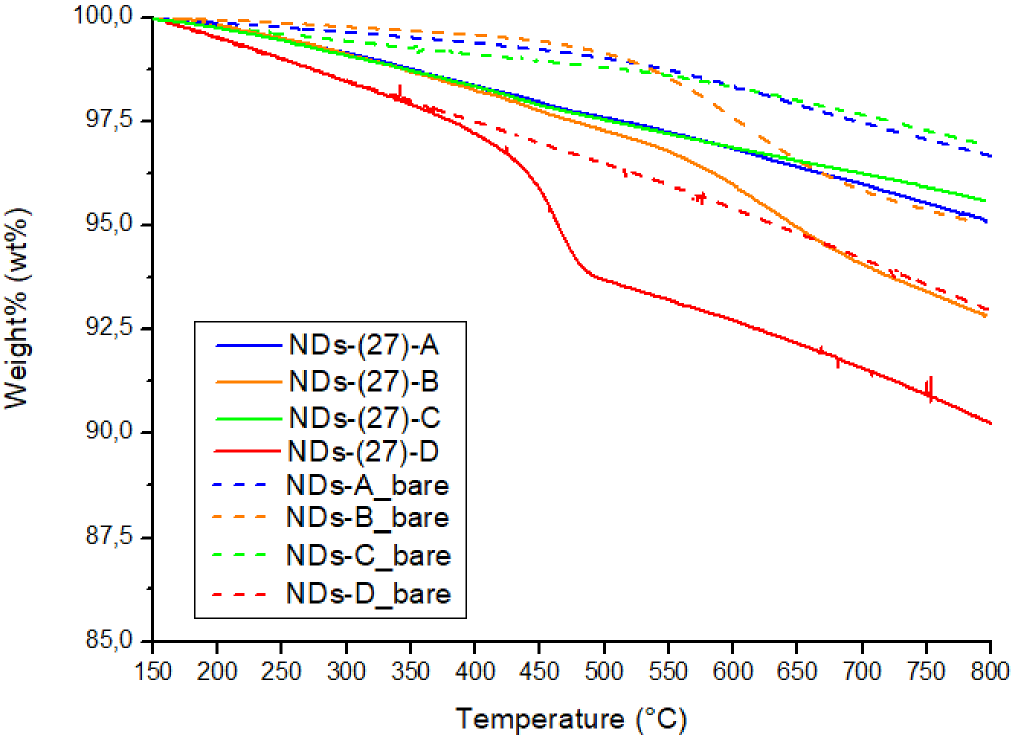

S39. Thermogravigrams of differently oxidized NDs-A (blue dash line), NDs-B (orange dash line), NDs-C (green dash line), NDs-D (red dash line), reacted with monoboc-protected diamine (b), leading to the corresponding NDs-(27)-(A, B, C, D) (solid lines).

BIBLIOGRAPHY

1. Hong, G., Diao, S., Antaris, A. L. & Dai, H. Carbon Nanomaterials for Biological Imaging and Nanomedicinal Therapy. *Chem. Rev.* 115, 10816–10906 (2015).

2. Xu, N., Chen, J. & Deng, S. Effect of heat treatment on the properties of nano-diamond under oxygen and argon ambient. *Diam. Relat. Mater. - DIAM RELAT MATER* 11, 249–256 (2002).

3. Gali, Á. Ab initio theory of the nitrogen-vacancy center in diamond. *Nanophotonics* 8, 1907–1943.

4. Mita, Y. Change of absorption spectra in type-Ib diamond with heavy neutron irradiation. *Phys. Rev. B* 53, 11360–11364 (1996).

5. Kuznetsov, V. L., Chuvilin, A. L., Butenko, Y. V, Mal'kov, I. Y. & Titov, V. M. Onion-like carbon from ultra-disperse diamond. *Chem. Phys. Lett.* 222, 343–348 (1994).

6. Petrakova, V. *et al.* Charge-sensitive fluorescent nanosensors created from nanodiamonds. *Nanoscale* 7, 12307–12311 (2015).

7. Miloushev, V. Z. *et al.* Metabolic Imaging of the Human Brain with Hyperpolarized <sup>13</sup>C Pyruvate Demonstrates <sup>13</sup>C Lactate Production in Brain Tumor Patients. *Cancer Res.* 78, 3755 LP – 3760 (2018).

8. Reina, G., Zhao, L., Bianco, A. & Komatsu, N. Chemical Functionalization of Nanodiamonds: Opportunities and Challenges Ahead. *Angew. Chem. Int. Ed. Engl.* 58, 17918–17929 (2019).

9. Kong, X. L. *et al.* High-Affinity Capture of Proteins by Diamond Nanoparticles for Mass Spectrometric Analysis. *Anal. Chem.* 77, 259–265 (2005).

10. Hsiao, W. W.-W., Hui, Y. Y., Tsai, P.-C. & Chang, H.-C. Fluorescent Nanodiamond: A Versatile Tool for Long-Term Cell Tracking, Super-Resolution Imaging, and Nanoscale Temperature Sensing. *Acc. Chem. Res.* 49, 400–407 (2016).

11. Ma, L., Hart, A. H. C., Ozden, S., Vajtai, R. & Ajayan, P. M. Spiers Memorial Lecture Advances of carbon nanomaterials. *Faraday Discuss.* 173, 9–46 (2014).

12. Mochalin, V. N., Shenderova, O., Ho, D. & Gogotsi, Y. The properties and applications of nanodiamonds. *Nat. Nanotechnol.* 7, 11–23 (2012).

13. Stehlik, S. *et al.* Size and Purity Control of HPHT Nanodiamonds down to 1 nm. *J. Phys. Chem. C* 119, 27708–27720 (2015).

14. Adiga, L. . *Nanodiamonds Applications in Biology and nanoscale Medicine*. (Springer, 2010).

15. Yang, L., May, P. W., Yin, L., Smith, J. A. & Rosser, K. N. Growth of diamond nanocrystals by pulsed laser ablation of graphite in liquid. *Diam. Relat. Mater.* 16, 725–729 (2007).

16. Hu, S., Sun, J., Du, X., Tian, F. & Jiang, L. The formation of multiply twinning structure and photoluminescence of well-dispersed nanodiamonds produced by pulsed-laser irradiation. *Diam. Relat. Mater.* 17, 142–146 (2008).

17. Basso, L. *et al.* The modeling and synthesis of nanodiamonds by laser ablation of graphite and diamond-like carbon in liquid-confined ambient. *Appl. Phys. A* 124, 72 (2017).

18. Qiao, Z., Li, J., Zhao, N., Shi, C. & Nash, P. Graphitization and microstructure transformation of nanodiamond to onion-like carbon. *Scr. Mater.* 54, 225–229 (2006).

19. Kuznetsov, V. L., Zilberberg, I. L., Butenko, Y. V, Chuvilin, A. L. & Segall, B. Theoretical study of the formation of closed curved graphite-like structures during annealing of diamond surface. *J. Appl. Phys.* 86, 863–870 (1999).

20. Barnard, A. S., Russo, S. P. & Snook, I. K. Structural relaxation and relative stability of nanodiamond morphologies. *Diam. Relat. Mater.* 12, 1867–1872 (2003).

21. Osswald, S., Yushin, G., Mochalin, V., Kucheyev, S. O. & Gogotsi, Y. Control of sp2/sp3 carbon ratio and surface chemistry of nanodiamond powders by selective oxidation in air. *J. Am. Chem. Soc.* 128, 11635–11642 (2006).

22. Gaebel, T. *et al.* Size-reduction of nanodiamonds via air oxidation. *Diam. Relat. Mater.* 21, 28–32 (2011).

23. Smith, B., Gruber, D. & Plakhotnik, T. The effects of surface oxidation on

luminescence of nano diamonds. *Diam. Relat. Mater.* 19, 314–318 (2010).

24. Dolmatov, V. Y. Detonation-synthesis nanodiamonds: synthesis, structure, properties and applications. *Russ. Chem. Rev.* 76, 339–360 (2007).

25. O. Shenderova, A. V. *Detonation Nanodiamonds. Science and Applications*. (Pan Stanfor Publishing, 2013).

26. Ōsawa, E. Recent progress and perspectives in single-digit nanodiamond. *Diam. Relat. Mater.* 16, 2018–2022 (2007).

27. Nguyen, T.-T.-B., Chang, H.-C. & Wu, V. W.-K. Adsorption and hydrolytic activity of lysozyme on diamond nanocrystallites. *Diam. Relat. Mater.* 16, 872–876 (2007).

28. Boudou, J.-P. *et al.* High yield fabrication of fluorescent nanodiamonds. *Nanotechnology* 20, 235602 (2009).

29. Bogatyreva, G. P. *et al.* The effect of the methods of recovering diamond nanopowders on their physicochemical properties. *J. Superhard Mater.* 33, 208–216 (2011).

30. Brunauer, S., Emmett, P. H. & Teller, E. Adsorption of Gases in Multimolecular Layers. *J. Am. Chem. Soc.* 60, 309–319 (1938).

31. Mcdonough, J. & Gogotsi, Y. Carbon Onions: Synthesis and Electrochemical Applications. *Electrochem. Soc. Interface* 22, 61–66 (2013).

32. Ozawa, T. Thermal analysis — review and prospect. *Thermochim. Acta* 355, 35–42 (2000).

33. Lang, D. & Krueger, A. The Prato reaction on nanodiamond: Surface functionalization by formation of pyrrolidine rings. *Diam. Relat. Mater.* 20, 101–104 (2011).

34. Jarre, G., Liang, Y., Betz, P., Lang, D. & Krueger, A. Playing the surface game—diels–alder reactions on diamond nanoparticles. *Chem. Commun.* 47, 544–546 (2011).

35. Lang, D. & Krueger, A. Functionalizing nanodiamond particles with N-heterocyclic iminium bromides and dicyano methanides. *Diam. Relat. Mater.* 79, 102–107 (2017).

36. Ozawa, M. *et al.* Preparation and behavior of brownish, clear nanodiamond colloids. *Adv. Mater.* 19, 1201–1206 (2007).

37. Dolmatov, V. Y. *et al.* IR spectra of detonation nanodiamonds modified during the synthesis. *J. Superhard Mater.* 36, 344–357 (2014).

38. Ji, S., Jiang, T., Xu, K. & Li, S. FTIR study of the adsorption of water on ultradispersed diamond powder surface. *Appl. Surf. Sci.* 133, 231–238 (1998).

39. Picollo, F. *et al.* Synthesis and characterization of porphyrin functionalized nanodiamonds. *Diam. Relat. Mater.* 91, 22–28 (2019).

40. Dresselhaus, M. S., Jorio, A. & Saito, R. Characterizing Graphene, Graphite, and Carbon Nanotubes by Raman Spectroscopy. *Annu. Rev. Condens. Matter Phys.* 1, 89–108 (2010).

41. M.S. Dresselhaus., P. C. E. *Science of fullerenes and carbon nanotubes*. (Academic Press, 1996).

42. Ferrari, A. C. & Robertson, J. Raman spectroscopy of amorphous, nanostructured, diamond-like carbon, and nanodiamond. *Philos. Trans. R. Soc. A Math. Phys. Eng. Sci.* 362, 2477–2512 (2004).

43. Itoh, T. & McCreery, R. L. In situ Raman spectroelectrochemistry of azobenzene monolayers on glassy carbon. *Anal. Bioanal. Chem.* 388, 131–134 (2007).

44. Shenderova, O. *et al.* Surface Chemistry and Properties of Ozone-Purified Detonation Nanodiamonds. *J. Phys. Chem. C* 115, 9827–9837 (2011).

45. Aramesh, M., Shimoni, O., Ostrikov, K., Prawer, S. & Cervenka, J. Surface charge effects in protein adsorption on nanodiamonds. *Nanoscale* 7, 5726–5736 (2015).

46. Chow, E. K. *et al.* Nanodiamond therapeutic delivery agents mediate enhanced chemoresistant tumor treatment. *Sci. Transl. Med.* 3, 73ra21 (2011).

47. Nangia, S. & Sureshkumar, R. Effects of Nanoparticle Charge and Shape Anisotropy on Translocation through Cell Membranes. *Langmuir* 28, 17666–17671 (2012).

48. Delgado, A. V, González-Caballero, F., Colomba F., Hunter, R. J., Koopal, L. K. & Lyklema, J. Measurement and interpretation of electrokinetic phenomena. *J. Colloid Interface Sci.* 309, 194–224 (2007).

49. Ginés, L. *et al.* Positive zeta potential of nanodiamonds. *Nanoscale* 9, 12549–12555 (2017).

50. Stehlik, S. *et al.* Nanoparticles Assume Electrical Potential According to Substrate, Size, and Surface Termination. *Langmuir* 29, 1634–1641 (2013).

51. Hees, J., Kriele, A. & Williams, O. Electrostatic self-assembly of diamond nanoparticles. *Chem. Phys. Lett.* 509, 12–15 (2011).

52. Doherty, M. W., Manson, N. B., Delaney, P. & Hollenberg, L. C. L. The negatively charged nitrogen-vacancy centre in diamond: The electronic solution. *New J. Phys.* 13, (2011).

53. Coulson, C. ~A. & Kearsley, M. J. Colour Centres in Irradiated Diamonds. I. *Proc. R. Soc. London Ser. A* 241, 433–454 (1957).

54. Ma, Y., Rohlfing, M. & Gali, A. Excited states of the negatively charged nitrogen-vacancy color center in diamond. *Phys. Rev. B* 81, 41204 (2010).

55. Beveratos, A., Brouri, R., Gacoin, T., Poizat, J.-P. & Grangier, P. Nonclassical radiation from diamond nanocrystals. *Phys. Rev. A* 64, 61802 (2001).

56. Mohtashami, A. & Femius Koenderink, A. Suitability of nanodiamond nitrogen–vacancy centers for spontaneous emission control experiments. *New J. Phys.* 15, 43017 (2013).

57. Zheng, D. *et al.* A hand-held magnetometer based on an ensemble of nitrogen-vacancy centers in diamond. *J. Phys. D Appl. Phys.* 53, 155004 (2020).

58. Holzgrafe, J. *et al.* Nanoscale NMR Spectroscopy Using Nanodiamond Quantum Sensors. *Phys. Rev. Appl.* 13, 44004 (2020).

59. Singam, S. K. R., Nesladek, M. & Goovaerts, E. Nitrogen-vacancy nanodiamond based local thermometry using frequency-jump modulation. *Nanotechnology* 31, 105501 (2020).

60. Abeywardana, C., Stepanov, V., Cho, F. & Takahashi, S. Magnetic resonance spectroscopy using a single nitrogen-vacancy center in diamond. *Proc SPIE* 9269, 92690K (2014).

61. Slichter, C. P. *Principles of Magnetic Resonance*. (Springer, 1996).

62. Sotoma, S. *et al.* Enrichment of ODMR-active nitrogen-vacancy centres in five-nanometre-sized detonation-synthesized nanodiamonds: Nanoprobes for temperature, angle and position. *Sci. Rep.* 8, 5463 (2018).

63. Clevenson, H. *et al.* Broadband magnetometry and temperature sensing with a light-trapping diamond waveguide. *Nat. Phys.* 11, 393–397 (2015).

64. Neumann, P. *et al.* High-Precision Nanoscale Temperature Sensing Using Single Defects in Diamond. *Nano Lett.* 13, 2738–2742 (2013).

65. Dolde, F. *et al.* Electric-field sensing using single diamond spins. *Nat. Phys.* 7, 459–463 (2011).

66. Bourgeois, E. *et al.* Photoelectric detection of electron spin resonance of nitrogen-vacancy centres in diamond. *Nat. Commun.* 6, 8577 (2015).

67. Hegyi, A. & Yablonovitch, E. Molecular Imaging by Optically Detected Electron Spin Resonance of Nitrogen-Vacancies in Nanodiamonds. *Nano Lett.* 13, 1173–1178 (2013).

68. Mrózek, M. *et al.* Longitudinal spin relaxation in nitrogen-vacancy ensembles in diamond. *EPJ Quantum Technol.* 2, 22 (2015).

69. Redman, D. A., Brown, S., Sands, R. H. & Rand, S. C. Spin dynamics and electronic states of N-V centers in diamond by EPR and four-wave-mixing spectroscopy. *Phys. Rev. Lett.* 67, 3420–3423 (1991).

70. Jarmola, A., Acosta, V. M., Jensen, K., Rinaldi S., Chemerisov, S. & Budker, D. Temperature- and Magnetic-Field-Dependent Longitudinal Spin Relaxation in Nitrogen-Vacancy Ensembles in Diamond. *Phys. Rev. Lett.* 108, 197601 (2012).

71. Kaufmanna, S. *et al.* Detection of atomic spin labels in a lipid bilayer using a single-spin nanodiamond probe. *Proc. Natl. Acad. Sci. U. S. A.* 110, 10894–10898 (2013).

72. McGuinness, L. P. *et al.* Ambient nanoscale sensing with single spins using quantum decoherence. *New J. Phys.* 15, 73042 (2013).

73. Giri, R., Dorigoni, C., Tambalo, S., Gorrini, F. & Bifone, A. Selective measurement of charge dynamics in an ensemble of nitrogen-vacancy centers in nanodiamond and bulk diamond. *Phys. Rev. B* 99, 1–8 (2019).

74. Giri, R. *et al.* Coupled charge and spin dynamics in high-density ensembles of nitrogen-vacancy centers in diamond. *Phys. Rev. B* 98, 1–7 (2018).

75. Felton, S. *et al.* Electron paramagnetic resonance studies of the neutral nitrogen vacancy in diamond. *Phys. Rev. B* 77, 81201 (2008).

76. Gali, A. Theory of the neutral nitrogen-vacancy center in diamond and its application to the realization of a qubit. *Phys. Rev. B* 79, 235210 (2009).

77. Manson, N. B. & Harrison, J. P. Photo-ionization of the nitrogen-vacancy

center in diamond. *Diam. Relat. Mater.* 14, 1705–1710 (2005).

78. Giri, R. *et al.* Coupled charge and spin dynamics in high-density ensembles of nitrogen-vacancy centers in diamond. *Phys. Rev. B* 98, 45401 (2018).

79. Dhomkar, S., Jayakumar, H., Zangara, P. R. & Meriles, C. A. Charge Dynamics in near-Surface, Variable-Density Ensembles of Nitrogen-Vacancy Centers in Diamond. *Nano Lett.* 18, 4046–4052 (2018).

80. Petrakova, V. *et al.* Charge-sensitive fluorescent nanosensors created from nanodiamonds. *Nanoscale* 7, 12307–12311 (2015).

81. Zhang, T. *et al.* Hybrid nanodiamond quantum sensors enabled by volume phase transitions of hydrogels. *Nat. Commun.* 9, 3188 (2018).

82. Steinert, S. *et al.* Magnetic spin imaging under ambient conditions with sub-cellular resolution. *Nat. Commun.* 4, 1607 (2013).

83. Tetienne, J.-P. *et al.* Spin relaxometry of single nitrogen-vacancy defects in diamond nanocrystals for magnetic noise sensing. *Phys. Rev. B* 87, 235436 (2013).

84. Panich, A. M. *et al.* Magnetic Resonance Study of Gadolinium-Grafted Nanodiamonds. *J. Phys. Chem. C* 120, 19804–19811 (2016).

85. Rendler, T. *et al.* Optical imaging of localized chemical events using programmable diamond quantum nanosensors. *Nat. Commun.* 8, (2017).

86. Lin, B.-R. *et al.* Fe Doped Magnetic Nanodiamonds Made by Ion Implantation as Contrast Agent for MRI. *Scientific reports* vol. 8 7058 (2018).

87. Chang, Y. R. *et al.* Mass production and dynamic imaging of fluorescent nanodiamonds. *Nat. Nanotechnol.* 3, 284–288 (2008).

88. Reddy, N. R. S., Manson, N. B. & Krausz, E. R. Two-laser spectral hole burning in a colour centre in diamond. *J. Lumin.* 38, 46–47 (1987).

89. Batalov, A. *et al.* Low Temperature Studies of the Excited-State Structure of Negatively Charged Nitrogen-Vacancy Color Centers in Diamond. *Phys. Rev. Lett.* 102, 195506 (2009).

90. Smith, B. R. *et al.* Five-nanometer diamond with luminescent nitrogen-vacancy defect centers. *Small* 5, 1649–1653 (2009).

91. Zhao, L. *et al.* Chromatographic Separation of Highly Soluble Diamond

Nanoparticles Prepared by Polyglycerol Grafting. *Angew. Chemie Int. Ed.* 50, 1388–1392 (2011).

92. Zhang, X. *et al.* PEGylation and polyPEGylation of nanodiamond. *Polymer (Guildf).* 53, 3178–3184 (2012).

93. Tinwala, H. & Wairkar, S. Production, surface modification and biomedical applications of nanodiamonds: A sparkling tool for theranostics. *Mater. Sci. Eng. C* 97, 913–931 (2019).

94. Schrand, A. M. *et al.* Are diamond nanoparticles cytotoxic? *J. Phys. Chem. B* 111, 2–7 (2007).

95. Schrand, A. M., Dai, L., Schlager, J. J., Hussain, S. M. & Osawa, E. Differential biocompatibility of carbon nanotubes and nanodiamonds. *Diam. Relat. Mater.* 16, 2118–2123 (2007).

96. Moosa, B. *et al.* Applications of nanodiamonds in drug delivery and catalysis. *J. Nanosci. Nanotechnol.* 14, 332–343 (2014).

97. Chen, X. *et al.* Fabrication of an EGF modified nanodiamonds-based anti-cancer drug targeted delivery system and drug carrier uptake visualization by 3D Raman microscopy. *RSC Adv.* 6, (2016).

98. Guan, B., Zou, F. & Zhi, J. Nanodiamond as the pH-Responsive Vehicle for an Anticancer Drug. *Small* 6, 1514–1519 (2010).

99. Lin, Y. W. *et al.* Co-delivery of paclitaxel and cetuximab by nanodiamond enhances mitotic catastrophe and tumor inhibition. *Sci. Rep.* 7, 1–11 (2017).

100. Wee, T.-L. *et al.* Two-photon Excited Fluorescence of Nitrogen-Vacancy Centers in Proton-Irradiated Type Ib Diamond. *J. Phys. Chem. A* 111, 9379–9386 (2007).

101. Billinton, N. & Knight, A. W. Seeing the wood through the trees: a review of techniques for distinguishing green fluorescent protein from endogenous autofluorescence. *Anal. Biochem.* 291, 175–197 (2001).

102. Yu, S.-J., Kang, M.-W., Chang, H.-C., Chen, K.-M. & Yu, Y.-C. Bright Fluorescent Nanodiamonds: No Photobleaching and Low Cytotoxicity. *J. Am. Chem. Soc.* 127, 17604–17605 (2005).

103. Chang, B.-M. *et al.* Highly Fluorescent Nanodiamonds Protein-Functionalized for Cell Labeling and Targeting. *Adv. Funct. Mater.* 23, 5737–5745 (2013).

104. Lin, H.-H. *et al.* Tracking and Finding Slow-Proliferating/Quiescent Cancer Stem Cells with Fluorescent Nanodiamonds. *Small* 11, 4394–4402 (2015).

105. Fang, C.-Y. *et al.* The exocytosis of fluorescent nanodiamond and its use as a long-term cell tracker. *Small* 7, 3363–3370 (2011).

106. Wu, T.-J. *et al.* Tracking the engraftment and regenerative capabilities of transplanted lung stem cells using fluorescent nanodiamonds. *Nat. Nanotechnol.* 8, 682–689 (2013).

107. Fujisaku, T. *et al.* PH Nanosensor Using Electronic Spins in Diamond. *ACS Nano* 13, 11726–11732 (2019).

108. Butler, J. E., Mankelevich, Y. A., Cheesman, A., Ma, J. & Ashfold, M. N. R. Understanding the chemical vapor deposition of diamond: recent progress. *J. Phys. Condens. Matter* 21, 364201 (2009).

109. Paci, J. T., Man, H. B., Saha, B., Ho, D. & Schatz, G. C. Understanding the Surfaces of Nanodiamonds. *J. Phys. Chem. C* 117, 17256–17267 (2013).

110. Bondar', V. S., Pozdnyakova, I. O. & Puzyr', A. P. Applications of nanodiamonds for separation and purification of proteins. *Phys. Solid State* 46, 758–760 (2004).

111. Krueger, A. & Lang, D. Functionality is Key: Recent Progress in the Surface Modification of Nanodiamond. *Adv. Funct. Mater.* 22, 890–906 (2012).

112. Wang, Y. *et al.* Electrochemical Behavior of Fluorinated and Aminated Nanodiamond. *Int. J. Electrochem. Sci.* 7, (2012).

113. Nakamura, T., Ohana, T., Hagiwara, Y. & Tsubota, T. Photochemical modification of diamond powders with elemental sulfur and their surface-attachment behavior on gold surfaces. *Phys. Chem. Chem. Phys.* 11, 730–734 (2009).

114. Stanishevsky, A. V, Walock, M. J. & Catledge, S. A. Surface modification and stability of detonation nanodiamonds in microwave gas discharge plasma. *Appl. Surf. Sci.* 357, 1403–1409 (2015).

115. Krüger, A., Liang, Y., Jarre, G. & Stegk, J. Surface functionalisation of detonation diamond suitable for biological applications. *J. Mater. Chem.* 16, 2322–2328 (2006).

116. Meinhardt, T., Lang, D., Dill, H. & Krueger, A. Pushing the functionality of diamond nanoparticles to new horizons: Orthogonally functionalized nanodiamond using click chemistry. *Adv. Funct. Mater.* 21, 494–500 (2011).

117. Spitsyn, B. V *et al.* Inroad to modification of detonation nanodiamond. *Diam. Relat. Mater.* 15, 296–299 (2006).

118. Lisichkin, G. V, Kulakova, I. I., Gerasimov, Y. A., Karpukhin, A. V & Yakovlev, R. Y. Halogenation of detonation-synthesised nanodiamond surfaces. *Mendeleev Commun.* 19, 309–310 (2009).

119. Mermoux, M., Crisci, A., Petit, T., Girard, H. A. & Arnault, J. C. Surface modifications of detonation nanodiamonds probed by multiwavelength raman spectroscopy. *J. Phys. Chem. C* 118, 23415–23425 (2014).

120. Krueger, A. & Boedeker, T. Deagglomeration and functionalisation of detonation nanodiamond with long alkyl chains. *Diam. Relat. Mater.* 17, 1367–1370 (2008).

121. Mochalin, V. N. *et al.* Covalent Incorporation of Aminated Nanodiamond into an Epoxy Polymer Network. *ACS Nano* 5, 7494–7502 (2011).

122. Ripoll, J. L., Rouessac, A. & Rouessac, F. Applications recentes de la reaction de retro-diels-alder en synthese organique. *Tetrahedron* 34, 19–40 (1978).

123. Karpf, M. Organic Synthesis at High Temperatures. Gas-Phase Flow Thermolysis [New Synthetic Methods (57)]. *Angew. Chemie Int. Ed. English* 25, 414–430 (1986).

124. Betz, P. & Krueger, A. Surface Modification of Nanodiamond under Bingel–Hirsch Conditions. *ChemPhysChem* 13, 2578–2584 (2012).

125. Romanova, E. E., Akiel, R., Cho, F. H. & Takahashi, S. Grafting nitroxide radicals on nanodiamond surface using click chemistry. *J. Phys. Chem. A* 117, 11933–11939 (2013).

126. Maggini, M., Scorrano, G. & Prato, M. Addition of azomethine ylides to C60: synthesis, characterization, and functionalization of fullerene pyrrolidines. *J. Am. Chem. Soc.* 115, 9798–9799 (1993).

127. Steinert, S. *et al.* Magnetic spin imaging under ambient conditions with sub-cellular resolution. *Nat. Commun.* 4, (2013).

128. Kaufmann, S. *et al.* Detection of atomic spin labels in a lipid bilayer using a single-spin nanodiamond probe. *Proc. Natl. Acad. Sci.* 110, 10894 LP – 10898 (2013).

129. Liu, G.-Q., Feng, X., Wang, N., Li, Q. & Liu, R.-B. Coherent quantum control of nitrogen-vacancy center spins near 1000 kelvin. *Nat. Commun.* 10, 1344 (2019).

130. Dolmans, D. E. J. G. J., Fukumura, D. & Jain, R. K. Photodynamic therapy for cancer. *Nat. Rev. Cancer* 3, 380–387 (2003).

131. Sibata, C. H., Colussi, V. C., Oleinick, N. L. & Kinsella, T. J. Photodynamic therapy in oncology. *Expert Opin. Pharmacother.* 2, 917–927 (2001).

132. Boucher, L. J. & Katz, J. J. The Infared Spectra of Metalloporphyrins (4000-160 Cm-1). *J. Am. Chem. Soc.* 89, 1340–1345 (1967).

133. Tagmatarchis, N. & Prato, M. Functionalization of carbon nanotubes via 1,3-dipolar cycloadditions. *J. Mater. Chem.* 14, 437–439 (2004).

134. Brown, A. E. A Polymer Reaction Product of Tyrosine and Formaldehyde. *J. Am. Chem. Soc.* 68, 1011–1015 (1946).

135. Martín, N. *et al.* Retro-cycloaddition reaction of pyrrolidinofullerenes. *Angew. Chemie - Int. Ed.* 45, 110–114 (2005).

136. Li, D. *et al.* Cetuximab-conjugated nanodiamonds drug delivery system for enhanced targeting therapy and 3D Raman imaging. *J. Biophotonics* 10, 1636–1646 (2017).

137. Rondin, L. *et al.* Magnetometry with nitrogen-vacancy defects in diamond. *Reports Prog. Phys.* 77, 56503 (2014).

138. Gorrini, F. *et al.* On the thermodynamic path enabling a room-temperature, laser-assisted graphite to nanodiamond transformation. *Sci. Rep.* 6, 35244 (2016).

139. Basso, L. *et al.* Laser-Synthesis of NV-Centers-Enriched Nanodiamonds: Effect of Different Nitrogen Sources. *Micromachines* 11, (2020).

140. Bradac, C. *et al.* Observation and control of blinking nitrogen-vacancy centres in discrete nanodiamonds. *Nat. Nanotechnol.* 5, 345–349 (2010).

141. Stacey, A. *et al.* Evidence for Primal sp2 Defects at the Diamond Surface: Candidates for Electron Trapping and Noise Sources. *Adv. Mater. Interfaces* 6, 1801449 (2019).